Optimal directed searches
for continuous gravitational waves

Der Fakultät für Mathematik und Physik
Gottfried Wilhelm Leibniz Universität Hannover

zur Erlangung des akademischen Grades
Doktor der Naturwissenschaften
Dr. rer. nat.

genehmigte Dissertation von

Jing Ming M.Sci.

geboren am 02.07.1986 in Zhejiang, China

2017

ii

Supervisor:

Dr. rer. nat. (Adj. Prof. UWM) M. Alessandra Papa
Max-Planck-Institut für Gravitationsphysik
University of Wisconsin-Milwaukee (UWM)

Co-supervisor::

Prof. Dr. Bruce Allen
Max-Planck-Institut für Gravitationsphysik
University of Wisconsin-Milwaukee
Leibniz Universität Hannover

Dr. Badri Krishnan
Max-Planck-Institut für Gravitationsphysik
Leibniz Universität Hannover

Tag der Disputation:
16.08.2017

Abstract

On 14 September, 2015, gravitational waves (GWs) were detected for the first time ever by the Laser Interferometer Gravitational-Wave Observatory (LIGO) detectors. GWs are one of the most important predictions of Einstein's theory of General Relativity. This particular GW event, GW150914, was a catastrophic merger of two stellar-mass black holes from the depths of the Universe. Since then, a new window on the Universe has been open.

Following GW150914, GWs from several other binary black hole mergers were observed. Continuous gravitational waves (CWs) from rapidly rotating compact star have also been predicted, but to date these signals have not been observed. CWs are expected to be weaker gravitational waves compared with binary black hole mergers. In order to detect these continuous but weak GWs, a long observation time is needed and a huge amount of computing power is often required. The detection of a continuous gravitational wave signal might depend on how intelligently we invest the computing power that we have available.

In the first work of this thesis, I propose an optimisation method for directed searches that determines what sources and what waveforms to target as well as the search set-up, given a fixed computational cost. This method picks the target and search parameters so that the probability of making a detection is maximized. Important inputs to this method are the priors that are assumed for the waveforms from a given target. These priors are folded in to the optimisation scheme and are convolved with a number of other factors, such as the frequency-dependent sensitivity of the detectors, the spindown-dependent cost of the search, and the maximum expected amplitude. One of our findings is that Vela Jr is a more promising target than Cas A. However, up until now, far more computing power has been spend on the searches for CWs from Cas A than the search for CWs from Vela Jr.

In the second work of this thesis, this optimisation method is applied in order to set up a directed search. This search was performed by the volunteer distributed computing project Einstein@Home (E@H) between December, 2016 and April, 2017. Four months of data from the first Advanced LIGO observation run (O1) were used and 3 point sources were targeted: Vela Jr, Cas A and G347.3. This search is the first deep and broad frequency range search for Cas A using the Advanced LIGO data and the first search for Vela Jr and G347.3 ever performed. The design of this search includes nontrivial new features with respect to the conceptual optimisation scheme proposed in the first work. I am looking forward to analysing the results from this search.

In the third work of this thesis, this optimisation method is used to set up a search for CW signals from isolated, unknown neutron stars at the Galactic Centre (GC) using O1 data. The GC is thought to harbour many compact objects and the $2 \times 2 \, \mathrm{pc}^2$ centred at Sgr A* is particularly dense in neutron stars and interesting to us. The novelty in this design is having to introduce two further search dimensions, the sky coordinates. This search is currently being performed on Einstein@Home and is expected to end in November, 2017.

Keywords: Gravitational Waves, Neutron Stars, Data Analysis, Galactic Centre

Kurzfassung

Am 14. September 2015 hat LIGO, das *Laser Interferometer Gravitational-Wave Observatory*, zum ersten Mal Gravitationswellen (GW) nachgewiesen. GW sind eine der bedeutendsten Vorhersagen von Einsteins Allgemeiner Relativitätstheorie. Dieses erste GW-Ereignis, GW150914, war die katastrophale Verschmelzung zweier Schwarzer Löcher stellarer Masse, aus den Tiefen des Universums. Seitdem steht ein neues Fenster auf das Universum offen.

Seit GW150914 wurden GW mehrerer anderer binärer Schwarzer Löcher beobachtet, während kontinuierliche GW (CW, für *Continuous gravitational Waves*) von schnell rotierenden kompakten Objekten noch nicht nachgewiesen werden konnten. Es wird erwartet, dass CW, im Vergleich zu den Verschmelzungen von Binärsystemen, schwchere Gravitationswellen sind. Um diese kontinuierlichen, aber schwachen GW nachzuweisen, bedarf es einer langen Beobachtungzeit und oft auch einer riesigen Rechenleistung. Die Detektion eines CW-Signals könnte davon abhängen, wie intelligent wir unsere verfügbare Rechenleistung investieren.

Im ersten Teil dieser Arbeit schlage ich eine Optimierungsmethode für gelenkte Suchen vor, die für eine gegebene Rechenleistung ermittelt, welche Quellen und welche Wellenformen anvisiert werden sollten und wie die Suche zu konfigurieren ist. Diese Methode wählt die Ziele und Suchparameter so aus, dass die Wahrscheinlichkeit einer Detektion maximiert wird. Wichtige Eingaben dieser Methode sind die Vorabannahmen für die Wellenformen eines gegebenen Ziels. Diese Annahmen werden in die Optimierungsmethode integriert und mit einigen weiteren Faktoren kombiniert: so etwa die frequenzabhängige Messgenauigkeit der Detektoren, die von der Frequenzänderung der Quelle abhängigen Rechenkosten der Suche sowie die maximal erwartete Amplitude. Beispielsweise ist eine unserer Erkenntnisse, dass Vela Jr. ein vielversprechenderes Ziel ist als Cas A. Dabei hat LIGO bisher noch keine einzige Suche für CWs mit Vela Jr. als spezifischem Ziel veröffentlicht.

Im zweiten Teil dieser Arbeit wird die Optimierungsmethode auf die Vorbereitung einer gelenkten Suche angewendet. Diese wurde dann zwischen Dezember 2016 und April 2017 mit dem Freiwilligen-Projekt für verteiltes Rechnen Einstein@Home (E@H) durchgeführt. Vier Monate an Daten aus der ersten Beobachtungskampagne (O1) von Advanced LIGO wurden genutzt, um 3 punktförmige Quellen anzuvisieren: Vela Jr., Cas A und G347.3. Dies ist die erste tiefe Suche über einen weiten Frequenzbereich mit Cas A als Ziel und Advanced-LIGO-Daten sowie die erste Suche überhaupt mit Vela Jr. und G347.3 als Zielen. Zur Gestaltung dieser Suche gehören nichttrivale Neuheiten im Vergleich zur allgemeinen Optimierungsmethode im ersten Teil. Ich erwarte gespannt die Auswertung der Ergebnisse aus dieser Suche.

Im dritten Teil wird die Optimierungsmethode für die Vorbereitung einer weiteren Suche nach CW-Signalen von einzelnen unbekannten Neutronensternen im Galaktischen Zentrum (GZ) angewendet, ebenfalls mit O1-Daten. Das GZ wird als Heimat vieler kompakter Objekte angesehen, und die $2 \times 2 \, \mathrm{pc}^2$ rund um Sgr A* sind besonders dicht mit Neutronensternen bevölkert und besonders interessant für uns. Das Neue an diesem Fall ist, dass wir zwei weitere Suchdimensionen einführen müssen, die Himmelskoordinaten. Die Suche läuft derzeit auf Einstein@Home und wir erwarten, dass sie im November 2017 endet.

Schlagworte: Gravitationswellen, Neutronensterne, Datenanlyse, Galaktisches Zentrum

Contents

Chapter 1

General Relativity and gravitational waves

Quantum mechanics (QM) and General Relativity (GR) are two foundations of human beings' deepest understanding of Nature. As one of the pillars of modern physics, quantum mechanics governs the properties of matter on a microscopic scale, from the size of Buckminsterfullerene (10^{-9} m) down to the electron (10^{-18} m) and the Planck length (10^{-35} m). The other pillar, General Relativity, governs the large-scale phenomena in the Universe, from the Earth orbiting around the Sun (10^{11} m) to the mergers of galaxies (10^{21} m) as well as the evolution of the Universe as a whole (10^{26} m). GR was developed by Albert Einstein in 1915. In this theory, gravity can be understood as a curvature of an unity of space and time – *spacetime*. In GR, spacetime has four dimensions: three spatial dimensions and one temporal dimension. The curvature of spacetime is caused by the matter and energy within. At the same time, matter and energy move through spacetime in a way defined by its curvature. GR not only predicts the existence of many exotic objects and phenomena in the Universe – such as black holes and neutron stars – but also forms our basic understanding of cosmology. GR has been greatly successful in the past century. However until very recently, one prediction had still not been confirmed – gravitational waves. Just as an accelerating charged particle generates electromagnetic waves, General Relativity predicts that an accelerating massive object would disrupt spacetime nearby and distorted spacetime would radiate from the source at the speed of light. This "ripple" of spacetime is a gravitational wave.

This chapter gives a brief introduction to gravitational waves. It starts with Einstein equations from which gravitational waves are derived. The effect of gravitational waves on test a mass is explained, and a few types of gravitational wave sources are introduced.
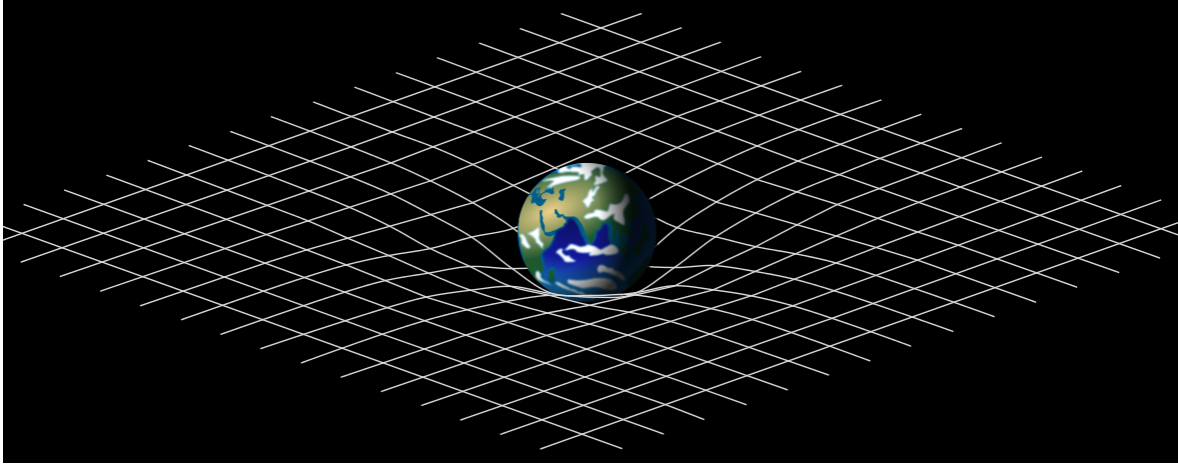
Figure 1.1: An illustration of how mass distorts spacetime (Credit: [1])

1.1 The Einstein equations in General Relativity

In special relativity, spacetime is flat and the distance between two points (the line element) can be expressed as

$$\mathrm{d}s^2 = -c^2\mathrm{d}t^2 + \mathrm{d}x^2 + \mathrm{d}y^2 + \mathrm{d}z^2 \qquad \text{or} \qquad \mathrm{d}s^2 = \eta_{\mu\nu}\mathrm{d}x^\mu\mathrm{d}x^\nu, \tag{1.1}$$

where the c is the speed of light and $\eta_{\mu\nu}$ is the Minkowski metric , which is expressed in Cartesian coordinates as

$$\eta_{\mu\nu} = \begin{pmatrix} -1 & 0 & 0 & 0 \\ 0 & 1 & 0 & 0 \\ 0 & 0 & 1 & 0 \\ 0 & 0 & 0 & 1 \end{pmatrix}. \tag{1.2}$$

This Minkowski metric describes flat spacetime. In General Relativity, as gravity is now included, spacetime is instead curved. The more general expression of the line element is then:

$$\mathrm{d}s^2 = g_{\mu\nu}\mathrm{d}x^\mu\mathrm{d}x^\nu. \tag{1.3}$$

Here, $g_{\mu\nu}$ is the metric that contains all the information on the spacetime curvature. One of the most important equations in GR, the Einstein field equations, describe how matter and energy curve spacetime. Its expression is

$$R_{\alpha\beta} - \frac{1}{2}g_{\alpha\beta}R = \frac{8\pi G}{c^4}T_{\alpha\beta}. \tag{1.4}$$

On the left side of the equations, the Ricci curvature $R_{\alpha\beta}$ describes the curvature of a manifold and the Ricci curvature scalar R is the trace of $R_{\alpha\beta}$. $R_{\alpha\beta}$ and R, together with metric tensor $g_{\alpha\beta}$, are combined into the Einstein tensor $G_{\alpha\beta}$ which specifies the geometry of spacetime. On the right side of the equations, $T_{\alpha\beta}$ is the stress-energy tensor, which describes the distribution of all forms of matter

and energy. Although the Einstein equations look elegant and compact, unlike Maxwell's equations, they are nonlinear. In addition, on the right side of the equations, the stress-energy tensor $T_{\alpha\beta}$ depends on the metric tensor $g_{\alpha\beta}$. When one tries to solve the Einstein equations, the unknown coefficient $g_{\alpha\beta}$ appears on both sides of the equations. Because of the nonlinearity of Einstein equation and the dependence between $T_{\alpha\beta}$ and $g_{\alpha\beta}$, it's extremely difficult to get a complete analytic solution of the Einstein field equations.

1.2 Gravitational waves in the Weak-Field Approximation

There are several approaches to solving Einstein equations. Under some particular circumstances such as symmetry, particular exact solution can be obtained. Alternatively, if the spacetime geometry differs only slightly from flat spacetime, the complete solutions of the Einstein equations can be obtained by the *Weak-Field Approximation*. Under this weak-field condition, the nonlinear Einstein field equations become approximately linear.

At a place far away from the gravitational wave (GW) source that $T_{\alpha\beta} = 0$, the metric can be considered as a perturbation of flat spacetime. It can be written as

$$g_{\alpha\beta} = \eta_{\alpha\beta} + h_{\alpha\beta}, \quad |h_{\alpha\beta}| \ll 1, \tag{1.5}$$

where $\eta_{\alpha\beta}$ is the Minkowski metric which represents flat spacetime and $h_{\alpha\beta}$ is a very small perturbation on this flat space-time metric. Note that the components of the tensors above depend on the chosen coordinates, and the freedom in the choice of coordinates is named *gauge* freedom. GR is a theory with gauge freedom, and by carefully choosing suitable coordinates in which to express the Einstein equations, the computation on the equation can be much simplified. With $|h_{\alpha\beta}| \ll 1$, the inverse of $g_{\alpha\beta}$ is given to first order by

$$g^{\alpha\beta} = \eta^{\alpha\beta} - h^{\alpha\beta}. \tag{1.6}$$

In order to simplify the form, the trace-reversed metric perturbation is defined as:

$$\bar{h}_{\alpha\beta} = h_{\alpha\beta} - \frac{1}{2}\eta_{\alpha\beta}h, \tag{1.7}$$

where $h = \eta_{\alpha\beta}h^{\alpha\beta}$. With gauge freedom, one can use the Lorenz gauge:

$$\bar{h}^{\alpha\beta}{}_{,\beta} = 0. \tag{1.8}$$

After neglecting the quadratic and higher terms in $h^{\alpha\beta}$, the Einstein field equations give rise to a linear wave equation for $\bar{h}_{\alpha\beta}$:

$$\left(-\frac{\partial^2}{\partial t^2} + \nabla^2\right)\bar{h}^{\alpha\beta} = 0. \tag{1.9}$$

The solution to Equation (1.9) are gravitational waves. Using the transverse-traceless (TT) gauge, one obtains the plane wave solution of the form:

$$h_{\alpha\beta}^{\mathrm{TT}} = \mathcal{A}\mathbf{e}_{\alpha\beta}\exp(ik_\sigma x^\sigma), \tag{1.10}$$

where $\mathcal{A}$ is the GW amplitude, $\mathbf{e}^{\alpha\beta}$ the 4×4 polarization tensor and k^σ the four dimensional wave vector $(\omega/c, k^1, k^2, k^3)$. By choosing the direction of wave propagation along the z-axis, $k^\sigma = (\omega/c, 0, 0, \omega/c)$, one then can obtain the equation solution:

$$h_{\alpha\beta}^{\mathrm{TT}} = \begin{pmatrix} 0 & 0 & 0 & 0 \\ 0 & h_+ & h_\times & 0 \\ 0 & h_\times & -h_+ & 0 \\ 0 & 0 & 0 & 0 \end{pmatrix} e^{i\omega(t-z)} . \tag{1.11}$$

In Equation (1.11), h_+ and $h_\times$ are the "plus" and "cross" polarization amplitudes of the gravitational wave in the TT gauge.

The small perturbation tensor on flat spacetime $h_{\alpha\beta}$ is symmetric, so it has 10 degrees of freedom. By imposing the Lorenz gauge, it is reduced to 6 degrees of freedom. Then, by choosing transverse-traceless gauge, the number of degrees of freedom is reduced again from 6 to 2, which are the two modes of polarization of a gravitational wave. In GR, there are only two independent polarizations. However, in alternative theories of gravity, the number of polarization modes of a gravitational wave can go up to 5 (more details can be found in [176, 135]). In this thesis I will discuss the questions only in the context of GR.

1.3   Effects of gravitational waves on free particles

In order to examine the effects of the two polarizations of a gravitational wave, let's consider a circle of freely falling particles in space. The circle of particles is in the (x, y)-plane and the gravitational wave travels in the z-direction. When the gravitational wave passes through the (x, y)-plane, it causes the circle of particles to compress and stretch into an ellipse. As shown in Figure 1.2, the $+$ and $\times$ polarized gravitational waves compress and stretch the circle along different orientations separated by 45 degrees. The distortions in the perpendicular directions are equal, so the area of the ellipse is the same as that of the original circle. In addition, no matter what the size of the original circle is, the shape of the deformation is always the same. The measured relative change in distance between particles is the dimensionless gravitational wave strain:

$$h(t) = \frac{\delta L(t)}{L}. \tag{1.12}$$

Here, $\delta L(t)$ is the imposed distortion on the circle due to the gravitational wave and L is the radius of the original circle. In Section 1.4, it will be shown that the strongest expected strain of gravitational waves from astrophysical sources effecting on Earth-based GW detectors is $\sim 10^{-21}$. In Chapter 2, it will be shown that if mirrors approximately freely hang inside of a kilometer-scale detector, then as a gravitational wave pass through, the displacement between mirrors $\delta L \sim 10^{-18}$m would be measured. I want to note that, another concept – the gravitational wave amplitude – will be mentioned in the following sections of this thesis. The gravitational wave amplitude is also dimensionless. It is defined as twice the gravitational wave strain.
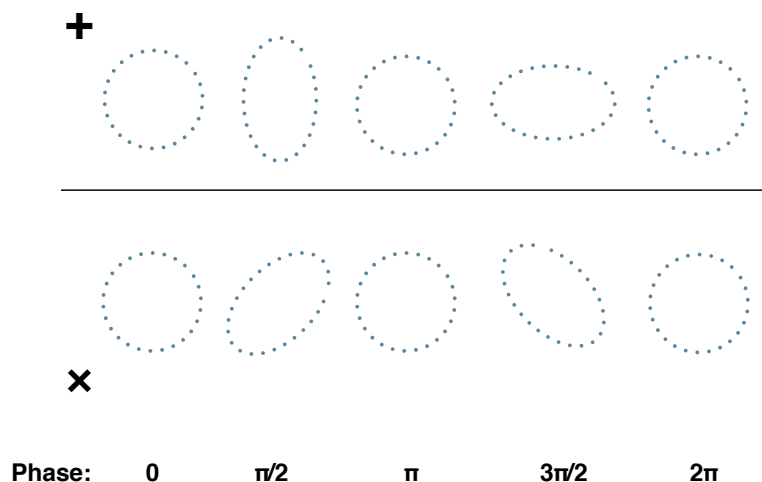
Figure 1.2: The effect of a gravitational wave consisting of only one polarization + or × on a circle of freely falling particles. As the gravitational wave travels in the z-direction, into the plane of the circle, it compresses and stretches spacetime. The two polarizations, + and ×, differ in the upper and lower halves. The + and × polarizations are rotated by 45 degrees. Note that the gravitational wave polarizations are invariant under a π radian rotation. In the context of quantum gravity it means the exchange particle for gravity, so the spin of graviton is $2\pi/\pi = 2$.

It's natural to ask why the effects of a gravitational wave are so tiny. Similar to how conservation of charge forbids monopole radiation in electromagnetism, conservation of mass-energy prevents monopole radiation in gravitational radiation. Gravitational radiation produced by an accelerated mass dipole is forbidden by conservation of linear and angular momentum. Therefore, the first multipole that produces gravitational radiation is the accelerating mass quadrupole with an amplitude [160]:

$$h \approx \frac{2G}{c^4} \frac{\ddot{Q}}{D},$$ (1.13)

diminished by the c^{-4} factor due to the high multipole. In Equation (1.13), G is the gravitational constant, c the speed of light, $\ddot{Q}$ the quadrupole's derivatives with respect to time and D is the distance between the source and the detector.

1.4 Astrophysical sources of gravitational waves

Strictly speaking, gravitational waves can be produced from any accelerating mass with a varying quadrupole. One can just gently wave one's own hand to disturb the local spacetime and thus generate a gravitational wave. Before discussing the astrophysical sources of gravitational waves, let's
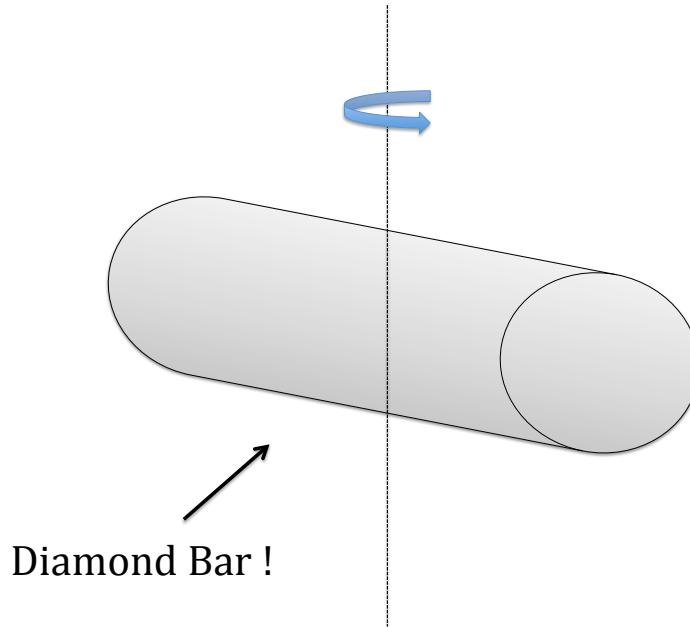
Figure 1.3: An 11-ton diamond bar (4 m length and 1 m diameter) spinning at its maximum frequency 5210 Hz before the the centrifugal force tears up the bar in the middle. For an observer 20 m away, one obtains a gravitational wave amplitude of $h \approx 2 \times 10^{-30}$ (setting aside the impracticality of the size of this diamond and such a fast bar rotation).

consider the possibility of detecting a gravitational wave that is produced in laboratory. After all, a detector can be installed in the next laboratory so the distance between source and detector wouldn't be astronomical. This sounds promising.

Let's say I have an unlimited budget with which to build a gravitational wave source. The physical model of this gravitational wave source is very simple – a spinning diamond bar. The reason I choose diamond is not because it is fancy, but because diamond's cubic crystal structure gives the highest tensile strength so that the diamond bar won't be destroyed by the great centrifugal force it experiences when it's rapidly spinning. Using an atomistic approach, one can get the theoretical upper limit on the tensile strength of diamond: 190 GPa [96]. Neglecting the existence of such a huge diamond in Nature, here I arbitrarily assume a length of 4 m and a circular cross-section with a diameter of 1 m. When the bar is spining at a frequency of 5210 Hz, the centrifugal force overcomes the tensile strength and tears up the diamond bar in the middle circular section. The gravitational wave amplitude this diamond bar emits is given by the formula:

$$h = \frac{4\pi^2 G}{c^4} \frac{I_{zz} f^2 \varepsilon}{D} \ . \tag{1.14}$$

Here, I_{zz} is the principal moment of inertia of the bar which is $1.46 \times 10^4\,\mathrm{kg\,m^2}$ in our case and ε the ellipticity of a ellipsoid which in our case can be approximately taken as 1. The f in Equation (1.14) is the gravitational wave frequency which is twice the rotational frequency and D is the distance between source and detector which I take to be 20 m here[1]. Using these numbers in Equation (1.14), I get the gravitational wave amplitude emitted by my maximally spinning diamond bar:

$$h \approx 2 \times 10^{-30}. \tag{1.15}$$

Even made of the strongest material in the world, the gravitational wave amplitude that the spinning bar emits is still far below the sensitivity of current detectors (10^{-21}). Thus the only possibility to detect gravitational waves comes from the sky.

For decades, astrophysical gravitational wave sources have interested many physicists. What kind of gravitational wave sources can be seen by the detectors becomes one of the most important questions to answer. The knowledge of promising gravitational wave sources helps us decide what kind of detector we should design and build, an undertaking that needs substantial investment. On the other hand, in the data analysis, a good knowledge of sources can allow us to predict accurate waveforms which helps us to recognize the weak gravitational wave signal against the noise of detectors.

As I discussed in Section 1.3, the GW sources must have an accelerating quadrupole. Therefore, spherically symmetric GW sources, such as a radially pulsating star, can't produce GWs. There are many astrophysical objects and phenomena that can produce GWs that could be detected by the current generation of GW detectors: (1) compact binary coalescences, (2) rapidly spinning compact objects, (3) stellar explosions and (4) the Big Bang. Here I will give a brief review of them (Section 3.1 of [162] as reference).

1.4.1 Compact binary coalescences

Binary systems have provided the best evidence of the validity of General Relativity. The most famous example is the orbital evolution of the binary system PSR1913+16. In 1974, Russell Hulse and Joseph Taylor discovered this binary system consisting of a pulsar and another neutron star. Due to the stable timing of the pulsar, the orbital period of this system could be measured with unprecedented precision. After decades of radio observation, the decay of the orbit from the loss of energy due to gravitational radiation was proven to agree with the decay predicted by GR within the measurement errors (see Figure 1.4) [172]. This result indirectly proved the existence of gravitational waves and gave gravitational wave scientists more confidence in their efforts toward making a direct detection. In 1993, Hulse and Taylor were awarded the Nobel Prize for their discovery.

However, the GW radiation from a system such as the Hulse-Taylor binary is strong enough for a direct detection with current ground-based detectors only when the system is at the final phase of inspiral, which will happen in 300 million years. At this final inspiral phase, the binary is much closer and the radiated GW power is much higher. The signal produced by the binary system at inspiral is commonly known as a chirp: as the orbit decays, the frequency and strain of GW increases (see Figure

---

[1] The GW amplitude given by Equation (1.14) requires the distance to be many wavelengths. Here the obtained amplitude at 20 m away is not strictly true which can be only considered as an approximation.
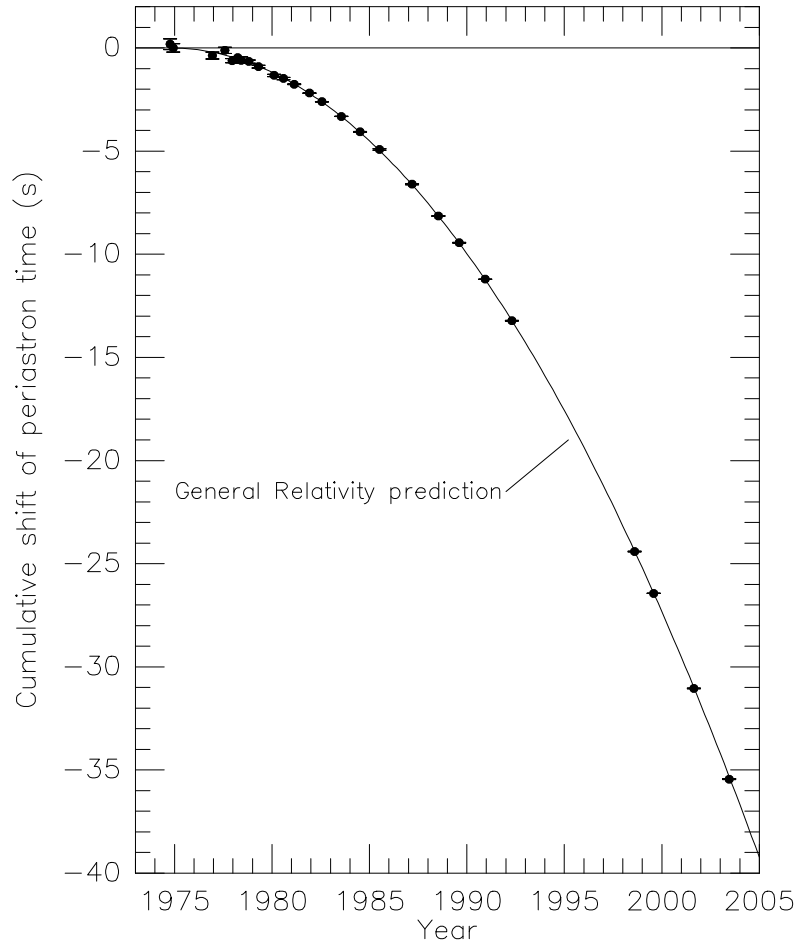
Figure 1.4: Decay of orbit of PSR1913+16. The data points are observational results which are well matched with the predication of General Relativity. Figure credit:[172]
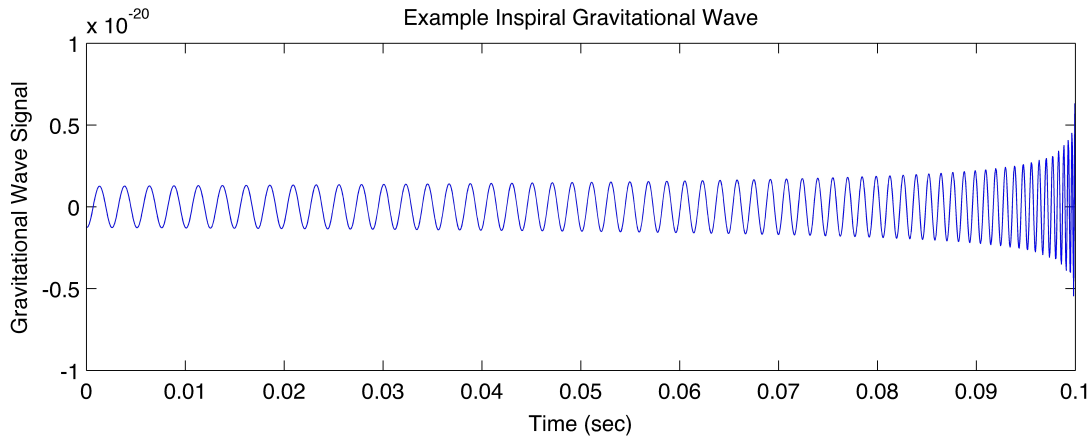
Figure 1.5: An example waveform from an inspiral gravitational wave source source. Figure credit: A. Stuver/LIGO

1.5). Shortly after the final inspiral, these two compact objects collide with each other in a process called coalescence. Therefore, this type of signal is referred to as a compact binary coalescence (CBC). The "compact" here refers both to the small distances between the objects in the binary system and to the objects themselves.

The components in compact binary systems are either neutron stars (NSs) or stellar mass black holes (BHs). Both are the remnants of massive stars after supernova explosions. The BH-BH coalescence is thought to be observable only through gravitational waves. In contrast, NS-NS and NS-BH coalescences may produce electromagnetic signals which can be observed to confirm the GW event.

CBCs are considered the most promising source for the detection of GWs because of the three following reasons.

- Firstly, the GW radiant power is very huge at the very short time before compact binary become into one.

- Secondly, the signal waveform of a compact binary coalescence can be accurately modeled. During the inspiral phase, the post-Newtonian approach and effective-one-body (EOB [91]) method are effective in modelling the GW signals. When the two components reach their last few stable orbits, their motion becomes relativistic and the post-Newtonian and EOB approaches begin to fail. That physical process can be investigated via numerical relativity. Since we use the match filtering method to analyse the GW signal, a reliable CBC waveform is helpful for detecting these types of signals.

- Finally, coalescences of systems with masses between $\mathcal{O}(10)$-$\mathcal{O}(10^2)$ solar mass are estimated to happen at the rate of at least a few per year with the horizon of the current generation of the ground-based detectors.

In the future, when the space-based detector LISA (see Section 2.3) comes online, its better sensitivity at lower frequencies will allow for the observation of the earlier inspiral phase. Hence, astrophysicists will know exactly when and where these two components merge and electromagnetic observatories will have enough time to aim at that direction and wait for the exciting moment.

Recently, GW signals from binary black hole coalescences have been detected for the first time ever[58, 57] (details in Section 2.2.4). These detections indicate a higher BH-BH event rate than previously expected and will improve our understanding of the processes for the formation of massive-star binaries.

1.4.2   Spinning compact objects

Spinning compact objects are another promising GW source. Neutron stars or other extreme compact objects are thought to have distortions that can break their axisymmetries. Thus, these spinning compact objects with a "bump" emit quadrupolar GW radiations. There are at least two physical mechanisms that can support such distortions. The first one has the distortion supported by the star's crust or magnetic field [77]. The second process has the distortion generated by the "hot spot" supported by the accretion onto a neutron star in a binary system. The accretion not only generates the distortion on the star but can also sustain the star's rotation [79]. The gravitational waves produced by spinning neutron stars are only very slowly changing in frequency and strain (sinusoidal, see figure 1.6) and last for a long time. This type of gravitational waves is hence referred to as a continuous gravitational wave (CW).

The frequency of a CW signal is twice the spin frequency of the star. Signals are expected in the range $\mathcal{O}(10)$-$\mathcal{O}(10^3)$ Hz, which is covered by the current generation of ground-based detectors. In spite of the waveforms being well known, because of the weak strength of CWs, long integration durations (usually from months to years) are required to make a detection above the noise. As a consequence, CW searches are very computationally expensive. Recently, a search for 200 known pulsars has been published [62], and so far no GW signal from this type of source has been detected yet.

As the continuous wave is the main topic of this thesis, I won't elaborate on it further in this subsection. Much more details on NS physics and CW searches will be given in Chapter 3.

1.4.3   Stellar explosions

Supernovae (SN) explosions are some of the most violent events known in the Universe. At the end of the life of a massive star, a supernova explosion is triggered by the gravitational collapse of the star's inner core. A huge amount of energy (mostly in the form of neutrinos) is released in the collapse; this blows off the envelope of the star and leaves behind a neutron star or black hole. Physical models of SN explosions show that asymmetries can take place in this process [109], which indicates that a fraction of the released energy can be in form of GWs.

Unfortunately, due to the poor understanding of the complicated internal physics, the GW signal waveforms from a supernova explosion are very uncertain. Assuming that 1% of the released energy is in form of gravitational radiation, the strain h of a supernovae explosion at the distance of the
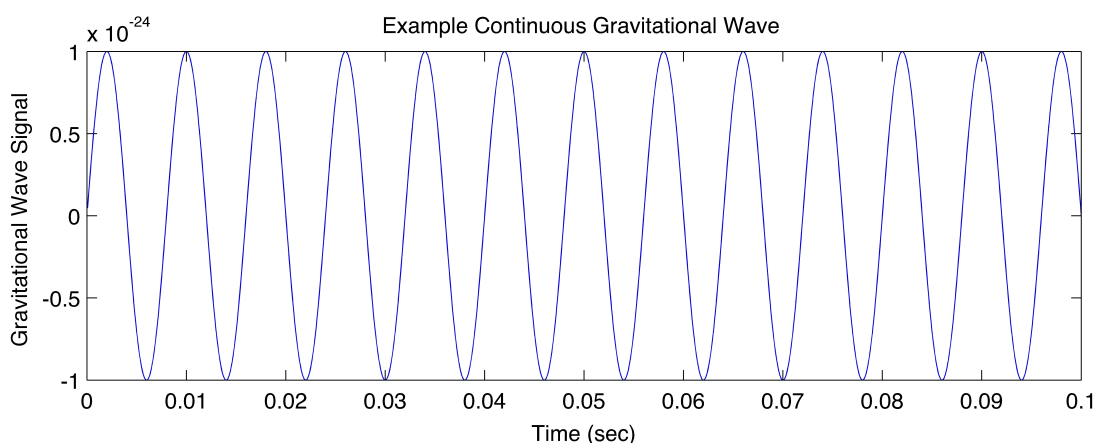
Figure 1.6: An example waveform from a CW source. Figure credit: A. Stuver/LIGO

Virgo Cluster (18 Mpc) reaches 10^{-21} which is high enough to be detected by current ground-based detectors [162] (see Figure 1.7). The duration of this waveform is usually assumed to be less than about 1 second, so the search for the GW from supernovae explosion is called a burst search.

1.4.4 The Big Bang and the stochastic background

The Big Bang is thought to be the most violent event from the beginning of the Universe. The quantum fluctuations from the Big Bang are expected to produce a enormous amount of gravitational radiation [102]. Like the cosmic microwave background (CMB), this GW emission from the early evolution of the universe gives rise to a stochastic background. This background is called the cosmic gravitational wave background (CGWB). Detecting the CGWB will provide us with unique information on the earliest moments of the universe (approximately 10^{-36} to 10^{-32} seconds after the Big Bang). However, the frequency range of the CGWB is extremely low (10^{-20} to 10^{-15} Hz), which can't be detected by any current or planned interferometric detector. Around the world, the BICEP team [2] and the Ali team [87] are aiming to measure the B-mode polarisation of the CMB which can be evidence for the existence of the CGWB.

The superposition of signals from individual sources (such as spinning NSs) is a stochastic background as well [65]. The stochastic background has similar characteristics as the random noise of the detectors and is expected to be even weaker than this noise. Detecting this weak stochastic background requires two or more detectors, so that one can correlate the detectors' outputs (multiplying them and integrating in time). Because the randomness of the stochastic background is correlated between detectors, the signal noise ration (SNR) increases as a function of the integration time T. In contrast, the noise from detectors at different locations is independent, so it would increase as a function of integration time $\sqrt{T}$. Due to the wide frequency range of the stochastic background (from below 10^{-17} Hz up to 10^{-8} Hz and higher), it is of interest to not only the ground-based interferometric detectors but also the space-based detectors like LISA and pulsar timing arrays (PTA).
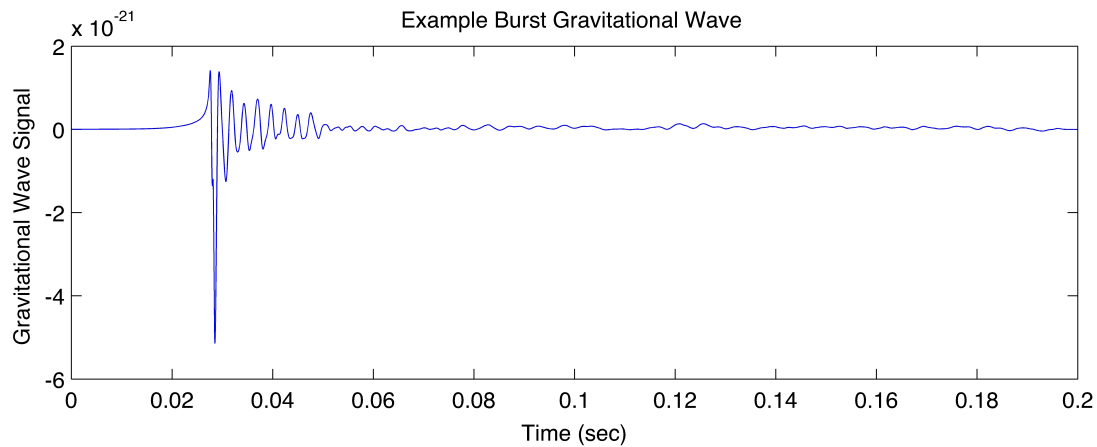
Figure 1.7: An example GW waveform from a supernovae explosion. Note that, due to the poor understanding of this type of waveform, the figure here is just showing the basic picture. Figure credit: A. Stuver/LIGO

1.4.5   Other potential sources

Other potential GW sources haven't been mentioned above, such as an intermediate-mass black hole capturing a star [129], the coalescence of super-massive black holes (SMBHs) [169], cosmic strings [34] and so on. In this thesis, I do not intend to describe or comprehend all of them. What I want to emphasize here is that, as GW astronomy is a completely new window for us to observe the Universe, it won't be surprising if in the future we find exotic sources those are unknown to us as yet. We will see them!

Chapter 2

Gravitational wave detectors

In 1886, the German physicist Heinrich Hertz established the existence of electromagnetic waves and since then a revolution of communications has transformed our lives. While writing this thesis, I check my cellphone from time to time. Any cellphone is a radio receiver (as well as a radio transmitter). A gravitational wave receiver or detector is analogous to a radio receiver, except that electrons moving freely in conductors are replaced by test masses falling freely in space. In this chapter, I will give an overview on the gravitational wave "receiver".

The following sections begin with a brief overview on resonant mass detectors in Section 2.1. Then, a relatively detailed introduction on the currently most widely used and promising GW detectors – ground-based laser interferometric detectors – is given in Section 2.2. Next, a brief description of the space-based laser interferometric detectors is given in Section 2.3 and of pulsar time arrays (PTAs) in Section 2.4. At the end of this chapter, I will summarize GW detectors and briefly discuss GW astronomy.

2.1 Resonant mass detectors

The history of building gravitational wave detectors starts with resonant mass detectors. In the 1960s at the University of Maryland, Joseph Weber built the first gravitational wave "bar" detector. It was a 2-ton cylinder of aluminium with a resonant frequency of 1660 Hz and operated at room temperature [171] (Figure 2.1). The bar detector can be idealised as a pair of point masses connected by a mechanical spring. The stiffness of the spring determines the longitudinal resonant frequency of the bar detector. When a gravitational wave with energy at the resonant frequency passes vertically through this bar, it will trigger the resonance of the bar. Piezoelectric crystals on the surface of the bar respond to the vibrations and the signal is read out. The earliest bar detector had a modest sensitivity ($\sim 10^{-14}$) which is far above the sensitivity required to detect any GW event.

After the pioneering attempts by Joseph Weber, many other bar detectors were built. The best bar detectors of today are orders of magnitude better in sensitivity than the original Weber bar. A network of five cryogenic resonant detectors, the International Gravitational Event Collaboration (IGEC) [73] started to run in 1997. These five detectors are: ALLEGRO in Louisiana, USA [130], AURIGA in

Figure 2.1: Joseph Weber and his resonant mass detector. Figure credit: University of Maryland Libraries

Padova, Italy [88], EXPLORER in Geneva, Switzerland [74], NAUTILUS in Rome, Italy [74] and NIOBE in Perth, Australia [81]. All these bars are usually kept oriented to the same sky direction to optimize the GW signal correlation. In addition, spherical resonant detectors such as MiniGRAIL [101] and Schenberg [64] have also been built. Because of that spherical shape, they have the omnidirectional sky sensitivities so that all 5 independent GW polarization modes can be monitored and the entire sky can be observed. Resonant mass detectors have a main disadvantage compared with interferometric detectors: the narrow frequency bandwidth. The "dual" detector proposed by the AURIGA group might partly overcome this disadvantage [82].

2.2   Ground-based laser interferometric detectors

While resonant mass detectors were being built around the world, several groups were developing another type of detector: the Michelson laser interferometer. The feasibility of using interferometers as detectors had been considered by Weber in 1960s, but due to the state of the technology at that time, he went with resonant bars instead. However, only 15 years later, the technology needed for laser interferometric detectors had greatly improved. Between 1980 and 1994, interferometric detectors were investigated and developed at MIT, Glasgow University, Caltech, Max Planck Institute for Quantum Optics and University of Tokyo. These detectors were the prototypes of modern interferometric detectors, with sensitivities that reached $\sim 10^{-18}$ [159].
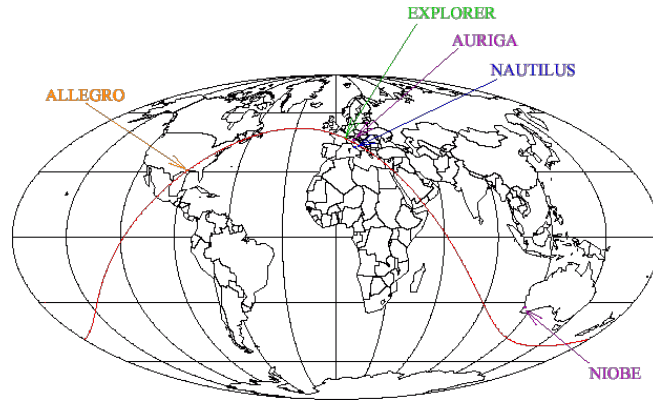
Figure 2.2: Locations of the five cryogenically cooled bar detectors in the world that participated in the IGEC. Figure credit: [3]

2.2.1 The physics of interferometric detectors

The basic concept of a Michelson laser interferometric detector is shown in Figure 2.3. The detector has two perpendicular arms of equal length L. Where the arms meet, there is a beam splitter which splits coherent light into two beams. On the far ends of the arms, two mirrors are installed as test masses. Instead of falling freely, these two mirrors hang as pendulums. Thus, in the horizontal plane, the motion of the mirrors is approximately free. When a gravitational wave passes through the detector, the lengths of the arms change and thus the two beams are no longer in phase. By measuring the difference in the interference pattern, one can know the incoming GW's strain. The relation of δL to the gravitational wave strain h is given by Equation (1.12).

So far I have only discussed the basic concept of an interferometric detector. In reality, the interferometric detectors are built to store light in both arms so that the light reflects more than once (see Figure 2.4). With two additional mirrors in each of the arms, the beams are reflected multiple times. This modification is called a Fabry-Perot cavity. The main advantage of such a design is that the beam gains an additional phase shift with each reflection which is equivalent to increasing the length of the arm. However, this doesn't necessarily mean that we can build shorter arm length detectors and compensate with more beam reflections, because each reflection introduces more noise from the mirrors. Most of the current interferometric detectors have arms with lengths of kilometers, a good balance between sensitivity and construction cost. The frequency range of these ground-based interferometric detectors is typically $\mathcal{O}(10)$-$\mathcal{O}(10^4)$ Hz.

no GW

Test Mass

Test
Mass

Beam
Splitter

Photo
Detector

Laser

(a) No gravitational waves

GW arrives

Test Mass

Test
Mass

Beam
Splitter

Photo
Detector
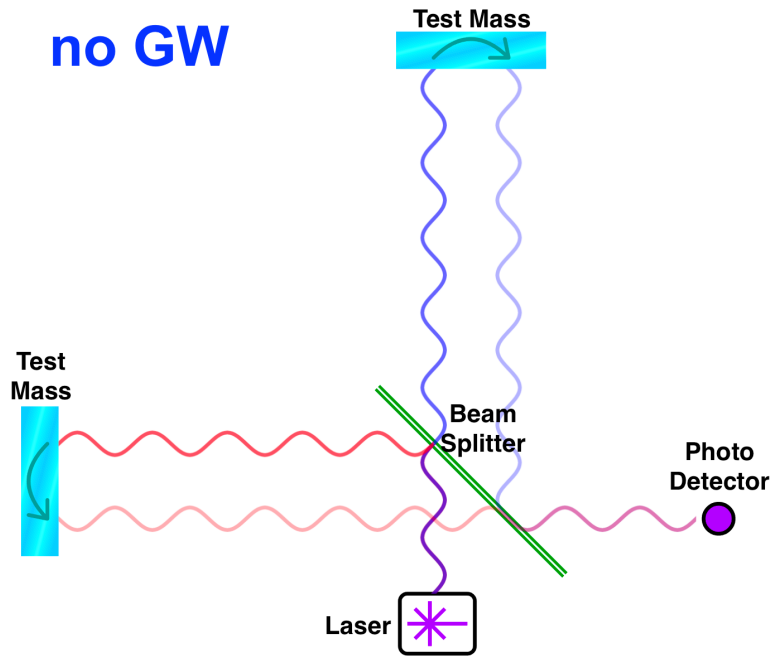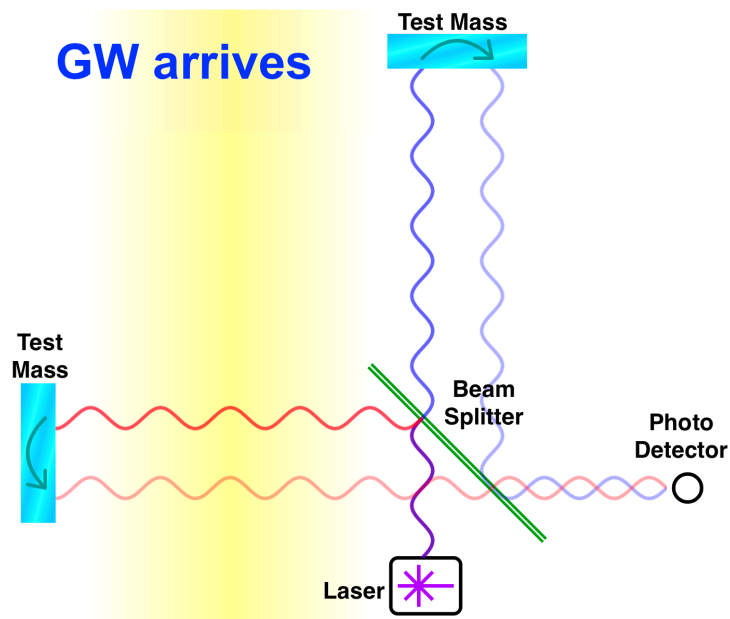
Laser

(b) Gravitational waves come through detector

Figure 2.3: The basic concept of a Michelson laser interferometric detector. A beamsplitter splits coherent light into two beams which reflect off the mirrors (test masses). Figure (a): In the case of no GW, the two reflected beams recombine and an interference pattern is detected. Figure (b): In the case that a gravitational wave moving in the direction perpendicular to the plane of the page), It changes the length of the left arm and the interference pattern changes. Figure credit: [4]
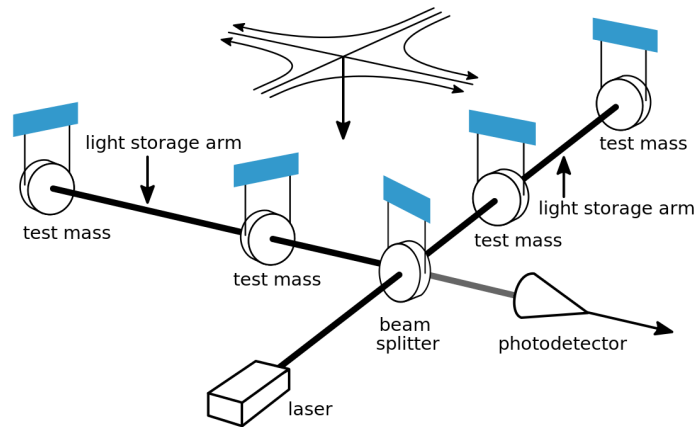
Figure 2.4: Schematic of a LIGO detector: a laser interferometer with light storage arms. Figure credit: LIGO Scientific Collaboration.

On the subject of detector noise, the history of interferometric detector development can be described as the history of the "war" between experimental physicists and detector noise. Since GWs have extremely weak strains, in order to detect them, the noise in detectors has to be suppressed to a very low level. There are three main sources of noise in interferometric detectors: seismic, thermal and quantum, which are briefly described below (based on Chapter 4.3 of [159]).

- **Seismic noise.** This type of noise encompasses all kinds of ground vibrations and mechanical vibrations coupling with the detector, such as seismic activity in the Earth. Because seismic noise typically decreases rapidly with frequency, it's the main limiting factor at low frequencies ($\leq$ 100 Hz). Multi-stage pendulum suspensions are the mechanisms used in the seismic isolation system. In the Advanced LIGO detectors, this system attenuates the ground motion by seven orders of magnitude [56] so the seismic noise in the detectors is negligible above 10 Hz. At frequencies below 10 Hz, interferometric detectors reach the seismic noise "wall", and current technology has no good solution yet.

- **Thermal noise.** Most of the current interferometric detectors are working at room temperature, so thermal noise is present in all components of those detectors, most notably in the mirrors and in the suspending pendulums. There are two ways to control thermal noise. The first method takes advantage of the fact that thermal noise is highest at the frequency of the vibrational mode of pendulums and mirrors, and when the resonance of this mode is narrow (high quality factor), then the thermal noise at other frequencies is small. This is why the suspending pendulums were designed to have the vibrational mode around 1 Hz (well below the observation frequency range) and the mirrors with the vibrational mode above 1 kHz (well above the observation frequency range). Systems with high quality factors (10^6 or more) are used to attenuate the noise in the
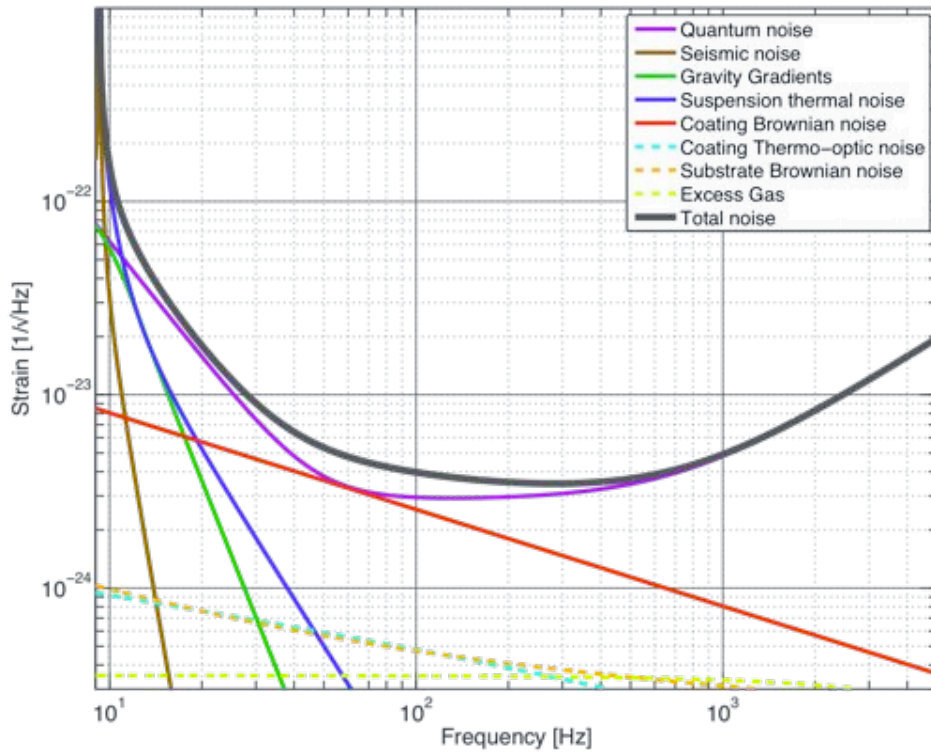
Figure 2.5: Main sources of noise of Advanced LIGO. Quantum noise includes both shot noise and radiation pressure noise and it dominates across almost the entire observation frequency range. This is the main noise that must be reduced in interferometers of future generations. Seismic noise from the ground causes mechanical vibration that are attenuated through the seismic isolation system and the suspensions. Seismic noise is dominant below 10 Hz. Suspension thermal noise and coating brownian noise (from the mirrors) are the two components of thermal noise, which is dominant at around 100 Hz. Gravity gradient noise arises from perturbations of the local gravitational field gradient. This noise is dominant below 1 Hz. Figure credit: LIGO Scientific Collaboration [125].

observation frequency range. However, the thermal noise still dominates around 100 Hz. The second approach to reduce thermal noise is to use cryogenic detectors like KAGRA [5, 165]. KAGRA will be operated at 20 K temperature at which thermal noise can possibly be reduced by one order of magnitude.

- **Quantum noise.** Quantum noise includes shot noise, which arises from statistical fluctuations of the number of photons on a photodetector in a given time interval, and radiation pressure noise on mirrors due to photon-number fluctuations.

  The photon number fluctuation is proportional to the square root of number of photons $\sqrt{N}$, while the signal is proportional to the number of photons N. Thus, the shot noise – which can be also understood as the minimum detectable signal – is proportional to $1/\sqrt{N}$. Shot noise is dominant at high frequency because higher frequencies correspond to a shorter time interval during which the $\sqrt{N}$ is smaller. In contrast, radiation pressure noise is proportional to the square root of photon number $\sqrt{N}$ and therefore dominant at low frequencies because of the longer time interval.

  In order to reduce shot noise, a high-power continuous laser is needed. Unfortunately, the power that current laser technology can provide is far below the requirement of a GW interferometric detector. A technique called power recycling is gerenally used to solve this problem. A power recycling mirror is placed between the laser and the beamsplitter, thus the waste light is reflected back into the interferometer and the required power (750 kW in each arm cavity) is achieved. However, no matter how much the light power is increased in the cavity, there is a frequency-dependent but power-independent lower bound on the detector's sensitivity, which is called the Standard Quantum Limit (SQL) [80]. A series of approaches have been discussed or proposed to overcomes the SQL, such as quantum non-demolition detector [157, 158], squeezed light [131], radiation pressure noise cancellation [120] and modifying test mass dynamic with optical spring effect [86]. Some of these are expected to be used in interferometers of future generations.

The noise sources mentioned above dominate in the current ground-based interferometric detectors. There are a few other, subdominant noise sources. For example, gravity-gradient noise, arises from perturbations of the local gravitational field gradient. Within the observation frequency range (10 Hz to a few kHz) of ground-based interferometric detectors, gravity-gradients noise is negligible compared to the other three main noises. However below 1 Hz, the gravity gradient changes due to surface ground motion or atmospheric pressure changes become significant. This is the reason for using space-based interferometric detectors to observe the GW Universe below 1 Hz (Section 2.3).

GW detectors' sensitivities entirely depend on the combination of all types of noise (including noise sources not mentioned above) and many great efforts have been made to improve sensitivity. In the next section, I present a brief review over the existing and planned interferometric detectors and their sensitivities.
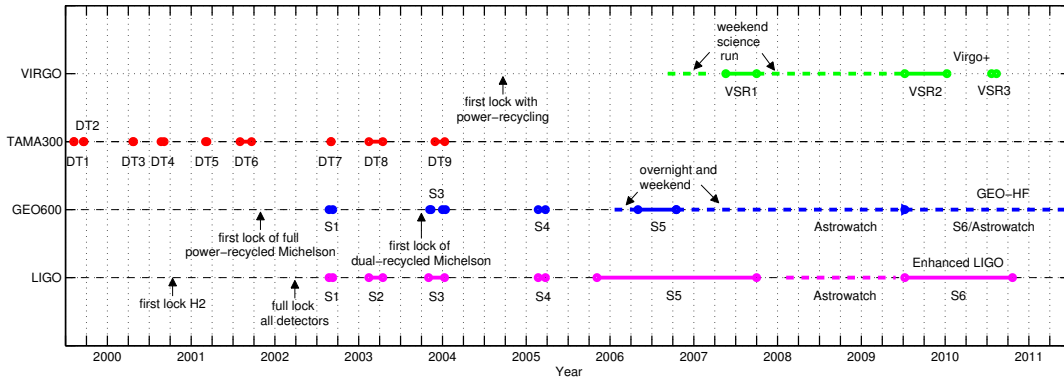
Figure 2.6: A timeline of science runs of the first-generation ground-based interferometric detectors. Figure credit: [147].

2.2.2   Existing and planned interferometric detectors

In the mid-1990s, multiple long-baseline interferometric detectors were being built worldwidely by different groups. Compared with the initial prototypes, the arm lengths were much longer (typically, from a few hundred meters to a few thousand meters). After years of construction and experimental study, the detectors began to take data in the early 2000s with sensitivities of around 10^{-21} over a frequency band $\mathcal{O}(10)$-$\mathcal{O}(10^3)$ Hz. In the first decade of this century, several commissionings and improvements to these detectors have been carried out and the detector sensitivities have hence been improved at each stage. Figure 2.6 shows a timeline of the science runs of these detectors. The six detectors[1] are the so-called first-generation interferometer ground-based detectors and a brief introduction to each of them is given below (Section 2.2.1 of [162] as reference).

- **TAMA300** [6] (Japan) has two 300-m arms and is located at the Tokyo Astronomical Observatory. Construction of TAMA300 started in 1995, and data started to be collected in 1999 without the power recycling system. After a few improvements, in particular the Fabry-Perot cavity for power recycling, the strain sensitivity was close to $10^{-21}\,\mathrm{Hz}^{-1/2}$ (Figure 2.7). The main goals of TAMA300 were to develop the advanced techniques needed for a future kilometer-sized interferometer (KAGRA) and detect events within the local group of galaxies.

- **GEO600** [7] (Germany and UK) is located near Hannover, Germany. The arm length of GEO600 is 600 m. Compared to other detectors, GEO600 is somewhat different. It was designed to be a detector to test cutting-edge technologies such as the four-pass delay-line system with advanced optical signal-recycling technique and the extremely low loss-fused silica suspensions for the test masses. Despite GEO600's shorter baseline, its sensitivity above a few hundred Hz is comparable to the LIGO and Virgo sensitivities at their first operations. At

---

[1]Virgo, TAMA300, GEO600, and three LIGO detectors.
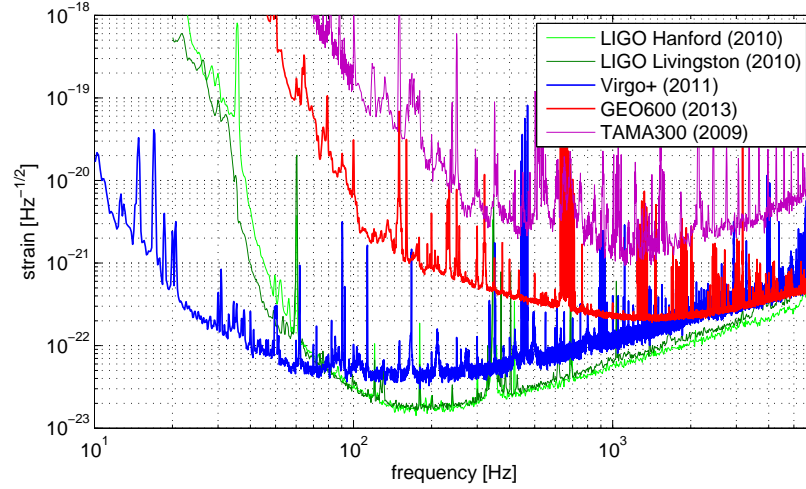
Figure 2.7: Strain sensitivities achieved by the first-generation of ground-based interferometric detectors. Figure credit: [94].

later stages, LIGO and Virgo adopted these advanced technologies that were first developed in GEO600. When the other longer baseline detectors were offline for commissioning or upgrades, GEO600 also served in the so-called "Astrowatch" program.

- **LIGO** [8] (USA) has detectors at two sites: an observatory in Hanford, Washington, houses two detectors, H1 (4 km long) and H2 (2 km long); and an observatory in Livingston, Louisiana, houses the 4 km long L1. Multiple detectors at separate locations are important for rejecting the local environmental artifacts in data. In addition, the wide separations between detectors are required for the localisation of the astrophysical sources. LIGO started the first science observation run (S1) in the middle of 2002 with an initial sensitivity close to 10^{-21} Hz$^{-1/2}$. With the benefit of the longer arm, after several commissionings and improvements on aspects like laser power and mirror quality, during the sixth science run, LIGO (H1) reached an unprecedented sensitivity of $\sim 2 \times 10^{-23}$ Hz$^{-1/2}$ at the most sensitive frequencies (around 150 Hz). Figure 2.8 shows how the sensitivities of initial LIGO have improved at each stage.

- **Virgo** [9] (Italy and France) is a 3 km long detector near Pisa, Italy. After a few years of commissioning, from late 2006 until March 2007, Virgo began 10 weekend science runs (WSRs) for coincident observations with LIGO and GEO600 which were in the S5 run [147]. In May 2007, the first full-time (four month) data taking science run of Virgo (VSR1) started. Like LIGO, Virgo's sensitivity has been improved in stages. In 2011, the upgrade to Virgo, called Virgo+, had a sensitivity level of $\sim 4 \times 10^{-23}$ Hz$^{-1/2}$ around 200 Hz.

The above six detectors formed the first-generation ground-based laser interferometer detector network. Because the components of this network are distributed worldwide, if a GW signal had been
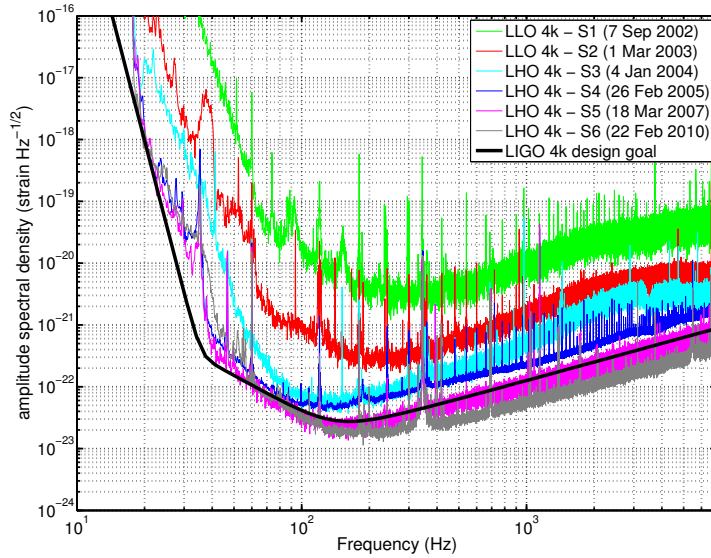
Figure 2.8: The strain sensitivities of initial LIGO from science runs S1 to S6. The LIGO 4 km design sensitivity is also shown. Figure credit: [147].

detected by this network, the sky location could have been determined using the time delay on each detector. In addition, while one detector was undergoing maintenance and construction, the others were able to keep running in an "Astrowatch" mode in case a supernovae or GRB happened nearby. However, due to the extreme weakness of the GW signal, a direct detection of gravitational waves wasn't made by any of these first-generation detectors. Better detector sensitivities are required in order to detect astrophysical GW events.

Powered by the development of GW instrument science, the second-generation of GW detectors has started to come online in recent years. Both LIGO and Virgo reused the infrastructure from the first-generation detectors and enclosed the hardware in an ultra high vacuum system. The upgraded detectors are named Advanced LIGO [104] and Advanced Virgo [63], respectively.

Advanced LIGO started its first observation run (O1) in September 2015, and during those four months of observation two or three GW events were detected by the Advanced LIGO L1 and H1 (more details in Section 2.2.4).

Advanced Virgo is commissioning and will start its first observation run in summer 2017.

Following TAMA300, the brand new 3km interferometer KAGRA [165] was built near Kamioka, Japan. KAGRA is the first underground, cryogenic laser interferometer (see Figure 2.9) and is expected to collect data start in 2018.

GEO600 reused its infrastructure, but carried out a series of upgrades in order to test advanced techniques in a program: GEO-HF [128]. One of GEO-HF's main goals is to improve the detector's high frequency sensitivity above approximately 600 Hz where quantum shot noise is dominant.

Figure 2.9: KAGRA under construction. This panorama photo was taken in June 2014 when I was visiting KAGRA which is located underneath a mountain near Kamioka.

In addition, a planned advanced GW observatory located in India called LIGO-India recently received an in-principle approval from the Indian government. LIGO-India is identical to the other two Advanced LIGO detectors in the US. As a part of the worldwide network, it will increase the accuracy of the sky localisation of the GW sources [10, 108].

These second-generation detectors are expected to have an order of magnitude improvement in sensitivity compared to the first-generation detectors and will form a new network. Figure 2.10 shows the expected noise level, and some of the most important design properties of these detectors are listed in Table 2.1.

While these second-generation detectors were under construction, plans for the third generation of detectors were being developed [153, 155]. The most mature proposal is called the Einstein Tele-scope (ET) [154]. Various aspects of ET have been studied, including the site location (underground), arm length (10 km), suspension technologies, laser, test mass, detector geometry and topology (an equilateral triangle configuration), and astrophysical goals (more details can be found in [156]). ET is expected to yield an order-of-magnitude better sensitivity than the second-generation detectors over a broad frequency band. Furthermore, it will benefit from the underground location and improved seismic isolation, and be able to make observations down to a few Hz. Thus, the ground-based detectors will share an observation window with space-based detectors and combine into a broad seamless observation frequency range from 10^{-8} to 10^4 Hz. In this way, it will be possible to monitor the whole process of a compact binary coalescence, from the early phase of the inspiral until the ringdown (Figure 2.11).

2.2.3 The Advanced detectors

In late October 2010, after initial LIGO finished its sixth and last science runthe era of initial LIGO came to an end and the upgrades immediately began. In the next few years, various aspects of LIGO were improved and tested [13]:

- (1) The laser power was increased from the initial LIGO value of 20 W (S6) to 23 W (O1) to decrease the shot noise.
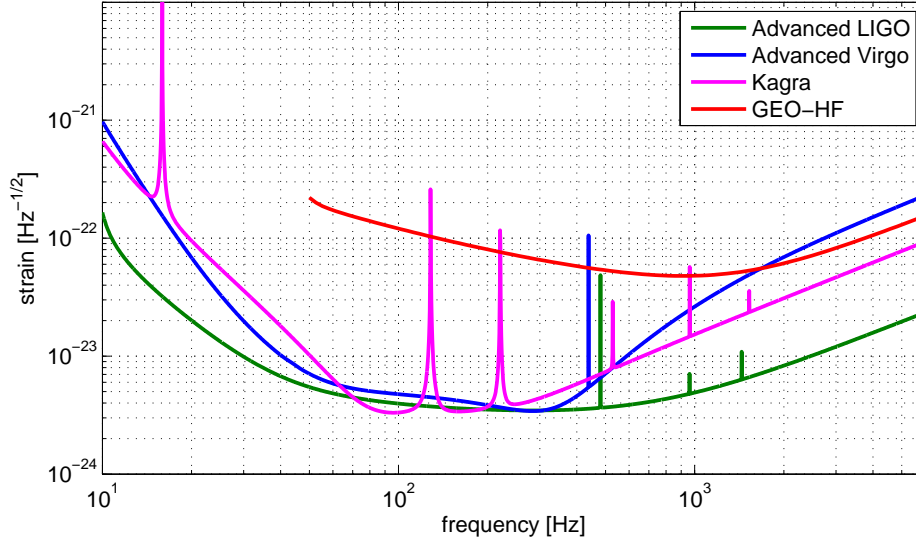
Figure 2.10: Expected sensitivities of the instruments in the advanced detector network. Note that the noise curves of Advanced Virgo and KAGRA assume a detuned model which is optimized for sensitivity to neutron star binaries [63, 165], while the Advanced LIGO and GEO-HF noise curves are without detuning [11, 12]. Figure credit: [94].

Table 2.1: Some design properties of the second-generation ground-based laser interferometric detectors. DRFPMI stands for dual-recycled Fabry-Perot Michelson and GEO is has no arm cavities. Table credit: [94].

	Advanced LIGO	Advanced Virgo	GEO-HF	KAGRA
arm length	4 km	3 km	2×600 m	3 km
power recycling gain	44	39	900	11
arm power	800 kW	700 kW	20 kW	400 kW
# of pendulum stages	4	8	3	6
mirror mass	40 kg	42 kg	6 kg	23 kg
mirror material	fused silica	fused silica	fused silica	sapphire
temperature	room	room	room	cryogenic
topology	DRFPMI	DRFPMI	DRMI	DRFPMI
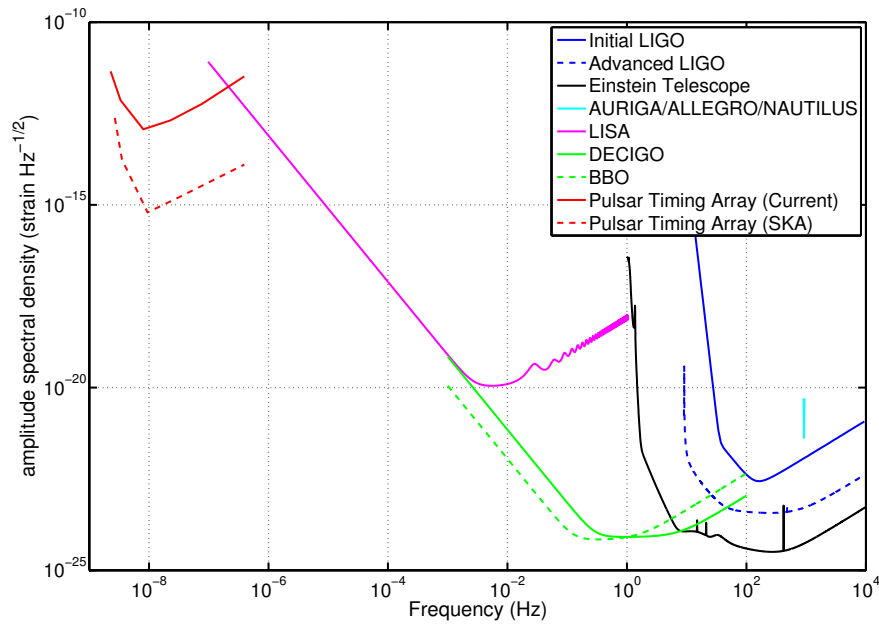
Figure 2.11: Estimated sensitivity curves for various GW detectors across 12 orders of magnitude in frequency. At the lowest frequencies, the pulsar timing arrays are the relevant detectors (more details in Section 2.4). In the middle frequency range are the space-based interferometers LISA, DECIGO and BBO (more details in Section 2.3). At the high frequency range the sensitivities are led by three generations of laser interferometric detectors: LIGO, Advanced LIGO and ET. Sensitivity curves of the bar detectors Nautilus, AURIGA and Allegro are also shown in this Figure. Figure credit: [147].

- (2) The fused-silica test masses (25 cm diameter, 11 kg) in initial LIGO were replaced with larger (34 cm) and heavier (40 kg) ones to reduce thermal noise as well as to keep the radiation pressure noise to a level comparable to the suspension thermal noise.

- (3) The steel wires that held the test masses in initial LIGO were replaced by fused-silica fibers to reduce the suspension thermal noise.

- (4) A new suspension system with four pendulum stages and active servo techniques were applied to the detectors. Together with the replacement of the piers and support tubes which the seismic isolation system is built on, overall the seismic noise of Advanced LIGO was brought down to a negligible level at all observation frequencies.

- (5) The signal recycling mirror was installed. It allows to re-inject the GW signal back into the interferometer for further sensitivity gain and allows to tune the detector for different frequencies.

After ~ 5 years of upgrade and test, on 18 September 2015, the first advanced detector observation run (O1) started. O1 lasted four months and ended on 12 January 2016. The Advanced LIGO sensitivity during O1 is shown in Figure 2.12. The sensitivity of O1 in the low frequency range (≤ 100 Hz) is approximately dozen times better than S6 and in the high frequency range (≥ 100 Hz) is roughly 4 times better. The better sensitivity in O1 resulted in a larger volume of observable sources, with a BNS range[2] of $40 - 80$ Mpc. After 9 months of configuration upgrade and commissioning, on 30 November 2016, Advanced LIGO began its second observation run (O2). O2 will last for 9 months and currently is ongoing. The BNS range in O2 is $80 - 120$ Mpc which gives a BNS search volume of $(0.6 - 2) \times 10^6$ Mpc^3 yr and an expected number of $0.006 - 20$ BNS detections in 6 months [59].

Advanced Virgo is expected to take part in O2 (near the end). The localization accuracy will be improved by this advanced detector network, and follow-up observations of a GW signal will be easier. In future years, more observation runs will be carried out by these advanced detectors. Table 2.2 shows the observation schedule and expected sensitivities of Advanced LIGO and Advanced Virgo. In 2019, Advanced LIGO will reach its full design sensitivity which is approximately 10 times better than the initial LIGO design (Figure 2.12). This means the detectors will be able to observe 10 times further into space, which translates to, 1000 times more GW events.

2.2.4   The first GW event ever: GW150914

In 2016, a full century after Einstein predicted the existence of gravitational waves, the word "Gravitational Wave" suddenly aroused public attention like never before. This is because of the first direct GW detection, GW150914. On 14 September, 2015 at 09:50:45 UTC, during the last commissioning run before O1, the two LIGO detectors H1 and L1 almost simultaneously observed a transient GW signal. This signal (Figure 2.13) enters in the detectors near 30 Hz and then sweeps upwards in frequency to 250 Hz with a peak GW strain of 1.0×10^{-21}. It matches the waveform predicted by

---

[2] The BNS range is the averaged distance at which a compact binary coalescence of two $1.4\,M_\odot$ neutron stars gives a matched filter SNR of 8 in a single detector [98].
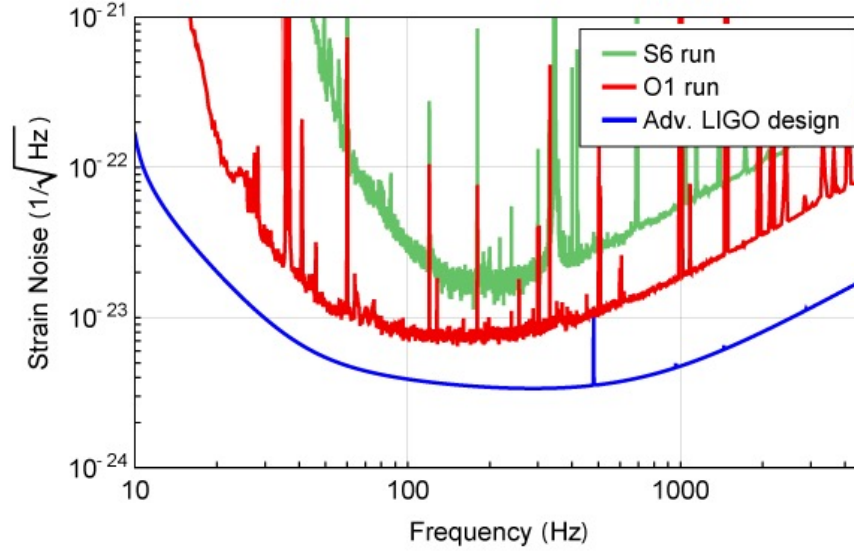
Figure 2.12: Sensitivity curves of initial LIGO during the S6 run and Advanced LIGO in O1 run, as well as the full design sensitivity curves of Advanced LIGO. Figure credit: LSC [14].

Table 2.2: Summary of observation schedule and expected sensitivities of the Advanced LIGO and Advanced Virgo detectors. The future schedules will be dependent on the commissioning progress. The BNS detection numbers assume an SNR greater than 12. Around 2022, LIGO-India is expected to be online. (Data in this table is from [59].)

Epoch		$2015-2016$	$2016-2017$	$2017-2018$	2019+	2022+ (India)
Estimated run duration		4 months	6 months	9 months	(per year)	(per year)
BNS range/Mpc	LIGO	$40-80$	$80-120$	$120-170$	200	200
	Virgo	—	$20-60$	$60-85$	$65-115$	130
Estimated BNS detections		$0.0005-4$	$0.006-20$	$0.04-100$	$0.2-200$	$0.4-400$

General Relativity for the inspiral, merger and ringdown of two black holes with masses of $36^{+5}_{-4}\,M_\odot$ and $29^{+4}_{-4}\,M_\odot$ in the source frame. After $3^{+0.5}_{-0.5}\,M_\odot c^2$ energy released in the form of GWs in this process, the newly formed black hole has a rest-frame mass of $66^{+4}_{-4}\,M_\odot$ and spin $0.67^{+0.05}_{-0.07}$. The luminosity distance of the source is 410^{+160}_{-180} Mpc. With a matched-filter SNR of 24 and a significance greater than 5.1σ, GW150914, as it has been named, is the first confirmed GW observation [58]. As the first direct detection of gravitational waves and the first observation of a binary black hole merger, GW150914 is significant from various perspectives in science. It confirms: (1) the existence of gravitational radiation predicted by Einstein's theory, (2) the validity of Einstein's theory of gravity in the strong gravitational field regime, and (3) the existence of black holes. From an astrophysical perspective, the detection of GW150914 opens a new observation window, and provides the first measure of the mass and the spin of stellar-mass black holes.

GW astronomy began on 14 September, 2015, 4 days before O1. At that time, LIGO was carrying out the eighth engineering run (ER8) which was intended to provide a gradual transition into the continuous operation of an observing run, so the data during this time is as good as the data in O1. In the following four months, the LIGO detectors were continuously listening to the Universe. On 26 December, 2015, a second binary black hole (BBH) merger, GW151226, was observed by LIGO with a significance again greater than 5σ [57]. In addition to this, there was a third candidate BBH event, LVT151012, on 12 October, 2015 with a significance $\approx 2\sigma$n[57]. This significance is not large enough to claim a detection, but it is more likely that LVT151012 results from a GW signal rather than environmental or instrumental transient noise. Various astrophysical implications have been discussed from these unique GW observations[60, 54, 53, 61]. For instance, (1) how does the large stellar-mass BBHs form and merge in less than a Hubble time; (2) what's the mass distribution of BBHs and their merger rate; (3) is there any evidence for deviations from GR; and so on. Detections of these GW events by LIGO open a new era of how we observe the Universe. The meaning and implications of LIGO GW events are broader than what I can cover in this introductory chapter. In the end of this paragraph, I want to show one last Figure 2.14 to close this topic.

The first GW detection is a milestone on path of human beings exploring Nature. As a member of LIGO Scientific Collaboration (LSC), I am so proud of being a part of this. After LIGO announced the first GW event, as one of a few Chinese in LVC, I was invited by many Chinese media to write popular science articles to introduce this event. Chinese people were so interested by the GW that my articles were viewed over one million times [15]. Together with Y. Hu, I also maintain the LSC official Weibo account (Chinese counterpart of twitter) which attracts over 13 thousand followers. The tweet "we detected it!" was viewed over a half million times [16].

2.3 Space-based interferometric detectors

While the ground-based interferometric detectors like Advanced LIGO are making exciting discoveries, the space-based interferometric detectors are under active investigations. Unlike the ground-based interferometers which are fundamentally limited by the seismic noise wall at ~ 10 Hz, the interferometers in space are free of seismic noise and are able to observe a low frequency band of $\sim 10^{-6}$ to ~ 10 Hz. In addition, in the vacuum of space, the interferometer does not need to be encased in
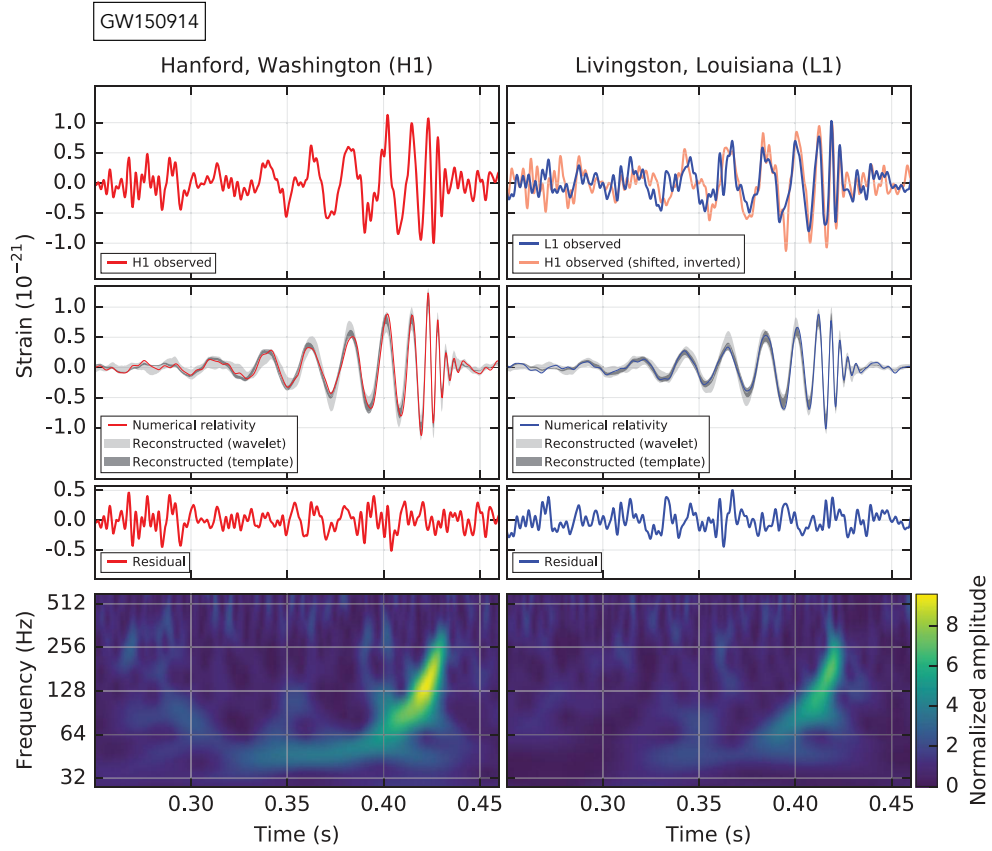
Figure 2.13: The first detected GW signal GW150914 observed by the LIGO H1 (left panel) and L1 (right panel) interferometers. The first row shows the strain with time in the two interferometers. Note that in the right plot H1 strain is time shifted for visual comparison because GW150914 arrived first at L1 and $6.9^{+0.5}_{-0.4}$ ms later at H1. The second row shows the gravitational wave strain projected onto each detector in the 35-350 Hz band, and the solid lines show the numerical relativity waveform of two coalescing black holes of $36^{+5}_{-4}\,M_\odot$ and $29^{+4}_{-4}\,M_\odot$ and forming a new black hole of $62^{+4}_{-4}\,M_\odot$. The third row gives a time-frequency representation of the strain data, showing the signal frequency increasing over time. Figure and caption credit: LSC [58].
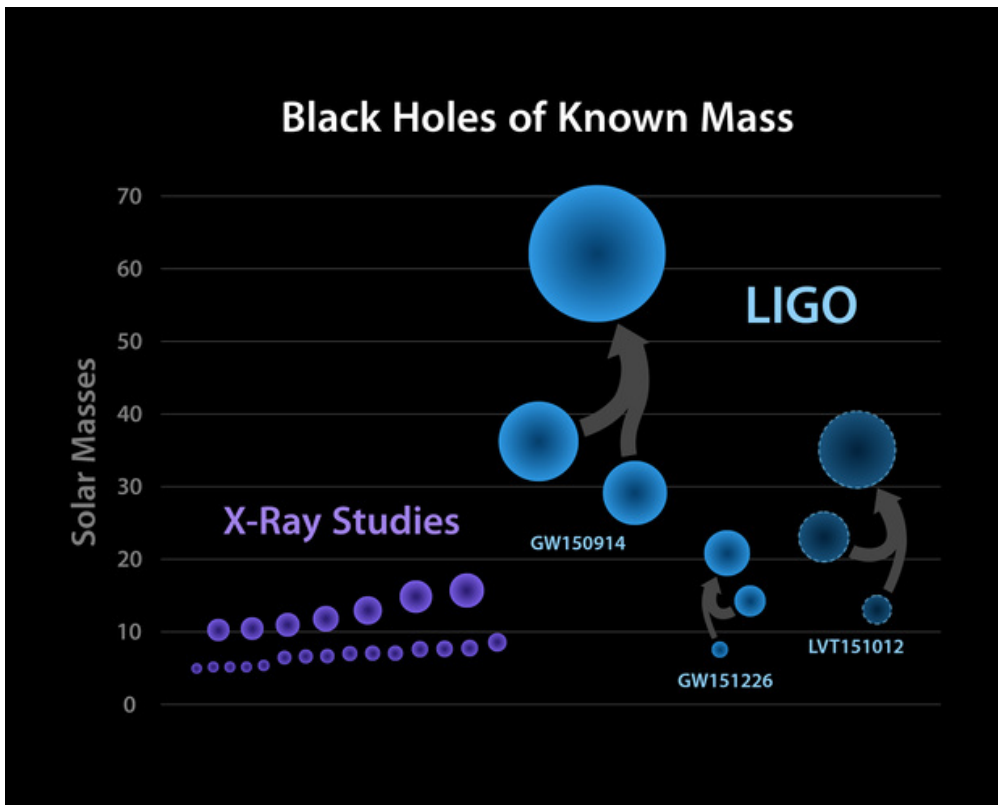
Figure 2.14: black holes of known masses. The discoveries of LIGO expand the known mass range of stellar black holes. These small purple ones are black holes observed via X-Ray channel and the large blue ones are from the GW observation. Figure credit: LSC.

a vacuum tube, so it can be designed with an arm length of a few million km. On the other hand, once the interferometer has been sent into space, the hardware cannot be serviced and tuned on site, so various fascinating techniques are required for space-based interferometers.

Among all the proposed space detectors, the Laser Interferometer Space Antenna (LISA) is the most mature one and will likely be the first detector in space [93]. The concept of LISA is an equilateral triangular array of three spacecrafts, with 2.5 million km arm lengths, orbiting the Sun in the Earth's orbit but trailing the Earth by 20 degrees. Each spacecraft contains two test masses, two lasers and two telescopes which are assembled into two optical sets pointed at the other two spacecrafts. The telescope is used to detect the incoming laser from one spacecraft and then an amplified laser beam with the same phase and frequency is sent back to the original spacecraft. This allows for the exact Doppler tracking of the spacecrafts. Thus, the distance between the spacecrafts is precisely measured to detect a passing gravitational wave in a range from $\sim 10^{-4}$ to ~ 0.1 Hz. In this low-frequency GW window, the primary scientific objective of LISA is to measure gravitational waves produced by supermassive black hole (SMBH) binaries. The LISA mission was first proposed by the United States National Aeronautics and Space Administration (NASA) and the European Space Agency (ESA) together. In 2011, however, NASA paused the LISA partnership because of funding limitations. LISA was then taken over by ESA and a launch could feasibly occur around 2030 [17].

As the first step of ESA's GW observation in space, a small satellite named LISA Pathfinder was launched on December 3, 2015 [18]. LISA Pathfinder is essentially a scaled-down version of two LISA spacecrafts. Instead of millions km arm lengths, LISA Pathfinder contains two test masses 40 cm apart in a nearly perfect free fall condition. The relative motion between the two test masses is controlled and measured with unprecedented accuracy. Several technologies required by LISA are being tested in LISA Pathfinder and they worked so well that the sensitivity of LISA Pathfinder exceeded the expectations. After 127 days of the launch, the acceleration noise of the free fall of the test masses is as small as $(0.54\pm0.01)\times10^{-15}g/\sqrt{\text{Hz}}$, where g the standard gravitational acceleration on the Earth [72]. This sub-femto-g noise in LISA Pathfinder is even better than the requirement of LISA.

In addition to LISA, there are several other concepts for space-based detectors. A Japanese project, Deci-hertz Interferometer Gravitational Wave Observatory (DECIGO), aims to fill the gap in frequency $(0.1 - 10$ Hz) between LISA and ground-based detectors [116, 71] (Figure 2.11). DECIGO would have a similar configuration to LISA, but with a much shorter arm length of 1000 km. Another similar mission, the US Big Bang Observer (BBO) [103], also seeks to cover the same frequency band as DECIGO. Besides observing GW emission from younger sources like binary inspirals, another scientific aim of BBO is to observe GWs from the early Universe (shortly after the Big Bang). With 50000-km arm lengths and more powerful lasers, BBO is designed to be 2-3 times more sensitive than DECIGO [147].

Recently, there have been two proposals in China for space-based GW detectors in LISA's frequency range, the Earth orbiting detector Tianqin with arm lengths of 0.1 million km [127] and the Solar orbiting detector Taiji with arm lengths of 3 million km [100]. These two proposals was initially competed against each other but now collaborate with each other on an unified mission for the future Chinese space-based GW detector.

2.4   Pulsar timing array

Instead of building expensive GW detectors either on the ground or in space, we can utilize the "detectors" that already exist in nature. Pulsar are rapidly spinning neutron stars whose beamed electromagnetic radiation sweeps through the Earth at the pulsar's spin frequency. The rotation frequency of some neutrons stars – more specifically, the millisecond pulsars which are not prone to starquakes and accretion events – is very stable. Therefore, they are very good clocks and are competitive with modern atomic clocks. When GWs pass through an array consisting of a number of millisecond pulsars, they will affect the times of arrival (TOA) of pulsar signals. By observing the correlated changes to the TOAs, one can detect the gravitational waves. The arm length of pulsar timing array (PTA) can be imagined as the distance between the individual pulsar and Earth. Compared to the arm lengths of detectors like LIGO (km-scale) or LISA (million-km-scale), a PTA's arm length is much longer (galaxy-scale) so it has a lower observation frequency range from 10^{-9} to 10^{-6} Hz. At such a low frequency band, the expected astrophysical sources would be super massive black hole binaries in the centres of merging galaxies.

The sensitivity of PTA depends on the number of known pulsars which have low uncertainties (~ 100 ns) in their TOA. Currently, 37 pulsars with TOA uncertainties from ~ 100 ns to ~ 2000 ns are being observed in the International Pulsar Timing Array project [105] which is formed from three collaborations: the Parkes Pulsar Timing Array (PPTA) of Australia [106], the European Pulsar Timing Array (EPTA) of UK, France, Netherlands and Italy [95], and the North American NanoHertz Observatory for Gravitational Waves (NANOGrav) of U.S.A. and Canada [112]. In the coming years, the sensitivity of PTA is expected to be improved as new radio telescopes join. For example, the Chinese Five-hundred-meter Aperture Spherical radio Telescope (FAST) recently started its testing and commissioning [136, 19]. FAST is an ideal radio telescope for pulsar searching and timing and it will improve the uncertainties of TOA and increase the already large number of known pulsars significantly. Furthermore, the Square Kilometre Array (SKA) telescope is scheduled to begin its construction in 2018 and start initial observations by 2020. With a huge collecting area of approximately one square kilometre, SKA will be able to provide timing information for many more pulsars at high precision and bring an enormous increase in PTA sensitivity (Figure 2.11) [122]. Recently, an estimate has been made that the stochastic GW signals from supermassive BBH mergers is likely detected by PTA in next two decades [166].

Chapter 3

Data analysis of GW signals from spinning compact stars

Continuous gravitational waves (CWs) produced by a spinning rigid body are one of the most important and interesting types of GWs. Spinning compact objects (such as neutron stars) with non-axisymmetric distortions are expected to emit CWs which lie in the most sensitive frequency range of ground-based interferometers. In this chapter, I will describe GW signals from isolated neutron stars, as well as the analysis methods to detect them.

3.1 Detector response to gravitational waves

3.1.1 Antenna pattern functions

Before going into the details of the detector response to GWs, I will first introduce the reference frames. Figure 3.1 shows two frames. The first one, denoted by (x_d, y_d, z_d), is the reference frame of the detector. The x_d and y_d directions are parallel to the two detectors' arms. The second one, (x_w, y_w, z_w), is the gravitational wave frame. The gravitational wave travels in the z_w direction and the neutron star's rotation axis is perpendicular to the x_w direction.

Assume that the arm length of the detector is much shorter than the reduced wavelength $\lambda/(2\pi)$ of the gravitational wave (long wavelength approximation). The dimensionless detector response $h(t)$ to GWs is defined as the relative length changes of the two arms of the interferometer and can be written as

$$h(t) = \frac{1}{2}\mathbf{n}_1 \cdot \left[\widetilde{H}(t)\mathbf{n}_1\right] - \frac{1}{2}\mathbf{n}_2 \cdot \left[\widetilde{H}(t)\mathbf{n}_2\right], \qquad (3.1)$$

where $\mathbf{n}_1$ and $\mathbf{n}_2$ are the unit vectors in the two arms' directions and $\widetilde{H}$ is the three-dimensional matrix of the spatial metric perturbation induced by the gravitational wave in the detector's proper reference frame. The matrix $\widetilde{H}$ can be written as

$$\widetilde{H}(t) = M(t)H(t)M(t)^T, \qquad (3.2)$$
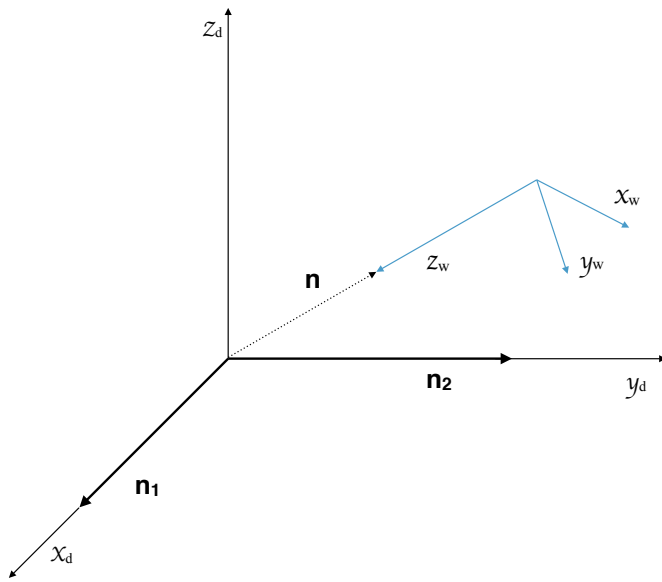
Figure 3.1: Illustration of the detector and gravitational wave reference frames: The detector frame (x_d, y_d, z_d), where $\mathbf{n}_1$ and $\mathbf{n}_2$ are the unit vectors in the two arms' directions and $\mathbf{n}$ represents the relative position of the source; the reference frame of the wave, (x_w, y_w, z_w), has z_w in direction of the gravitational wave's propagation and the x_w direction is perpendicular to the neutron star's rotation axis.

where M is the three-dimensional orthogonal matrix and represents the transformation from the co-ordinates (x_w, y_w, z_w) of the gravitational wave to the coordinates (x_d, y_d, z_d) in the proper reference frame of detector (Figure 3.1). T indicates matrix transposition. If the gravitational wave travels in the z_w direction, the matrix H has the form:

$$H(t) = \begin{pmatrix} h_+(t) & h_\times(t) & 0 \\ h_\times(t) & -h_+(t) & 0 \\ 0 & 0 & 0 \end{pmatrix}, \tag{3.3}$$

where the functions $h_+(t)$ and $h_\times(t)$ are two gravitational wave polarizations. Combining Equations (3.1)–(3.3), we have the response function $h(t)$ which is a linear combination of $h_+(t)$ and $h_\times(t)$:

$$h(t) = F_+(t)h_+(t) + F_\times(t)h_\times(t), \tag{3.4}$$

where $F_+(t)$ and $F_\times(t)$ are called the *antenna pattern functions*. $F_+(t)$ and $F_\times(t)$ depend on (1) the detector's position (latitude of the detector's site λ), orientation (γ), and angle between the two arms (ζ), (2) the sky position of the source (defined by the right ascension α and declination δ), and (3) the polarization angle ψ (the angle between the x_w direction and the direction defined by the intersection of the gravitational wave plane (x_w, y_w) with the Earth's equatorial plane). The detector rotates with the Earth and so periodically changes its orientation with respect to the source. Therefore, $F_+(t)$ and $F_\times(t)$ are periodic time functions with a period of one sidereal day. Skipping the extensive algebraic manipulations, the explicit form of F_+ and $F_\times$ is [111]:

$$F_+(t) = \sin\zeta \left[a(t)\cos 2\psi + b(t)\sin 2\psi \right], \tag{3.5}$$
$$F_\times(t) = \sin\zeta \left[b(t)\cos 2\psi - a(t)\sin 2\psi \right], \tag{3.6}$$

where

$$\begin{aligned}
a(t) = {} & \frac{1}{16}\sin 2\gamma(3 - \cos 2\lambda)(3 - \cos 2\delta)\cos[2(\alpha - \phi_r - \Omega_r t)] \\
& - \frac{1}{4}\cos 2\gamma \sin\lambda(3 - \cos 2\delta)\sin[2(\alpha - \phi_r - \Omega_r t)] \\
& + \frac{1}{4}\sin 2\gamma \sin 2\lambda \sin 2\delta \cos[\alpha - \phi_r - \Omega_r t] \\
& - \frac{1}{2}\cos 2\gamma \cos\lambda \sin 2\delta \sin[\alpha - \phi_r - \Omega_r t] \\
& + \frac{3}{4}\sin 2\gamma \cos^2\lambda \cos^2\delta, \tag{3.7} \\
b(t) = {} & \cos 2\gamma \sin\lambda \sin\delta \cos[2(\alpha - \phi_r - \Omega_r t)] \\
& + \frac{1}{4}\sin 2\gamma(3 - \cos 2\lambda)\sin\delta \sin[2(\alpha - \phi_r - \Omega_r t)] \\
& + \cos 2\gamma \cos\lambda \cos\delta \cos[\alpha - \phi_r - \Omega_r t] \\
& + \frac{1}{2}\sin 2\gamma \sin 2\lambda \cos\delta \sin[\alpha - \phi_r - \Omega_r t]. \tag{3.8}
\end{aligned}$$

Ω_r is the spin velocity of the Earth, and ϕ_r is the initial phase and represents the position of the Earth in its diurnal motion at $t = 0$. The sum $\phi_r + \Omega_r t$ denotes the local sidereal time of the detector (the angle between the local meridian and the vernal point). γ is measured counter-clockwise from the East to the angular bisector of the detector's arms.

3.1.2   The expected GW from spinning NS

To obtain the full expression of detector response $h(t)$ (Equation 3.4), the functions $h_+(t)$ and $h_\times(t)$ are needed.

Rapidly rotating neutron stars must be asymmetric in order to radiate gravitational waves. Here I consider the simplest model that a NS rotating around a principal axis which is a special case of a freely precessing NS with the wobble equal to $\pi/2$ [178]. Neglecting the proper motion of the star, the GW signal in solar system barycenter (SSB) frame can be expressed as [111]:

$$h_+(t) = \frac{1}{2}h_0(1 + \cos^2 \iota) \cos 2\Psi_{\mathrm{SSB}}(t_{\mathrm{SSB}}),$$
$$h_\times(t) = h_0 \cos \iota \sin 2\Psi_{\mathrm{SSB}}(t_{\mathrm{SSB}}). \tag{3.9}$$

ι is the angle between the rotation axis and the direction from the NS to Earth. t_{SSB} is the arrival time of the GW front at the SSB. $\Psi(t)$ is the phase of the gravitational wave signal in the SSB frame which has the form [111]:

$$\Psi_{\mathrm{SSB}}(t_{\mathrm{SSB}}) = \Phi_0 + 2\pi \sum_{k=0}^{s} \overset{(k)}{f_0} \frac{t_{\mathrm{SSB}}^{k+1}}{(k+1)!}, \tag{3.10}$$

where Φ_0 is the initial GW phase evaluated at $t_{\mathrm{SSB}} = 0$ in the SSB frame and $\overset{(k)}{f_0}$ is the kth time derivative of the instantaneous NS spin frequency evaluated at $t_{\mathrm{SSB}} = 0$ in the SSB frame. From Equations (3.9) and (3.10), we see that the frequency of gravitational waves emitted by a spinning NS is twice the spin frequency. Equation (3.10) says that the gravitational wave signal in the SSB frame is almost a monochromatic sinusoid due to the loss of rotational energy. One of the reasons of this loss is the emission of GWs.

Due to the orbital motion and rotation of the Earth, the gravitational wave signal at the detector is Doppler shifted. The phase of the gravitational wave at the detector has the form [111]:

$$\Psi(t) = \Phi_0 + \Phi(t) \quad \text{where} \quad \Phi(t) = +2\pi \sum_{k=0}^{s} \overset{(k)}{f_0} \frac{t^{k+1}}{(k+1)!} + \frac{2\pi}{c} \mathbf{n}_0 \cdot \mathbf{r}_{\mathrm{d}}(t) \sum_{k=0}^{s} \overset{(k)}{f_0} \frac{t^k}{k!}. \tag{3.11}$$

Equation (3.11) gives the phase as function of the time at the detector. t is the arrival time of the GW front at the detector $\mathbf{n}_0$ is the unit vector in the direction of the star in the SSB frame. $\mathbf{r}_{\mathrm{d}}$ is the position vector of the detector in that frame.

In Equations (3.9), h_0 is the gravitational wave amplitude. A straightforward application of the Einstein quadrupole formula yields:

$$h_0 = \frac{4\pi^2 G}{c^4} \frac{I_{zz} f^2 \varepsilon}{D}, \tag{3.12}$$

where, f is the instantaneous frequency of the emitted GW signal (twice the rotational frequency), G Newton's constant, and D the distance from the Earth to the NS. I_{zz} is the moment of inertia with respect to the rotation axis (also one principal axis) so that I_{xx} and I_{yy} are the moments of inertia with respect to other two principal axes. Among all the quantities appearing in Equation (3.12), the value of ε is by far the most uncertain. ε is called the ellipticity and describes the degree of distortion of the star. It can be defined as:

$$\varepsilon = \frac{|I_{xx} - I_{yy}|}{I_{zz}}. \tag{3.13}$$

The ellipticity of a NS is expected to be supported by the NS's strong magnetic fields or its crust, and the distribution of ε is highly uncertain. Estimates on the maximum strain which a NS crust can sustain before breaking vary according to various models of NS internal structure. However, these estimates only give upper limits on the allowed ellipticities rather than estimates of the actual values. Over recent years, these estimations for the maximum ellipticity have changed significantly. The most current prediction is $\varepsilon_{\max} \sim 10^{-5}$ for the standard nucleon-only NS model [114]. Other predictions for maximum ellipticity are $\sim 10^{-4}$ given by [107] and $\sim 10^{-6}$ given by [168]. Aside from approach via NS modeling to predict the upper limit of ε, there are other two approaches.

The first is called the spin-down upper limit for the ellipticity $\varepsilon^{\mathrm{sd}}$. Typically, neutron stars spin down and thus lose their rotational kinetic energy. Most of this energy loss can be attributed to electromagnetic interactions. For example [164], the neutron star can be described as a rotating body with a magnetic dipole moment $\mathbf{m}$ that is misaligned with the rotation axis. This system would lose energy at a rate proportional to $|\ddot{\mathbf{m}}|^2$. In contrast, if the loss of rotational kinetic energy of the star is assumed to be entirely due to the gravitational radiation, an upper limit on h_0 is thus set. This upper limit is known as the spindown limit h_0^{sd} and it can be translated to an upper limit on the the ellipticity. I illustrate this in the next paragraph.

GWs carry energy away at a rate $\dot{E}_{\mathrm{gw}}$ given by

$$\langle \dot{E}_{\mathrm{gw}} \rangle = -\frac{c^3}{16\pi G} \oint_S \langle \dot{h}_+^2 + \dot{h}_\times^2 \rangle dS, \tag{3.14}$$

where S is a large sphere with radius D centered at the star, and dS the area element on the large sphere. The brackets $\langle \cdot \rangle$ decribes a time average over a adequately large number of CW cycles. Using the CW waveform given in Equation (3.9), $\dot{E}_{\mathrm{gw}}$ can be calculated to be $\langle \dot{E}_{\mathrm{gw}} \rangle \propto f^2 h_0^2 D^2$. Since $\dot{E}_{\mathrm{gw}}$ is independent of D, h_0 is proportional to $1/D$. At the same time, the rotational kinetic energy of the star is $E_{\mathrm{rot}} = I\pi^2 f^2/2$, so that $\dot{E}_{\mathrm{rot}} = \pi I f \dot{f}$. Letting $\langle \dot{E}_{\mathrm{gw}} \rangle = \dot{E}_{\mathrm{rot}}$ and averaging over the sphere S, the gravitational wave amplitude h_0^{sd} can be obtained:

$$h_0^{\mathrm{sd}} = \frac{1}{D} \sqrt{\frac{5GI}{2c^3} \frac{|\dot{f}|}{f}} \quad \text{and} \quad h_0 \le h_0^{\mathrm{sd}}. \tag{3.15}$$

The value of h_0^{sd} is determined by energy conservation, and doesn't depend on the actual mechanism that causes the neutron star to emit gravitational radiation. Therefore, this is an upper limit on h_0 and the actual amplitude of the CW from an isolated NS is expected to be much smaller and depends on

the emission mechanism. One can assume that no more than a fraction x of the spindown energy is taken away by gravitational radiation. Thus the corresponding upper limit is smaller by a factor $\sqrt{x}$:

$$h_0 \leq \frac{1}{D}\sqrt{x \cdot \frac{5GI}{2c^3}\frac{|\dot{f}|}{f}} \; . \tag{3.16}$$

Based on the most recent observational limits on GW emission from the Vela and Crab pulsars, x is constrained to less than 1% and 0.2% respectively for these two pulsars [62]. By combining Equations (3.15) and (3.12), I can get the value of ε required for emitting at the spindown limit:

$$\varepsilon^{\mathrm{sd}} = \sqrt{\frac{5c^5}{32\pi^4 G}\frac{|\dot{f}|}{I f^5}} \tag{3.17}$$

and correspondingly for emitting CWs at a fraction x of the spindown energy:

$$\varepsilon_x^{\mathrm{sd}} = \sqrt{\frac{5c^5}{32\pi^4 G}\frac{x|\dot{f}|}{I f^5}} \; . \tag{3.18}$$

The upper limit on ellipticity from the final approach is known in the literature as the age limit. If I assume that the NS's frequency evolution follows $\dot{f} \propto f^n$, where n is the braking index, and the NS has been spinning down from f at a spindown rate $\dot{f}$ during a time τ_{c}, which is called its characteristic age[1], then I have:

$$\tau_{\mathrm{c}} = \frac{1}{n-1}\frac{f}{|\dot{f}|} \; . \tag{3.19}$$

Here, the braking index n represents the mechanism that causes the neutron star to emit gravitational radiation. For pure GW emission, $n = 5$, and for pure electromagnetic, $n = 3$ (see e.g. [164]). The age of the NS can be estimated, for instance, using electromagnetic observations of the surrounding supernova remnant if one exists. If I take this estimated age of the NS as a proxy for its characteristic age τ_{c} and combine Equation (4.19) with Equations (3.15) and (3.17), I have the corresponding upper limit on GW amplitude and ellipticity in terms of τ_{c}:

$$h_0^{\mathrm{sd}} = \frac{1}{D}\sqrt{\frac{5GI}{2(n-1)c^3\tau_{\mathrm{c}}}} \tag{3.20}$$

and

$$\varepsilon^{\mathrm{age}} = \frac{c^2}{4\pi^2 f^2}\sqrt{\frac{5c}{2(n-1)GI\tau_{\mathrm{c}}}} \; . \tag{3.21}$$

---

[1]It should be note that for normal pulsars, with a period ~ 0.1 second, their characteristic ages can be very approximate to their true age. For example, in 2007 the Crab pulsar had a period of 0.0331 second and a spin-down of 4.22×10^{-13} Hz/s, correspond to a characteristic age around 1240 years. The supernova that produced the pulsar was in 1054 AD, yielding an age of around 950 years [113].

If $n = 5$ then $\tau_c = f/4|\dot{f}|$ is the shortest lifetime compared to the characteristic ages of other emission mechanisms. Here I want to point out that the choices on the upper limit on ellipticity as well as its distribution play an important role in the optimisation procedures described in Sections 4, 5 and 6.

Now I have the complete expression of Equation (3.4) and can rewrite it in the following form [111]:

$$h(t) = \sum_{i=1}^{4} A_i \, h_i(t), \tag{3.22}$$

where the four amplitudes A_i depend on the unknown $h_0, \theta, \iota, \psi, \Phi_0$ and on the known ζ:

$$A_1 = h_0 \sin \zeta \sin^2 \theta \left[\frac{1}{2}(1 + \cos^2 \iota) \cos 2\psi \cos 2\Phi_0 - \cos \iota \sin 2\psi \sin 2\Phi_0 \right], \tag{3.23}$$

$$A_2 = h_0 \sin \zeta \sin^2 \theta \left[\frac{1}{2}(1 + \cos^2 \iota) \sin 2\psi \cos 2\Phi_0 + \cos \iota \cos 2\psi \sin 2\Phi_0 \right], \tag{3.24}$$

$$A_3 = h_0 \sin \zeta \sin^2 \theta \left[-\frac{1}{2}(1 + \cos^2 \iota) \cos 2\psi \sin 2\Phi_0 - \cos \iota \sin 2\psi \cos 2\Phi_0 \right], \tag{3.25}$$

$$A_4 = h_0 \sin \zeta \sin^2 \theta \left[-\frac{1}{2}(1 + \cos^2 \iota) \sin 2\psi \sin 2\Phi_0 + \cos \iota \cos 2\psi \cos 2\Phi_0 \right]. \tag{3.26}$$

The four detector-dependent wave components h_i depend on $(\alpha, \delta, f_0, \overset{(k)}{f_0}; \lambda, \gamma, t)$:

$$\begin{aligned} h_1 &= a(t) \cos 2\Phi(t), & h_2 &= b(t) \cos 2\Phi(t), \\ h_3 &= a(t) \sin 2\Phi(t), & h_4 &= b(t) \sin 2\Phi(t). \end{aligned} \tag{3.27}$$

Here, the functions a and b are given by Equations (3.7) and (3.8), and Φ is the GW phase given by Equation (3.11). Recall that a and b depend on the right ascension α, the declination δ of the source, and the angles λ, γ. The phase Φ depends on the frequency f_0, s spindown parameters $\overset{(k)}{f_0}$ ($k = 1, \ldots, s$), and the angles α, δ. Among these, $f_0, \overset{(k)}{f_0}, \alpha, \delta$ are the phase parameters which are unknown and λ is the latitudeof the detector, which is known. Thus, the complete signal h depends on $8 + s$ unknown parameters: $h_o, \theta, \psi, \iota, \Phi_0, \alpha, \delta, f_0, \overset{(k)}{f_0}$.

3.2 Detection statistic for CW signals

The major challenge in CW data analysis is that the very weak signal is buried in detector noise. Extracting the weak signal out of strong noise is a common problem in many scientific fields, and over years many approaches have been developed to overcome this problem. One standard method is called the *maximum likelihood detection* method. It was first introduced into CW data analysis by Jaranowski, Krolak and Schutz in 1998 (JKS98) [111] and afterwards was extensively applied to various CW searches. In this section, I briefly introduce this method and its results.

The basic idea behind the signal detection can be posed as a binary hypothesis testing problem:

$$\mathcal{H}_0 : x(t) = n(t), \qquad \text{no signal is present}, \tag{3.28}$$

$$\mathcal{H}_1 : x(t) = n(t) + s(t), \qquad \text{the signal } s(t) \text{ is present}. \tag{3.29}$$

Here $s(t)$ is the GW signal, $n(t)$ the detector noise, and $x(t)$ the detector data which is measured over an interval of $t : [0, T_{\text{obs}}]$. When the signal is absent the data have a probability density function (PDF) $p_0(x)$, and when the signal is present the data have a PDF $p_1(x)$. In order to make the decision between the two hypotheses, a detection statistic Λ needs to be built. $\Lambda(x(t))$ is a function of the detector's data $x(t)$. If Λ is larger than a given threshold Λ_{thr}, I say $\mathcal{H}_1$ is true, and if $\Lambda \leq \Lambda_{\text{thr}}$, I choose $\mathcal{H}_0$. The probability of detecting $\mathcal{H}_1$ when $\mathcal{H}_0$ is called *the false alarm probility* and can be defined as

$$P_{\text{FA}} = P(\Lambda(x(t)) > \Lambda_{\text{thr}} | \mathcal{H}_0). \tag{3.30}$$

The detection probability is defined as

$$P_{\text{D}} = P(\Lambda(x(t)) > \Lambda_{\text{thr}} | \mathcal{H}_1). \tag{3.31}$$

The Neyman-Pearson Lemma [137] states that a statistic $\Lambda(x)$ is optimal if $\Lambda(x)$ has the highest P_{D} at a given P_{FA} and that optimal statistic is any monotonic function of likelihood ratio test:

$$\Lambda(x) = \frac{p_1(x)}{p_0(x)}. \tag{3.32}$$

If we assume the noise of the detector is a Gaussian, stationary, and zero-mean continuous random process, an expression for the log likelihood function can be obtained (see detailed derivation in section 3.4 of book [110]):

$$\ln \Lambda = (x|s) - \frac{1}{2}(s|s), \tag{3.33}$$

where the scalar product $(\,\cdot\,|\,\cdot\,)$ can be approximately expressed as:

$$(x|s) \cong \frac{2}{S_h(f)} \int_0^{T_{\text{obs}}} x(t)s(t)\, dt, \tag{3.34}$$

where $S_h(f)$ is the one-sided spectral density of detector noise. Equation (3.33) is maximum when $x \equiv s$. One usually refers to "s" as the template.

The signal s linearly consists of four correlated GW amplitudes A_i (Equation (3.22)) that depend on five unknown parameters $(h_0, \theta, \iota, \psi, \Phi_0)$. One can find the maximum likelihood estimators for these five unknown parameters to maximize the likelihood function given in Equation (3.33). These five parameters are intractable in a set of nonlinear equations, so the maximum likelihood estimators can be solved numerically using computationally expensive methods. Instead, as a compromise, these four linear-combined amplitudes A_i are treated independently and the maximum likelihood estimators for A_i are used to construct a so called reduced likelihood function, greatly reducing the computational cost. If these A_i are independent, in order to get their maximum likelihood estimators, one can let:

$$\frac{\partial \ln \Lambda}{\partial A_i} = 0, \quad i = 1, \dots, 4. \tag{3.35}$$

The solutions to the above set of equations are:

$$\sum_{j=1}^{4} \mathcal{M}_{ij} A_j = (x|h_i), \quad i = 1, \ldots, 4, \tag{3.36}$$

where the 4×4 matrix $\mathcal{M}_{ij}$ has the form:

$$\mathcal{M}_{ij} = (h_i|h_j). \tag{3.37}$$

Over a relatively long observation time T_{obs} which contains many cycles of Φ, some components of $\mathcal{M}_{ij}$ average to zero [111]:

$$(h_1|h_3) = 0, \quad (h_1|h_4) = 0, \quad (h_2|h_3) = 0, \quad (h_2|h_4) = 0. \tag{3.38}$$

The rest of the non-zero components are denoted by A, B, and C:

$$\begin{aligned}
(h_1|h_1) &= (h_3|h_3) &= \tfrac{1}{2}A, \\
(h_2|h_2) &= (h_4|h_4) &= \tfrac{1}{2}B, \\
(h_1|h_2) &= (h_3|h_4) &= \tfrac{1}{2}C.
\end{aligned} \tag{3.39}$$

Thus, the new expressions of A_i without the five unknown parameters are obtained [111]:

$$\begin{aligned}
\widehat{A}_1 &= 2\frac{B(x|h_1) - C(x|h_2)}{D}, \\
\widehat{A}_2 &= 2\frac{A(x|h_2) - C(x|h_1)}{D}, \\
\widehat{A}_3 &= 2\frac{B(x|h_3) - C(x|h_4)}{D}, \\
\widehat{A}_4 &= 2\frac{A(x|h_4) - C(x|h_3)}{D},
\end{aligned} \tag{3.40}$$

where D is defined by

$$D = AB - C^2. \tag{3.41}$$

According to the Schwarz inequality, $D > 0$ $(A \neq B)$. The second partial derivatives of $\ln \Lambda$ are:

$$\frac{\partial^2 \ln \Lambda}{\partial A_i \partial A_j} = -\mathcal{M}_{ij}. \tag{3.42}$$

Since $A > 0$ and $B > 0$, the extrema of $\ln \Lambda$ is local maxima. Therefore, after replacing A_i by the maximum likelihood estimators $\widehat{A}_i$ in the reduced likelihood function $\ln \Lambda$, the maximum log likelihood function is obtained:

$$\begin{aligned}
\mathcal{F} = \ &\frac{B(x|h_1)^2 + A(x|h_2)^2 - 2C(x|h_1)(x|h_2)}{D} \\
&+ \frac{B(x|h_3)^2 + A(x|h_1)^2 - 2C(x|h_3)(x|h_4)}{D}.
\end{aligned} \tag{3.43}$$

$\mathcal{F}$ is called the $\mathcal{F}$-statistic, and because of its statistical properties one commonly works with $2\mathcal{F}$:

$$2\mathcal{F} = \frac{2B(x|h_1)^2 + 2A(x|h_2)^2 - 4C(x|h_1)(x|h_2)}{D}$$
$$+ \frac{2B(x|h_3)^2 + 2A(x|h_1)^2 - 4C(x|h_3)(x|h_4)}{D}, \tag{3.44}$$

which can also be written in the concise form of a tensor:

$$2\mathcal{F} = H_a(\mathcal{M}^{-1})^{ab} H_b \qquad \text{where } H_a = (x|h_a). \tag{3.45}$$

Thanks to this analytical maximization, the $2\mathcal{F}$ statistic depends on the template frequency, the spin-down parameters and source position rather than the five unknown parameters $(h_0, \theta, \iota, \psi, \Phi_0)$. The likelihood function is only maximized if the input frequency, spindowns, α and δ are "matched" with the signal. Therefore, this is often referred to as "matched filtering".

In the special case when the target's frequency, spin-downs, and sky position are known (e.g. searching for CW from the Crab pulsar), the computing cost of this so-called targeted search is inexpensive. However, in the search for CWs from unknown NSs whose position or phase parameters are partly or fully unknown, one must explicitly search over all position and phase parameters. Over long observation periods, this search becomes soon very computationally expensive.

In principle, when the value of the $2\mathcal{F}$ statistic is larger than a certain threshold $2\mathcal{F}^\star$ which is determined by the false alarm probability that one can afford, one can say that a detection of a CW signal has been made. The probability of detection is consequently determined by the magnitude of the $2\mathcal{F}$ statistic's distribution above $2\mathcal{F}^\star$. To find the distribution of $2\mathcal{F}$, let's assume that the detector noise is Gaussian and that the data also contains a signal s. The expectation values E can be obtained as follows:

$$E(n_a) = 0, \qquad E(n_a n_b) = 0,$$
$$E(x_a) = s_a, \qquad E(x_a x_b) = \mathcal{M}_{ab} + s_a s_b, \tag{3.46}$$

where

$$n_a = (n|h_a), \quad s_a = (s|h_a) \quad \text{and} \quad x_a = (x|h_a). \tag{3.47}$$

Combining Equation (3.46) with Equation (3.45), the expectation value of the $2\mathcal{F}$ statistic can be obtained:

$$\begin{aligned}
E[2\mathcal{F}] &= E[H_a(\mathcal{M}^{-1})^{ab} H_b] = (\mathcal{M}^{-1})^{ab} E[H_a H_b] \\
&= (\mathcal{M}^{-1})^{ab} E[(x|h_a)(x|h_b)] \\
&= (\mathcal{M}^{-1})^{ab} (E[(n|h_a)(n|h_b)] + E[(s|h_a)(s|h_b)]) \\
&= (\mathcal{M}^{-1})^{ab} (\mathcal{M}_{ab} + s_a s_b) \\
&= 4 + \rho^2.
\end{aligned} \tag{3.48}$$

When the signal is absent, the term $\rho^2 = 0$, and when the signal is present, the signal-to-noise ratio (SNR) ρ is defined by:

$$\rho^2 = s_a(\mathcal{M}^{-1})^{ab}s_b. \tag{3.49}$$

The $2\mathcal{F}$ statistic is a quadratic function of the four Gaussian noise components n_a. If no signal is present, the $2\mathcal{F}$ distribution follows a central χ^2 distribution with 4 degrees of freedom, and if the signal is present it follows a noncentral χ^2 distribution with 4 degrees of freedom and a noncentrality parameter of ρ^2. Thus, the $2\mathcal{F}$ PDF $p_0(x)$ for the signal-absent case and $p_1(x)$ for the signal-present case will be:

$$p_0(x) = \frac{x}{4}\exp\left(\frac{-x}{2}\right) \tag{3.50}$$

$$p_1(\rho, x) = \frac{\sqrt{x}}{2\rho}I_1(\rho\sqrt{x})\exp\left(\frac{-x - \rho^2}{2}\right), \tag{3.51}$$

where I_1 is the modified Bessel function of the first kind and order 1. When the signal is absent, given a certain threshold $2\mathcal{F}^\star$, we can calculate the false alarm probability:

$$P_{\mathrm{FA}}(2\mathcal{F}^\star) = \int_{2\mathcal{F}^\star}^{\infty} p_0(x)\,dx. \tag{3.52}$$

The detection criterion is set based on a false-alarm threshold P_{FA}, and from Equation (3.52), one can obtain the corresponding threshold $2\mathcal{F}^\star$. The probability P_{D} of detecting a signal is the probability of obtaining a value of the detection statistic $\widehat{2\mathcal{F}}$ higher than the detection threshold $2\mathcal{F}^\star$ when the SNR of ρ^2 is drawn from the distribution:

$$P_{\mathrm{D}}(2\mathcal{F}^\star|\rho^2) := \int_{2\mathcal{F}^\star}^{\infty} p_1(x|\rho^2)\,dx. \tag{3.53}$$

Here, it should be emphasized that, even though the amplitude parameters have been eliminated from the template used to compute the detection statistic $2\mathcal{F}$, the $2\mathcal{F}$ distribution still depends on them through the non-centrality parameter ρ^2.

Consider the multi-detector case, say N_{det} GW detectors labeled by an integer $i = 1 \ldots N_{\mathrm{det}}$. The CW signal's SNR from the ith detector is denoted by ρ_i. By optimally combining the data streams of each detector, one can get a multi-detector $2\mathcal{F}$-statistic which follows a noncentral χ^2 distribution with 4 degrees of freedom and a noncentrality parameter ρ^2 that is the sum of ρ_i^2 from each detector [90]:

$$\rho^2 = \sum_{i=1}^{N_{\mathrm{det}}} \rho_i^2. \tag{3.54}$$

By combining Equations (3.4), (3.9) and (3.49), the explicit dependence of ρ_i^2 on the amplitude parameters of the signal can be derived:

$$\rho_i^2 = \frac{2h_0^2 T_{\mathrm{obs}}}{S_h^{(i)}(f)}\left[\frac{(1 + \cos^2\iota)^2}{4}\langle(F_+^{(i)})^2\rangle_t + \cos^2\iota\langle(F_\times^{(i)})^2\rangle_t\right], \tag{3.55}$$

where the angle brackets $\langle \cdot \rangle_t$ represent an average over time. Equation (3.55) shows that the squared SNR is proportional to T_{obs}. Hence, extending the observation time is an effective way to increase the SNR. On the other hand, for N_{det} detectors with the same sensitivity, the observation time T_{obs} required to obtain a certain SNR for a source by just one detector would scale down by a factor of N_{det}. Therefore, combining data from different detectors is a very useful strategy to increase the probability of detection. For example, the search for CWs from 3 point targets (Chapter 5) and the search for CWs from Galactic Centre (Chapter 6) both use the data from the two LIGO detectors: H1 and L1.

For the practical computation of $2\mathcal{F}$, the original time domain data $x(t)$ is short time-baseline Fourier transformed (SFT) into frequency domain data and these SFT files are narrow-banded. Then these SFTs are weighted by the noise over time to account for the non-stationarity in noise.

3.3   Templates

When the signal parameters are not known, one needs to numerically search over the whole parameter space. In this case, many different templates are compared against the data. Each template corresponds to a different GW waveform. If there is a gravitational wave signal present in the data, the template with the best matching parameters (frequency, spindowns, α and β) in the template bank would result in the highest $2\mathcal{F}$. Because $2\mathcal{F}$ needs to be calculated for each template, the computing cost of a search depends on the total number of templates used in that search. In a blind search with a fixed parameter space, the number of templates is determined by the density of the template bank. A higher density generally leads to a smaller loss in SNR due to signal-template mismatch. However, more templates also means higher computing cost. The density of a template bank can be quantified by the relative loss of squared SNR between the perfect match case (signal parameters λ_{pm}) and template mismatched case (template parameters λ_{mis}):

$$m(\lambda_{\mathrm{pm}}; \lambda_{\mathrm{mis}}) = \frac{\rho^2(\lambda_{\mathrm{pm}}) - \rho^2(\lambda_{\mathrm{mis}})}{\rho^2(\lambda_{\mathrm{pm}})}. \qquad (3.56)$$

Locally around the signal parameters λ_{pm}, one can do a Taylor expansion in a small offset $d\lambda$:

$$m(\lambda_{\mathrm{pm}}; \lambda_{\mathrm{pm}} + d\lambda) \approx g_{ij}(\lambda_{\mathrm{pm}})d\lambda^i d\lambda^j + \mathcal{O}(d\lambda^3). \qquad (3.57)$$

This metric g_{ij} forms the basic transform relation between the template grid spacing and the mismatch at every dimension in parameter space. Thus it is also called the parameter-space metric. The concept of the parameter-space metric was first introduced in the context of searching for binary inspiral signals [76, 138] and afterwards was translated to and developed in the CW field [84, 151, 149]. Recently, a global, numerically well-conditioned CW metric used in semi-coherent searches for isolated NSs has been developed [175, 173, 174]. Signal template banks can be optimized in order to gain maximum sensitivity constrained by a certain computational resource. Some works about this technique have been done (see [132, 173, 146]), but I am not going in to any details. Instead, in the next section, I introduce another technique, which is extensively used in CW searches to increase the sensitivity within a constrained computational resource.

3.4 Semi-coherent search methods

If the computational resources are unlimited, a fully coherent search will provide the best sensitiv-
ity and thus maximize the detection probability of a CW signal. However, with today's computers,
it is impossible to perform a purely coherent search in a data set spanning over several months or
years. Consider a so-called directed search, which is less expensive compared to a blind all-sky search
because the sky position of the source is known. Thus, the parameters that need to be searched are
frequency and spindowns. Consider a fully coherent directed search with a parameter space consisting
of three dimensions: f, $\dot{f}$ and $\ddot{f}$. Because a finer template grid is required by the longer observation
time T_{obs} [2], the number of templates required to cover the parameter space grows with T_{obs}^6 and soon
becomes unmanageable. For this reason, fully coherent wide parameter space searches have been
forced to restrict the duration of the analyzed data (e.g. [46, 41]) which consequentially leads to
limited detection probabilities. To obtain a higher detection probability, semi-coherent searches have
been proposed.

The general idea of semi-coherent algorithms is to break up the full data set into several shorter
time segments, coherently search each segment and combine the results of these coherent analyses to
generate the final detection statistic for the whole data set. Thus, the total computing requirement is
much reduced, and given the same computing resources the semi-coherent search can result in a higher
SNR than a fully coherent search with shorter T_{obs}. The combination of these coherent analyses
doesn't maintain the phase coherence between these segments and for this reason this technique is
called the semi-coherent method. More details on semi-coherent technique can be found in [161, 83,
124, 148, 150]. Here I will just address the notions of computational cost and the sensitivity of such
methods.

For semi-coherent methods, the final resolution in the signal parameter space is obtained in two
steps: the coherent analyses of the individual segments and the incoherent combination of the results
from the coherent analyses. In both of these stages, template banks are required to be set up. The
template bank used in the coherent analysis of the segments is called the *coarse* grid and comprises
N_{c} points. For directed searches the sky position is fixed so the coarse grid consists of points in
$(f, \dot{f}, \ddot{f})$. The incoherent step requires a different template grid, the so-called *fine* grid. It is defined
by a set of refinement factors for all the coarse grid parameters. An overall refinement factor N_{refine}
can be derived from these and this N_{refine} is the number of fine grid points for each coarse grid point.
The final grid will consist of a total of $N_{\text{c}} \times N_{\text{refine}}$ points. It should be emphasized that this fine
grid is still much coarser than the grid that would be required for a fully coherent search on the whole
data set, otherwise it would not have saved any computing power. It also should be emphasized that
a search with more coherent segments divided from the whole data set does not necessarily require
less computing power. This is because the cost of a semi-coherent search has two parts: the cost of
analysing all the coherent segments and the cost of summing up the analysis result. The semi-coherent
method reduces the cost of the first part. If a data set is broken into too many coherent segments, the
cost of the second part (incoherent part) is dominant and thus the total cost starts to grow instead.

If one consider a stack-slide method of combining the results of the coherent analyses, the final

---

[2]the f bins of a Fourier transform of the observation data with T_{obs} duration have a spacing of $1/T_{\text{obs}}$.

detection statistic is then the average of the $\mathcal{F}$-statistic across the N segments:

$$\widehat{2\mathcal{F}} = \frac{1}{N} \sum_{\ell=1}^{N} 2\mathcal{F}_\ell. \tag{3.58}$$

Here, $2\mathcal{F}_\ell$ is the $2\mathcal{F}$ statistic of the ℓth segment. On the left side of the equation, the average $\widehat{2\mathcal{F}}$ is evaluated at a point on the fine grid during the incoherent summing step. On the right side, the $\mathcal{F}_\ell$ are evaluated at coarse grid points, ideally the one nearest to the chosen fine grid point. Since $2\mathcal{F}_\ell$ follows a non-central χ^2 distribution with 4 degrees of freedom, it follows that $N\widehat{2\mathcal{F}}$ follows a non-central χ^2 distribution with $4N$ degrees of freedom. The new non-centrality parameter is the sum of ρ^2 over the N segments. As long as the noise of the detector is stationary over the observation period which is longer than a day, and each segment has the same observation duration, ρ^2 will be approximately constant over each segment, and thus the final non-centrality parameter can be well approximated by $N\rho^2$.

The false alarm probability of the semi-coherent detection statistics, which is the probability of obtaining a value of $\widehat{2\mathcal{F}}$ above a given threshold $\widehat{2\mathcal{F}}^\star$ in the absence of a signal, has the form:

$$P_{\mathrm{FA}}(\widehat{2\mathcal{F}}^\star) = \int_{N\widehat{2\mathcal{F}}^\star}^{\infty} \chi^2_{4N}(x|0)dx. \tag{3.59}$$

Here, $\chi^2_{4N}(x|0)$ denotes a central (non-centrality parameter is 0) χ^2 distribution with $4N$ degrees of freedom. Following Equation (3.53), the detection probability of the semi-coherent detection statistics is:

$$P_{\mathrm{D}}(\widehat{2\mathcal{F}}^\star|\rho^2) = \int_{N\widehat{2\mathcal{F}}^\star}^{\infty} \chi^2_{4N}(x|N\rho^2)dx. \tag{3.60}$$

3.5 Software and computing facilities

Gravitational wave data analysis is very challenging due to the extremely small GW amplitude h_0. Making a detection requires various efficient algorithms and computing facilities with great computational power. In this section, I will focus on the softwares (algorithms) and the computing facilities that I used most often in my PhD projects and give a brief description of them. Some concepts introduced here will be referred in next chapters.

3.5.1 CW data analysis software

Various algorithms, helper functions and search pipelines used in GW data analysis have been developed. The LIGO Scientific Collaboration (LSC) collects them as a whole in the free and open-source software package called `LALSuite` (LSC Algorithm Library Suite) [20]. For my PhD projects, I have used some of the `LALApps` applications. I list them below and give a brief introduction on their usage and the main contributors.

- `lalapps_HierarchSearchGCT` (GCT) is a semi-coherent StackSlide CW search code based on the global correlations method [148, 150]. The GCT code is widely used in CW searches [36, 142, 177] and it is the search code used in the directed searches for CWs from 3 point targets and Galactic Centre (Chapters 5 and 6). Besides, it is also used to test and develop the optimisation method. The GCT code was written mainly by H. Pletsch and later mainly contributed by R. Prix, K. Wette, B. Machenschalk and D. Keitel. It should be noted that, for long observation durations (a few months or longer), there does not exist a reliable prediction for the mismatch distributions of the GCT template banks. For this reason, in order to effectively optimize the set-ups of our searches, I had to perform simulations and obtain realistic mismatch distribution. The Weave code developed by K. Wette [21] recently is thought to be the next generation of the GCT code, and it will improve the GCT framework in various aspects.

- `lalapps_Makefakedata_v4` is contributed by R. Prix, M. A. Papa, X. Siemens, B. Allen and C. Messenger. I used this code to generate the artificial data that contains the simulated signals. It is used in the mismatch distribution investigation step and the optimizition step.

- `lalapps_PredictFStat` is contributed by I. Gholami and R. Prix. I used it to calculate the expected (multi-detector) $2\mathcal{F}$ statistic for CW signals instead of actually performing a search. In the optimisation step, the $2\mathcal{F}$ statistic for every "cell" (Chapter 4) must be calculated which is quite time consuming. To speed up the optimisation procedure, I used `lalapps_PredictFStat` to get the predicted $2\mathcal{F}$ rather than the GCT code to perform a real search.

Apart from the software developed by LSC, I want to mention the MATLAB linear programming function `linprog` [22] which was used in the optimisation procedure. In this optimisation procedure, the entire parameter space is divided into many cells, and each cell is associated with a computing cost and a detection probability. For the optimisation on a search with multiple set-ups involved, linear programming is effective method to generate the optimisation result. Since I developed most of the optimisation codes on MATLAB, naturally I adopted `linprog` to solve the linear programming problems. Details about this can be found in Chapter 4 and Appendix 4.6.

3.5.2 ATLAS and Einstein@Home

As previously discussed, the sensitivity of CW searches with large parameter spaces also depends on how much computational power is available. There are several high performance computing facilities playing a very important role in GW data analysis. The ATLAS cluster of Albert Einstein Institute (AEI) in Hannover is one of them [75]. As the world's most powerful computing resource dedicated to GW data analysis, the ATLAS computing cluster is a tool of paramount importance[3]. It was launched in May 2008 with 1344 quad-core compute nodes and one month later it was ranked 58th in the world's and sixth in Germany fastest computers. The computing power of ATLAS has being upgraded in recent years, and currently it has more than 2500 compute nodes and about 2000 GPUs. As the

---

[3]Gamma ray and radio pulsar analyses are also performed on ATLAS.

most powerful cluster in the LSC, it is utilized by over 1000 LSC members, and many GW searches and data analyses have been done on ATLAS. As one of the PhD students of the AEI as well as a member of LSC, I am very lucky to have such a powerful cluster to use for my research. For instance, I used ATLAS to do is the investigation of mismatch distributions, which will be introduced in more details in Chapter 5. The realistic mismatch distribution is a crucial piece of information used in the optimisation of the searches I set up. To obtain the mismatch distributions for the thousands of candidate set-ups, I needed to perform Monte Carlo simulations which require large computing resource that only ATLAS can provide. Another example that used ATLAS is the timing of the codes. The whole idea of optimisation of search set-up is manipulating the computing power to maximize the detection probability. The realistic mismatch distribution, as mentioned before, is related to the detection probability. At the same time, the timing test result is related to the computing cost, so it's also very important information. R. Prix, C. Beer and I developed a timing model for the resampling algorithm and tested it on ATLAS. The details about this will also be given in Chapter 5.

Another very important and powerful computing resource is Einstein@Home [23]. It is a volunteer distributed computing project based on the BOINC framework [24, 68, 69], and uses volunteers' computers' idle time to search for not only the GW signals but also the radio and gamma ray signals from rotating neutron stars. Although no CW signal has been found yet, Einstein@Home has discovered 55 radio pulsars [25] and 18 gamma-ray pulsars [26] by November 2016. Currently, over a half million host computers are active in Einstein@Home and provide a sustained average computing power more than of 10^{15} floating point operations per second (PFLOPS), which corresponds to a place among the top 100 in the November 2016 Top500 list [27]. The wide-parameter CW searches are templated searches which don't need information exchange between the calculations for different templates, so they can run in parallel and are well suited to distributed computing. A number of CW searches have utilized the great computing power of Einstein@Home and many results from these searches have been published (see e.g. [51, 50, 52, 37, 177, 167]). At the moment I am writing this thesis, the search exploring the Galactic Centre using the GCT method is ongoing on Einstein@Home and it's expected to be finished in November, 2017.

Before each CW search runs on Einstein@Home, the whole search is divided into many small jobs with specified run time and data volume. Each of these jobs covers a subset of the whole parameter space. These tasks are then distributed to the hosts. Because the hardware and software environments of the host computers are not tightly controlled, computational errors and corruptions or problems during internet transfer may occur. To avoid these erroneous results, each task is distributed to at least two hosts so the results can be compared. This redundance doubles the computation but is necessary. The same task in two or more hosts defines the work unit (WU) which is the base unit containing the science results from the host computers. After accounting for the redundance effect, the computing power of Einstein@Home is approximately 12000 CPU cores.

We can use the Einstein@Home month (EM) as our computation unit, which corresponds to about 12000 CPU cores round the clock for one month. This number of CPU cores is evaluated in the average sense. However, in reality, the computing power of hosts varies by quite a lot. The tasks distributed to the Einstein@Home volunteers in the O1 all-sky search were designed to have an average runtime of 8 hours on one host. Because each host has different hardware and software environments, the
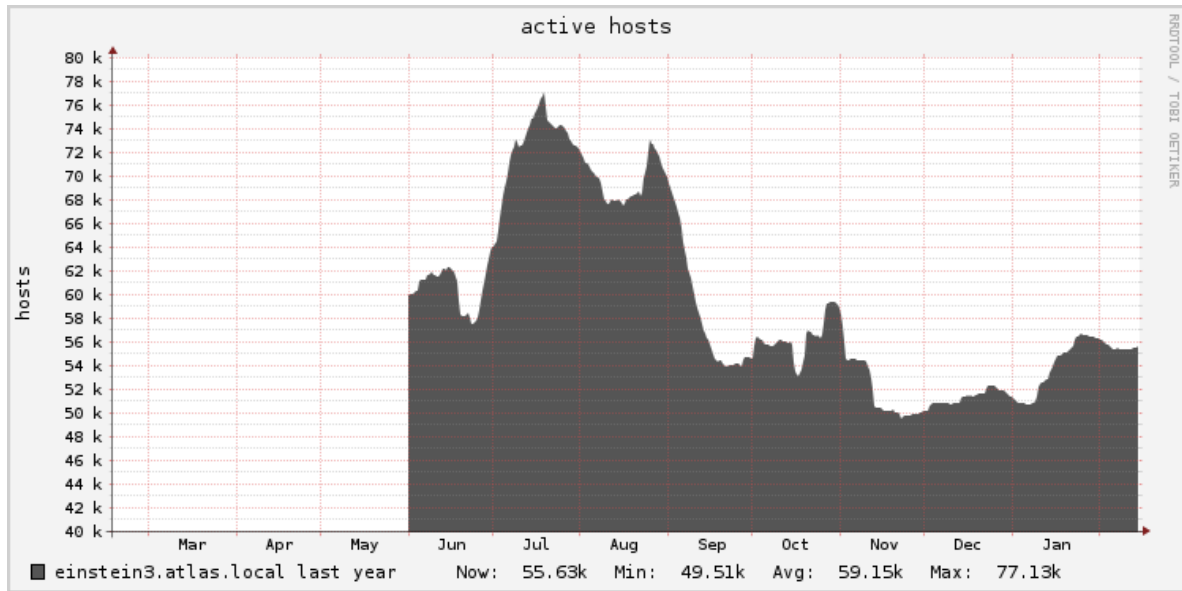
Figure 3.2: The number of active hosts of Einstein@Home from May 2016 to February 2017. Figure credit: Einstein@Home group [28].

runtime of the each individual host varies. The histogram of runtime showed two modes, one centred at 10 hours and the other centred at 24 hours. Further analysis led to the conclusion that it is possible to divide the entire host population of Einstein@Home into fast hosts and slow hosts based on the average runtimes in the test run. Hosts that had a runtime of less than 14 hours were considered fast hosts and hosts that needed more time per task on average were considered slow hosts. This then divided the available host population roughly into two halves. These two categories strongly are related to the CPU models. The Intel CPUs like E3, I7 were categorized as fast nodes and almost all of the hosts which have AMD CPUs were categorized as slow hosts by this method. In the searches that I designed, the computation amount per task for fast hosts is larger than the computation amount for slow hosts, in order to obtain roughly same run time both in fast and slow hosts.

Before each CW search starts, the expected run time on Einstein@Home needs to be estimated. Knowing when the search will be finished is necessary to make sure that the results are produced in a timely manner. The estimation of the run duration also depends on the number of active hosts which varies with time. Figure 3.2 shows the number of active hosts of Einstein@Home in the last 10 months. The number of active hosts varies with time and peaks to summer of 2016 and drops quickly around late August. This variation is determined by the occupation, age and custom of the population of volunteers, which we don't quite comprehend. Further investigation on this may improve the understanding of how it changes with time and thus allow us to estimate run time more accurately. This topic will be discussed again in Chapters 5 and 6.

Chapter 4

Optimization method

As previously discussed, wide-parameter-space CW searches are computationally limited. Therefore it is extremely important that available computational resources are utilized wisely. In my first PhD project, under the supervision of M. A. Papa and B. Krishnan, I develop a general framework to determine what waveforms to search for, what search set-up to use and what astrophysical targets to point to for a given computational budget. The method that I propose determines these factors in such a way that the probability of making a detection is maximum. This method is illustrated by considering a semi-coherent search scheme, a set of interesting astrophysical targets and a few different prior assumptions on the signal parameters. From this illustrative example, interesting results are found: for example, Vela Jr is a more promising target than Cassiopeia A (Cas A). However in past searches many more compute cycles have been invested searching for a continuous signal from Cas A than from Vela Jr.

Caveats:
A lot of the material in this chapter is taken verbatim from [133]. Refer to Appendix A for details on my contributions.

4.1   Introduction

There are a number of interesting astrophysical targets for CW searches. Known pulsars are particularly good examples for which we know all of the parameters. Searches, where the sky-position, frequency and spindown are all known accurately, are referred to as *targeted* searches of targets in the literature. In these cases it is fairly straightforward, at least from a computational point of view, to search for possible GW signals emitted by the neutron star. A number of such searches have been carried out (see e.g. [38]). Most notably, for the Crab and Vela pulsars, the upper-limit on the GW amplitude is more constraining than the limit one derives by assuming that all of the observed spindown is due to GW emission [48, 43, 39].

At the other extreme we have the *blind* searches where nothing is known *a priori* about the source parameters. One has to survey a data set which could span several months or years, a frequency range of $\mathcal{O}(10^3)$ Hz, the entire sky and a reasonable choice of spindown parameters. Such searches are computationally limited and are, by far, the most computationally challenging GW searches of all. Results from a number of such searches have been published (see e.g. [46, 45, 47, 49, 44, 51, 50, 52]). Some of these results [51, 50, 52]) have utilized the public distributed computing project Einstein@Home [23].

Between these two extremes lie the *directed* searches where one targets interesting astrophysical objects or regions. In this case the signals parameters are partially known. In particular the sky-position is known accurately. [1] but no information is available on the spin frequency of the star and hence the GW frequency. Such searches are also computationally limited. A few such results have been published in the literature so far : a search for CW signals from the supernova remnant Cassiopeia A [42], from the galactic center [36] which could potentially harbor a number of young and rapidly rotating neutron stars and from nine young supernova remnants [35]. A deep search for CW signals from Cassiopeia A (Cas A)using Einstein@Home was completed last year. All of these searches were computationally limited. We expect that similar directed searches will be of great interest in the near future.

When the searches are computationally limited (the directed and blind searches), the most commonly employed methods are *semi-coherent*: rather that matching the full ∼year long data set with coherent signal templates, one splits up the data set into N shorter segments (stacks) typically ∼hours or ∼days long. Each segment is matched with a set of signal templates coherently and finally the results of these N searches are combined incoherently. Descriptions of such methods can be found in [84, 83, 124, 143, 123, 89, 150, 148]. Semi-coherent methods have also been considered as parts of multi-stage hierarchical schemes for surveying large parameter spaces, see for example [89, 83, 163].

It is very important to spend the computational resources wisely: what search set-up to use, what astrophysical objects to target and for each target what waveforms to search can make the difference between making a detection or missing it.

In this paper I shall focus on the directed searches though the general scheme I propose is also applicable to the blind searches. I assume that I have a list of N_{t} potential targets. For each of the targets I assume that I know how far away and old it is. I also make assumptions on the likelihood for different values of the signal amplitude, its frequency and the frequency-derivates, as discussed in Sec. 5.2. Given these priors, the question I address is: what sources should we target? What is the optimal search set-up and what is the search region in frequency and spindown that maximizes our probability of making a detection? Various parts of this problem have been partially addressed previously and here I present a complete solution. I explain how the key search pipeline parameters can be determined, which source and which part of parameter space to target taking into account the prior astrophysical knowledge, the performance of the search software, the available computational resources and the quality of the data from the GW detectors.

Previous works have typically fixed the parameter space to be searched *a priori* – often based on

---

[1]To be more explicitly, it means the uncertainty in sky-position is smaller than our search tolerance which is typically 1×10^{-4} rad.

reasonable astrophysical arguments – and then optimized for the search parameters (e.g. [140, 89, 152]). Conversely there are studies of what parameter space to search (see e.g. [141, 121, 170, 139]) which have largely neglected the computational cost of the GW search. One of the aims of the present work is to integrate both aspects of the problem.

4.2   General optimisation scheme

I begin by discretizing the whole parameter space into many small cells such that:

- The cells are non-overlapping, and the union of all the cells covers the parameter space of interest

- The computing costs and detection probabilities for each target vary smoothly from one cell to the next

- The cost of searching any cell for any target is much smaller that the total computational cost budget available

As long as these conditions are satisfied this optimisation method will be largely insensitive to how fine the cell- discretization is chosen.

I associate to each cell, astrophysical target and search set-up a probability to detect a signal with parameters in that cell and the computing cost for searching over the cell waveform parameters with a particular semi-coherent search set-up. The goal of this work is to choose a collection of cells and targets such that:

- The sum of the computational cost for searching all the chosen cells is within the computational budget, and

- The sum of the probability values for the chosen cells is maximized. By this I mean that other choices of cells, search set-ups or/and targets would yield a lower detection probability.

4.2.1   Single set-up case

To illustrate the procedure we begin by considering a single astrophysical target, i.e. a source corresponding to a single sky-position, unknown frequency and unknown spindowns. We also restrict ourselves to a single search set-up, i.e. we assume a specific coherent segment length and number of segments.

Let us indicate the frequency-spindown parameter space as $\mathcal{P}$. Based on available astrophysical information we define a prior probability density $P(f, \dot{f}, \ddot{f})$ for different frequency and spindown values[2] I will later make a particular choice for this prior but the general method we describe now is applicable for any choice.

---

[2]The third order spin-down $\dddot{f}$ does not need to be searched over because, even for the youngest target, a search over third order spin downs is not necessary for the coherent ($\sim$ 20 days) and observation times ($\sim$ monthes).

I break the space $\mathcal{P}$ into non-overlapping cells small enough so that the conditions described above are satisfied. It is simplest to consider rectangular cells defined by frequency and spindown widths $df, d\dot{f}, d\ddot{f}$. Next I assign a detection probability to each cell for a given data set from an arbitrary number of detectors and spanning a total duration T_{obs}. I assume that a semi-coherent method is applied with the data broken up onto N segments and the detection statistic is $\widehat{2\mathcal{F}}$, the average value of $2\mathcal{F}$ over the segments.

I calculate the detection probability for each parameter space cell c. In order to do this I need to assume distributions (priors) for the parameters of the population of signals in that cell. In particular, I need priors for $(\alpha, \delta), f, \dot{f}, \ddot{f}, \psi, \cos\iota, \phi_0$ and h_0. I assume that a compact object is present at the position of the astrophysical target and hence we will take the priors on (α, δ) to be 1. The standard physical priors for $\psi, \cos\iota, \phi_0$ are uniform, leading to an average detection probability for such a population, having assumed a specific value of h_0 and $f, \dot{f}, \ddot{f}$:

$$\langle \eta \rangle_{\phi_0, \psi, \cos\iota}(h_0) := \frac{1}{8\pi^2} \int_{-1}^{1} d\cos\iota \int_{0}^{2\pi} d\psi \int_{0}^{2\pi} d\Phi_0 \, \eta \, . \tag{4.1}$$

For a population of signals with a prior distribution on the amplitude, $p(h_0)$, the average detection probability having assumed values of $f, \dot{f}, \ddot{f}$ is:

$$\langle \eta \rangle_{h_0, \cos\iota, \psi, \phi_0} = \int_{o}^{\infty} p(h_0) \langle \eta \rangle_{\cos\iota, \psi, \phi_0} \, dh_0 \, . \tag{4.2}$$

Finally folding in the prior $P(f, \dot{f}, \ddot{f} \ldots | I)$ with the detection probability $\langle \eta \rangle$, I find the total probability of detection for a cell:

$$P_c = \langle \eta \rangle_{h_0, \cos\iota, \psi, \phi_0} P(f_c, \dot{f}_c, \ddot{f}_c) df \, d\dot{f} \, d\ddot{f} \, . \tag{4.3}$$

I note the difference between P_c and $\langle \eta \rangle$. $\langle \eta \rangle$ is the detection probability in a cell with an assumption that the signal is actually in that cell, and P_c is the real detection probability in a cell because it contains the prior probability density for that cell. I also note that $\langle \eta \rangle_{h_0, \cos\iota, psi, \phi}$ is actually independent of $\ddot{f}$. In fact, it depends on $\dot{f}$ only through the prior $p(h_0)$. Thus, since the prior $(f, \dot{f}, \ddot{f})$ is normalised to unity, I can drop the $\ddot{f}$ dependence in the above equation:

$$P_c = \langle \eta \rangle_{h_0, \cos\iota, \psi, \phi_0} P(f_c, \dot{f}_c) df \, d\dot{f} \, . \tag{4.4}$$

The detection probability over the whole parameter space is

$$P_{\mathrm{D}} = \int_{\mathcal{P}} \langle \eta \rangle_{h_0, \cos\iota, \psi, \phi_0} P(f, \dot{f}) df \, d\dot{f} \, . \tag{4.5}$$

Computational cost is the other quantity of interest. I define a computational cost density $C(f, \dot{f}, \ddot{f})$ such that the cost of searching a cell is

$$c_c = C(f_c, \dot{f}_c, \ddot{f}_c) df \, d\dot{f} \, d\ddot{f} \, . \tag{4.6}$$

In practice, the cost function is strictly speaking not a density because of overhead and startup costs associated with a search which make the cost not strictly proportional to the size of the parameter space cell. However I shall neglect this because in practice these overhead costs are controlled and can be kept to a minimum by an appropriate choice of cell size.

I want to define a ranking criterion on the cells such that when we pick, according to that criterion, the top $n_{C_{\max}}$ cells that exhaust the computing budget, the resulting total detection probability ($P_{\mathrm{sum}} = \sum_i^{n_{C_{\max}}} P_i$) is maximum. In other words any other choice of cells would yield a lower value of the total detection probability P_{sum}. These top $n_{C_{\max}}$ cells are then the ones that I should search.

I use the detection probability and the computational cost to define a ranking for each cell. I motivate this as follows. As explained at the beginning of this Section, the cells are small enough so that the cost for any cell is much smaller than the total available computational budget $C_{\max}$. If all the cells had the same cost, then clearly I would use the detection probability to rank the cells and I would simply pick as many top cells as I can before exhausting the computing budget. However, the cells will generally have different costs associated with them hence the ranking by detection probability does not ensure that the total detection probability is maximized. A way to fix this would be to adjust the size of the cells so that they do have the same cost. A simpler method is to instead use the ratio between the detection probability and the cost, which I call efficiency, to rank the cells. Thus for each cell I construct the ratio

$$e(f_c, \dot{f}_c, \ddot{f}_c) = \frac{\langle \eta \rangle_{h_0, \cos \iota, \psi, \phi_0} P(f_c, \dot{f}_c, \ddot{f}_c | I)}{C(f_c, \dot{f}_c, \ddot{f}_c)} \,. \tag{4.7}$$

Note that the efficiency e contains information about the search set-up through $\langle \eta \rangle$ and C, the detector sensitivity through $\langle \eta \rangle$, the astrophysical priors through $P(f_c, \dot{f}_c, \ddot{f}_c)$, and the computational cost through C.

A more rigorous argument that the efficiency is the correct ranking function can be modeled on the proof of the Neyman-Pearson lemma found in most statistics textbooks. I can formulate the problem as finding a region $\mathcal{P}_0 \subset \mathcal{P}$ in the parameter space $(f, \dot{f}, \ddot{f})$, such that the cost of searching over $\mathcal{P}_0$ is a chosen value $C_{\max}$

$$\int_{\mathcal{P}_0} C(f, \dot{f}, \ddot{f}) df \, d\dot{f} \, d\ddot{f} = C_{\max} \,. \tag{4.8}$$

and such that the detection probability over the region $\mathcal{P}_0$ is larger than over any other region that satisfies the computing budget requirement (Equation (4.8)):

$$\int_{\mathcal{P}_0} \langle \eta \rangle_{h_0, \cos \iota, \psi, \phi_0} P(f, \dot{f}, \ddot{f}) df \, d\dot{f} \, d\ddot{f} = P_{\max} \,. \tag{4.9}$$

With the problem formulated in this way, the Neyman-Pearson lemma is directly applicable and it tells us that the optimal choice of the region $\mathcal{P}_0$ is to consider level sets of the efficiency function. For a given threshold $e_{\min}$ on the efficiency, the condition $e(f_c, \dot{f}_c, \ddot{f}_c) \geq e_{\min}$ defines a region $\mathcal{P}_0$. I choose $e_{\min}$ so that the region $\mathcal{P}_0$ satisfies the computational cost constraint for a given maximum budget $C_{\max}$ according to Equation (4.8).

The optimisation procedure for a single source and a given set-up is then straightforward. For each cell I compute the efficiency e_c, pick the cells starting from the one with the largest efficiency and continue till I have used up all the computing power $C_{\max}$. By doing this, I maximise the probability with a limited computing power budget. If I have more than a single astrophysical target I can still use this same ranking criterion: I consider the parameter space cells from the different targets all together and drop the distinction between the different targets. The same procedure described above will yield the optimal detection probability.

4.2.2   The general case

The efficiency ranking introduced in the previous subsection is applicable when I constrain the realm of possible searches to a single search set-up for all the cells and for all the sources. It is clear that this is not optimal and I would gain by allowing for varying set-ups. If I do this I also need to impose the additional constraint:

- Each parameter space cell for a given source, must be chosen only once,

because it would clearly be wasteful to search the same cell in parameter space for the same source more than once with different set-ups. The Neyman-Pearson method used earlier cannot incorporate this additional constraint and I must modify this optimisation algorithm.

I reformulate this optimisation problem in such a way that the widely used method of linear programming (LP) is applicable. LP is a optimisation method which extremizes a linear combination of the parameters also fulfilling a set of inequalities [92].

I start again with the discrete form of Equations (4.8) and (4.9) using the cells as constructed earlier. Let an integer i label each cell: $1 \leq i \leq N_f \times N_{\dot{f}}$. For simplicity I consider searches with a fixed total observation time, 300 days, and use a varying number of segments N to indicate different coherent observation time-baselines. For each cell, I can pick among different set-ups, i.e. different values of N. Let another integer s label the different set-ups: $1 \leq s \leq n_s$. I now introduce an index j that uniquely labels every different cell-set-up combination: $j \leftrightarrow (i, s)$ and $1 \leq j \leq n_s \times N_f \times N_{\dot{f}}$. Finding the optimal solution for this problem means finding which {cell,set-up} should be picked and which should be discarded. I describe this choice with an occupation index X_j:

$$X_j = \begin{cases} 1, & \text{if } j \text{ is chosen,} \\ 0, & \text{if } j \text{ is discarded.} \end{cases}$$

The ordered set of X_j values with $1 \leq j \leq n_s \times N_f \times N_{\dot{f}}$ constitutes a binary number with $n_s \times N_f \times N_{\dot{f}}$ digits. The total probability over the set of chosen cells, which is the quantity that I want to maximize, is

$$P_{\text{sum}} = \sum_j P_j X_j \tag{4.10}$$

with P_j being the probability of the cell/set-up $j \leftrightarrow (i, s)$. The computational cost constraint can be expressed as:

$$\sum_j C_j X_j \leq C_{\max} \tag{4.11}$$

I use LP to find the values of X_j that satisfy (4.10) under the constraint (4.11), and taking the X_j to be real numbers rather than integers. More details on this method, and the reason why the optimisation procedure yields (mostly) integers rather than real numbers can be found in Section 4.6.

If I consider more than a single target and want to optimize also over targets t, the problem does not change in nature. I simply consider more (cell,set-ups) combinations, each now also labelled by a target "t" index:

$$\begin{cases} X_{i,s} & \to X_{(i,s)_t} \\ C_{i,s} & \to C_{(i,s)_t}. \end{cases}$$

I want to find the combination of $X_{(i,s)_t}$ values that maximizes

$$P_{\text{sum}} = \sum_t \sum_{(i,s)_t} P_{(i,s)_t} X_{(i,s)_t} \tag{4.12}$$

with the constraints

$$\begin{cases} \sum_t \sum_{i,s} C_{i,s_t} X_{i,s_t} \leq C_{\max} \\ \sum_t \sum_s X_{i,s_t} \leq 1 \text{ and } X_{i,s_t} \geq 0 & \text{for every } (i,t). \end{cases}$$

I emphasize that the solution to this optimisation problem $X_{(i,s)_t}$ solves the problem that I posed in the introduction: it tells us what astrophysical targets (t) I should search; for each target what frequency-spindown values (i) I should search and what semi-coherent search set-up (s) to use in each parameter space cell. Moreover, the scheme incorporates, through the priors, any astrophysical information on the distribution of the relevant signal parameters.

4.3 Examples of the optimisation scheme

I now illustrate the optimisation scheme with a very specific and practical example, namely searching a list of potential targets on the public distributed computing project Einstein@Home [23].

The sources that I consider are taken from [35] and are listed in Table 5.3. This list comprises supernova-remnants (SNR) whose position in the sky is very well known (better than second of arc accuracy [3]), and described by their equatorial sky coordinates α, δ. I associate with each source its estimated age $\tau_t \pm d\tau_t$ and an estimate of what I believe is the maximum intrinsic GW amplitude that it could be emitting[4]: $h_{0\,t}^{\max}$. I label the different point sources with an index t, and $t = 1 \ldots N_t$.

4.3.1 Astrophysical priors

In order to compute the detection probability in every cell I have to choose the prior on the signal amplitude h_0: $p(h_0)$ (see Equations (4.4) and (4.2)). The most relevant parameter that h_0 depends on,

---

[3]The tolerance of accuracy is about half minute of arc for a search with a coherent duration shorter than 20 days and the highest frequency lower than 1500 Hz.

[4]This is the age-related spindown limit defined for example in [42].

Table 4.1: Point source targets considered in this chapter

SNR G name	Other name	Point source J	D_{kpc}	τ_{kyr}	$10^{25} h_0^{\mathrm{age}}$
111.7–2.1	Cas A	232327.9+584842	3.3–3.7	0.31–0.35	12
189.1+3.0	IC 443	061705.3+222127	1.5	3–30	3
266.2–1.2	Vela Jr	085201.4–461753	0.2–0.75	0.7–4.3	15–140
347.3–0.5		171328.3–394953	1.3	1.6	14
350.1–0.3		172054.5–372652	4.5	0.9	5.3

Note that the source Vela Jr. has uncertainties both in age and distance. One measures its angular size θ and expansion rate R. It follows that the ratio of the distance D and the age τ is given by $D/\tau = R/\theta$. Thus one does not measure D or τ independently but only the ratio and so a larger D implies a larger τ.

is the ellipticity ε defined in Equation (3.13). I thus recast the integral (4.2) on h_0 as an integral on ε. Unfortunately the ellipticity is also the least known parameter so reflecting our ignorance I take a flat probability density on $\log \varepsilon$ within a conservative range of values. Consider a cell i centered at a particular frequency f_i and spindown $\dot{f}_i$ for a particular source chosen from Table 5.3. For this cell I can consider two upper limits on ε: The first is the spindown ellipticity, $\varepsilon_x^{\mathrm{sd}}$ of Equation (5.9), with $x = 0.01$, which is consistent with the latest limits on the emission of gravitational waves from the Crab pulsar [38]. The second limit is based on the results of [107], according to which it is unrealistic to expect ε to exceed $\sim 10^{-4}$. I thus set a cell-dependent maximum acceptable value of ε as (for ease of notation I drop the subscript "x" in $\varepsilon_x^{\mathrm{sd}}$):

$$\varepsilon_i^{\mathrm{max}} = \min(10^{-4},\ \varepsilon_i^{\mathrm{sd}}). \tag{4.13}$$

I consider now the minimum value of ε. If the neutron star were perfectly axisymmetric then $\varepsilon = 0$, $h_0 = 0$ and there would be no GW emission. However deviations from this axisymmetric configuration are expected due to the internal magnetic field, at a level that should be at least $\varepsilon \sim 10^{-14}$ [70]. I hence take

$$\varepsilon^{\mathrm{min}} = 10^{-14}. \tag{4.14}$$

Based on the above discussion, the prior $p(\varepsilon)$ is:

$$p(\varepsilon) = \begin{cases} \frac{1}{\varepsilon} \frac{1}{\log(\varepsilon^{\mathrm{max}}/\varepsilon^{\mathrm{min}})} & \varepsilon^{\mathrm{min}} < \varepsilon < \varepsilon^{\mathrm{max}} \\ 0 & \text{elsewhere} . \end{cases} \tag{4.15}$$

As an illustration of this choice of prior, consider Cas A taken to be a distance of 3.5 kpc from us. Let us assume the star to be emitting GWs at some frequency f, the fraction of the rotational energy going into GWs to be $x = 0.01$ and the standard value of the moment of inertia I to be $10^{38}\,\mathrm{kg\,m^2}$
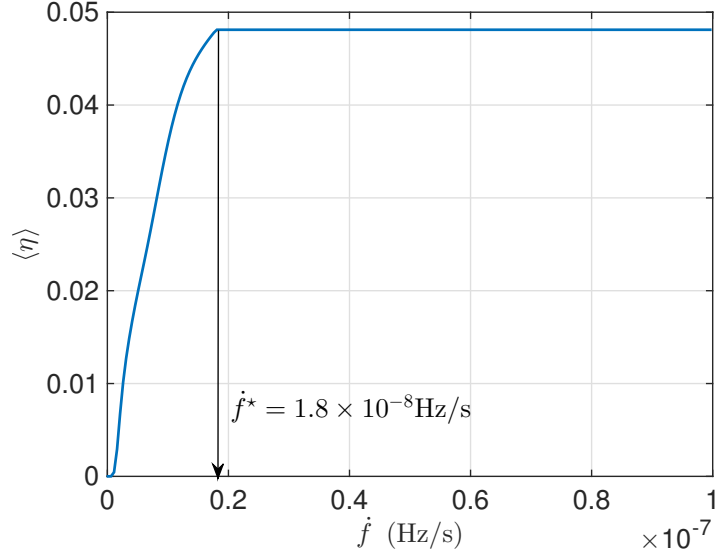
Figure 4.1: Detection probability as a function of the source's spindown, for a source at the position of Cas A, emitting at 101 Hz and being searched with 20-day coherent time-baseline segments over 300 days. Due to the prior on h_0 the detection probability stops increasing at $\dot{f}^\star = 1.8 \times 10^{-8}$Hz/s.

[5](these two assumptions are also used for all the other results in this chapter). At small $|\dot{f}|$, $\varepsilon^{\max}$ is given by the spindown limit $\varepsilon^{\mathrm{sd}}(f, \dot{f})$. As $|\dot{f}|$ increases, the spindown limit $\varepsilon^{\mathrm{sd}}(f, \dot{f})$ also increases and with it also $\varepsilon^{\max}$ until it reaches the value 10^{-4}. This happens at a crossover spin down value of

$$\dot{f}^\star = -1.71 \times 10^{-8}\mathrm{Hz/s} \left(\frac{f}{100\mathrm{Hz}} \right)^5 . \tag{4.16}$$

For spindown values in absolute value larger than this crossover spindown value, $h_0^{\max}$ ceases to increase and remains constant at a value that corresponds to the maximum ellipticity value that I have set: 10^{-4}. Correspondingly the detection probability $\langle \eta \rangle$ at a fixed search frequency will cease to increase as a function of the spindown. This is shown in Figure 4.1 where I assumed $f = 101\,\mathrm{Hz}$, a 20 day coherent integration time and 300 days observation time.

What about the prior $P(f, \dot{f})$? I consider either uniform or log-uniform priors on all these variables

---

[5]The inertia moment of a NS also has uncertainty. Current NS equation-of-state models still allow the inertia moment to be up to a factor of 5 larger than $10^{38}\,\mathrm{kg\,m^2}$[115]. However, since the information of inertia moments of the sources considered in this thesis is not known, I assume I to be the fixed number $10^{38}\,\mathrm{kg\,m^2}$. Note that difference of I in different sources can change the change the prioritization of sources and the optimaztion result.

with ranges sufficiently large to cover all possible values of these parameters[6]:

$$\begin{cases} 0\,\text{Hz} \leq & f \leq 1500\,\text{Hz} \\ -1 \times 10^{-7}\,\text{Hz/s} \leq & \dot{f} \leq 0 \\ 0\,\text{Hz/s}^2 \leq & \ddot{f} \leq 5\dot{f}^2/f. \end{cases} \tag{4.17}$$

For the second order spindown parameter I note that if the frequency evolution follows $\dot{f} \propto f^n$, where n is the braking index, then

$$\ddot{f} = n\dot{f}^2/f. \tag{4.18}$$

For pure GW emission $n = 5$, for all other possible mechanisms $n < 5$ and in particular for pure electromagnetic emission $n = 3$ (see e.g. [164]). Hence our range for $\ddot{f}$ in (4.17) encompasses all combinations of emission mechanisms.

Different ranges on $\dot{f}$, $\ddot{f}$ and ε could have been set, based on the estimates of the age of the astrophysical targets. If I assume that the object has been spinning down by f at a spindown rate $\dot{f}$ during a time τ_c, its characteristic age, due to some mechanism with a braking index n, then

$$\tau_\text{c} = \frac{1}{n-1}\frac{f}{|\dot{f}|}. \tag{4.19}$$

By maximising Equation (4.19) with respect to n I derive a maximum range for $\dot{f}$. I then use that value in Equation (4.18) to derive the largest range for $\ddot{f}$. The conservative search ranges are then

$$\begin{cases} |\dot{f}| < & f/\tau_\text{c} \\ |\ddot{f}| < & 5f/\tau_\text{c}^2, \end{cases} \tag{4.20}$$

having taken the estimated age of the object as a proxy for its characteristic age τ_c. Note that these maximum ranges for $\dot{f}$ and $\ddot{f}$ correspond to different n values, namely 2 and 5. This is physically inconsistent for any single source but it ensures the broadest prior range over the search values now, allowing for deviations from the constant braking index model in the past evolution of the star.

Let us assume $n = 5$, which means emission at the spindown limit, and recast the GW amplitude spindown upper limit (Equation (3.15)) as well as the corresponding ellipticity (Equation (3.17)), in terms of τ_c :

$$h_0^\text{sd} = \frac{1}{d}\sqrt{\frac{5GI}{8c^3\tau}} \tag{4.21}$$

and

$$\varepsilon^\text{age} = \frac{c^2}{16\pi^2 f^2}\sqrt{\frac{10c}{GI\tau}}. \tag{4.22}$$

When $n = 5$ then $\tau_\text{c} = f/4|\dot{f}|$ is the shortest lifetime compared to the characteristic ages for other emission mechanisms. Correspondingly the necessary spindown is the largest, and so are the GW

---

[6]In other words, if the detectors were infinitely sensitive and $\langle\eta\rangle$ in Equation (4.5) was equal to one, then, with the choice of priors also $P_\text{D} = 1$.

amplitude upper limit and the ellipticity. Hence, choosing $n = 5$ allows for the highest possible value of ε. Correspondingly, if I choose to fold in the prior information on the age of the object Equation (4.13) becomes:

$$\varepsilon_i^{\mathrm{max}} = \min(10^{-4},\ \varepsilon_i^{\mathrm{sd}},\ \varepsilon_i^{\mathrm{age}}). \tag{4.23}$$

I remind the reader that the index i labels a particular $f, \dot{f}$ cell in parameter space.

4.3.2 Grid spacings

Given the ranges for f, $\dot{f}$ and $\ddot{f}$ and the duration T of the coherent segments, I now need to specify the number of templates needed to cover the parameter space covered by each cell. This is a pre-requisite for estimating the computing cost for that cell. As discussed earlier, a semi-coherent search requires a set of templates for the coherent step and a set for the semi-coherent steps. These are referred to, as the coarse and fine grids respectively. The grid spacings in each search parameter can be parametrized in terms of nominal mismatches $m_f, m_{\dot{f}}, m_{\ddot{f}}$ in $f, \dot{f}, \ddot{f}$ respectively[149]:

$$\delta f = \frac{\sqrt{12 m_f}}{\pi T}, \tag{4.24}$$

$$\delta \dot{f} = \frac{\sqrt{180 m_{\dot{f}}}}{\pi T^2}, \tag{4.25}$$

$$\delta \ddot{f} = \frac{\sqrt{25200 m_{\ddot{f}}}}{\pi T^3}. \tag{4.26}$$

Following that, the semi-coherent grid spacing in each dimension is taken a factor γ^k finer than the coarse grid one:

$$(\delta f^{(k)})_{\mathrm{semi-coh}} = \frac{\delta f^{(k)}}{\gamma^{(k)}}, \quad k = 1, 2 \ldots \tag{4.27}$$

with the index k labelling the frequency and spindown parameters: $f^{(1)} = \dot{f}$ and $f^{(2)} = \ddot{f}$. The refinement factors $\gamma^{(k)}$ depend on the number of segments:

$$\gamma^{(1)} = \sqrt{5N^2 - 4}, \tag{4.28}$$

$$\gamma^{(2)} = \frac{\sqrt{35N^4 - 140N^2 + 108}}{\sqrt{3}}. \tag{4.29}$$

I note that in the simplified problem that I consider here I do not include the loss of signal-to-noise ratio associated with the given mismatches and I do not optimize with respect to searches with different grids.

4.4 Application of the optimisation scheme under different assumptions

I now apply the optimisation scheme to a search for a CW signal from the sources listed in Table 5.3. I will consider different priors and show intermediate optimisation results: namely I firstly fix the search

set-up and the target and eventually optimise also over these. In Section 4.4.1, I will use uniform priors on $f, \dot{f}$ in order to illustrate the main features of this optimisation scheme. In Section 4.4.2 I will show the results for the log-uniform priors which are more descriptions of our ignorance.

4.4.1   Uniform priors in f and $\dot{f}$

Optimizing at fixed search set-up and separately for each target

For illustration purposes, I consider the simplest case, namely when I have a pre-determined search set-up, i.e. a fixed value for the number of coherent segments N. The optimisation scheme will rank the parameter space cells of all the sources in decreasing order of detection probability and hence yield the parameter space regions that should be searched for each source. I will consider the data to span a total observation time of 300 days, to be from the LIGO Hanford and Livingston detectors at the best sensitivity level of the S6 science run[7] and with a duty factor of 50%. I assume as computing budget 12-Einstein@Home months (EMs). 1EM corresponds to about 12,000 CPU cores round the clock. Here and throughout this chapter[8] I use $m_f = m_{\dot{f}} = m_{\ddot{f}}$=0.18 in Equations (5.1) to (46) for the grid spacings. Note, these are arbitrary but reasonable choices of values illustrative of actual searches. I shall take the coherent segments to each be 10 days long, in this section.

The result will depend on what prior I choose. I work with two choices: one that does not fold in the age information (Equation (4.13)) and one that does (Equation (5.8)). I name these priors the "distance-based prior" and the "age-based prior", respectively. In this section I present results for the distance-based priors only and the age-based prior results will be discussed later.

The source in Table 5.3 closest to us is Vela Jr with distance estimates ranging from 0.2 to 0.75 kpc. Age and distance estimates are highly uncertain due to the overlap of the SNR with the main Vela SNR and possible interaction between them. Other targets such as IC 443 and G347.3 are relatively close to Earth, with distances of 1.5 kpc and 1.3 kpc respectively. The estimated distance of Cas A is between 3.3 and 3.7 kpc, which is not very close compared with the previous three source I mentioned above. However, Cas A is the youngest source and I include it in our list as a point of comparison.

I define a quantity $\mathcal{R}$ as the sum of detection probabilities for the parameter space cells which are chosen for a given source:

$$\mathcal{R} = \int_{\mathcal{P}_0} \langle \eta \rangle_{h_0, \cos \iota, \psi, \phi_0} P(f, \dot{f}) df \, d\dot{f} \,. \tag{4.30}$$
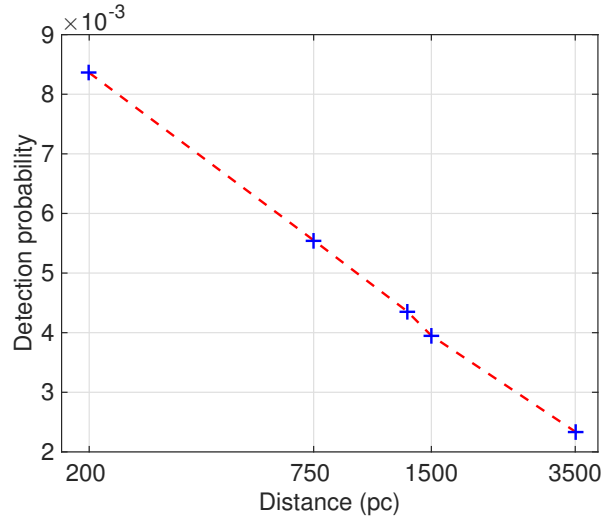
Note that $\mathcal{R}$ is also the actual highest detection probability that one can obtain for that source with the given computing budget. Clearly the higher the $\mathcal{R}$, the more promising is a search for the corresponding target. For a given amount of computing power $C_{\max}$, sources with higher $\mathcal{R}$ are more promising.

The highest value of $\mathcal{R}$, about 1%, is obtained with a search that targets the closest source, Vela Jr, at 200 pc. For the other targets the detection probability is even lower and decreases with increasing distance as summarized in Figure 4.2(a).
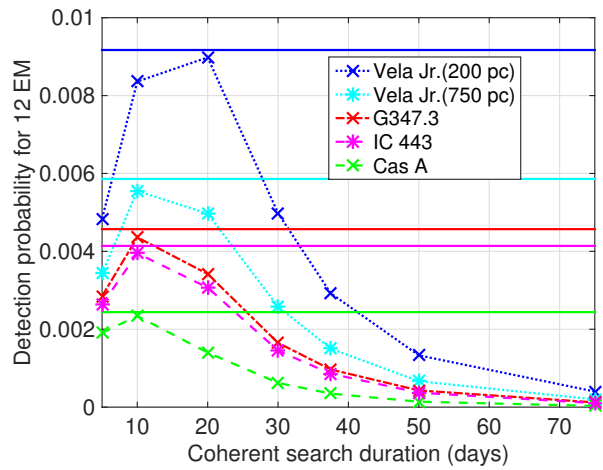
---

[7]https://github.com/gravitationalarry/LIGO-T1100338/blob/master/H1-SPECTRA-962268343-BEST.txt

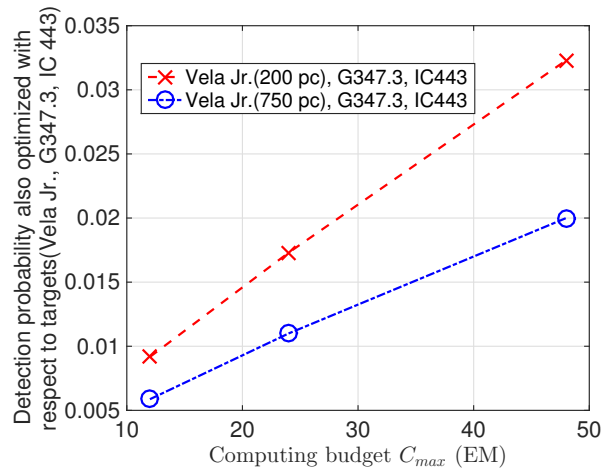[8] The definition of EM is different in Chapter 5 and 6 for practical reasons.

(a) $\mathcal{R}$ versus distance

(b) $\mathcal{R}$ versus T_{coh}

(c) $\mathcal{R}$ versus $C_{\max}$

Figure 4.2: Detection probability for various targets and search set-ups having assumed uniform and distance-based priors. The distances that were assumed for the targets are: Vela Jr (C) 200 pc, Vela Jr (F) 750 pc, G 347.3 1.3 kpc, IC443 1.5kpc, Cas A 3.5 kpc.

Table 4.2: $\mathcal{R}$ results with f and $\dot{f}$ uniform priors and distance-based priors. The highest $\mathcal{R}$ with respect to set-up is in bold font.

Name	D_{kpc}	$10^3\mathcal{R}$							LP Optimized		
		5D	10D	20D	30D	37.5D	50D	75D	12EM	24EM	48EM
		Computing Budget: 12EM									
Cas A	3.5	1.91	**2.34**	1.40	0.622	0.347	0.140	0.032	2.44	4.33	–
IC 443	1.5	2.63	**3.95**	3.07	1.45	0.858	0.371	0.104	4.14	7.33	–
G347.3	1.3	2.85	**4.36**	3.42	1.65	0.966	0.429	0.122	4.57	8.19	–
Vela Jr	0.2	4.84	8.36	**8.98**	4.98	2.92	1.33	0.401	9.17	17.3	–
Vela Jr	0.75	3.43	**5.55**	4.97	2.58	1.50	0.666	0.199	5.86	10.9	–
Top 3 (0.2 kpc)	–	–	–	–	–	–	–	–	9.17	17.3	32.3
Top 3 (0.75 kpc)	–	–	–	–	–	–	–	–	5.87	11.0	20.0

Figures 4.3 and 4.4 display two plots for each target[9]. The (a) plots shows the efficiency, color-coded, for each cell : $e(f, \dot{f})$. The green curve in the efficiency plots shows $\dot{f}^{\star}$ as a function of f. The "stripes" at certain frequencies (e.g. around 350 Hz) are due to the instrumental lines of detectors at where the sensitivities are not good [30]. The (b) plots display the cells selected by the optimisation procedure to be searched within the computational budget, i.e. the coverage that we can afford. It is interesting to note how the shape of the covered parameter space changes as the source distance increases. As the distance decreases the detection probability per cell P_c increases, but it does so more slowly as the distance decreases because the probability cannot exceed 1. Below $\dot{f}^{\star}$, cells with higher $\dot{f}$ have a higher detection probability through the maximum allowed h_0 in Equation (6.2). However higher spindown also means larger computational cost due to the broader range in $\ddot{f}$. So, for the farther away sources like Cas A, the gain in detection probability offsets the computational cost. However for sources which are closer, and for which the gain is smaller, this is not the case. This is the reason why in, say, Figure 4.4 more cells are picked from high $\dot{f}$ regions than for Figure 4.3. In general, given fixed-duration coherent segment, selected cells in farther source (Cas A) are more likely from higher $\dot{f}$ region.

Optimizing with respect to search set-ups and targets

I now vary the possible search set-ups and also optimize over these. Again for illustration I consider seven representative choices of coherent segment lengths: 5, 10, 20, 30, 37.5, 50 and 75 days. As before, the total observation time is 300 days. I present results for the 3 sources Vela Jr (at 200 pc), G347.3 and Cas A.

A plot of the optimal detection probability as a function of the set-up is shown in Figure 4.2(b), the non-solid lines. For Vela Jr, the 20-day segment gives us the best result where the detection probability $\mathcal{R}$ is 8.98×10^{-3}.

Figure 4.5 shows the efficiency and the parameter space region that would be searched having

---

[9]Similar figures for other sources are shown in Figures 1 to 3 in Ref. [29].
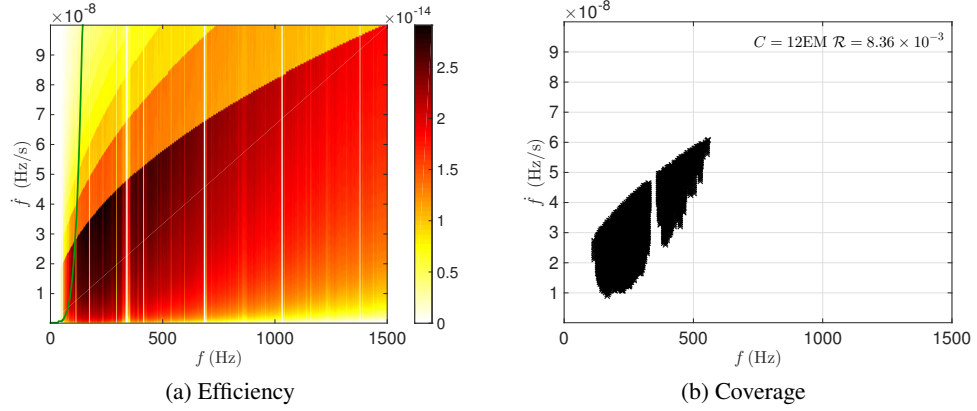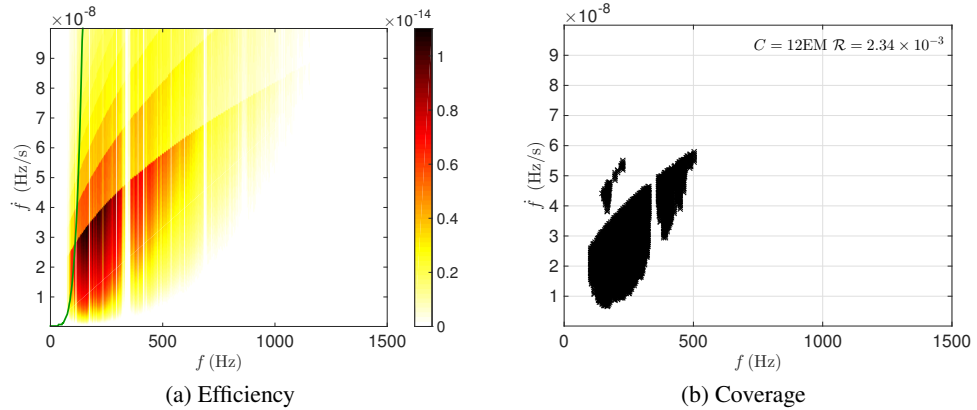
(a) Efficiency

(b) Coverage

Figure 4.3: Optimisation results for Vela Jr at 200 pc, assuming uniform and distance-based priors, and a 10-day coherent segment duration. The left plot shows the efficiency, color-coded, for each cell : $e(f, \dot{f})$. The green curve shows $\dot{f}^\star$ as a function of f. The origin of the strips at certain frequencies is due to the instrumental effects of LIGO detectors. The right plot displays the cells selected by the optimisation procedure with a computational budget of 12 EM. The detection probability $\mathcal{R}$ is 8.36×10^{-3}.

(a) Efficiency

(b) Coverage

Figure 4.4: Cas A at 3500 pc, assuming uniform and distance-based priors, and a 10-day coherent segment duration. The left plot shows the efficiency, color-coded, for each cell : $e(f, \dot{f})$. The green curve shows $\dot{f}^\star$ as a function of f. The right plot displays the cells selected by the optimisation procedure to be searched with a computational budget 12 EM. The detection probability $\mathcal{R}$ is 2.34×10^{-3}.

optimized separately for every different set-up[10]. This plot shows that longer coherent segment lengths disfavour very high values of $\dot{f}$ because the computing power grows more rapidly with increasing $\dot{f}$ than the gain in detection probability due to the larger range in $\ddot{f}$.

Using LP and optimizing also with respect to search set-ups I obtain the results shown in Figure 4.6 for Vela Jr and Figure 4.7 for Cas A. For illustration purposes I investigate different computing budgets: 12 EM and 24 EM[11].

I note three points from these results:

- For all the targets considered, doubling the computing cost increases the detection probability $\mathcal{R}$ by a factor of about 1.8 which means that the probability associated with the cells searched with the additional 12 EM is comparable with that associated to the cells searched by the first 12 EM.

- Optimizing with respect to the set-up yields a higher $\mathcal{R}$ as compared to a fixed set-up. However this gain is relatively small when compared to the set-up that by itself gave the highest detection probability, as it is illustrated in Figure 4.2(b). There the solid lines show the detection probability attainable by combining different set-ups for every target and the non-continuous line show the detection probability optimized at fixed set-up. For example, the $\mathcal{R}$ for Vela Jr. with the 20-day set-up is 8.98×10^{-3} and it grows to 9.17×10^{-3} by combining different set-ups; G347.3 similarly increases from 4.36×10^{-3} to 4.57×10^{-3} and Cas A from 2.34×10^{-3} to 2.44×10^{-3}.

- When optimizing for each target also with respect to set-up, the cells selected for Cas A's cells include the 5-day set-up (Figure 4.7), unlike for the other targets. The reason is that Cas A is the farthest of the considered targets and hence I gain more detection probability by searching higher spindowns, which in turn means higher maximum h_0 and hence higher detection probability, than by including more high-frequency cells. The cost of the high-spindown regions is higher than that of lower spindown ones and this is compensated by the optimisation procedure by using a shorter time-baseline set-up.

Since my goal is to optimize the probability of making a detection from *any* source, I do not want to restrict ourselves *a priori* to a particular source, and hence I optimize now also with respect to the targets.

Since the distance to Vela Jr is uncertain I consider two sets of three targets: Vela Jr at 200 pc and at 750 pc, G347.3 and IC 443. I will show results for 12EM, 24EM and 48EM computing budget $C_{\max}$. In Figure 4.8, when Vela Jr is assumed at 200 pc, even when $C_{\max} = 48$ EM, all the picked cells are from Vela Jr. This is because Vela Jr is so much closer to us than the others that the detection probability is maximized by always targeting Vela Jr. Thus, if I really believe that Vela Jr is 200 pc away, then I should concentrate all the computing budget on it. If in the optimisation process I assume that Vela Jr is 750 pc away, then the result changes. With a 12 EM budget, cells both from Vela Jr and G347.3 are picked. If I double the budget, some cells from IC 443 become worth searching and

---

[10]Similar figures for source G347.3 and Cas A are shown in Figures 4 and 5 in Ref. [29].

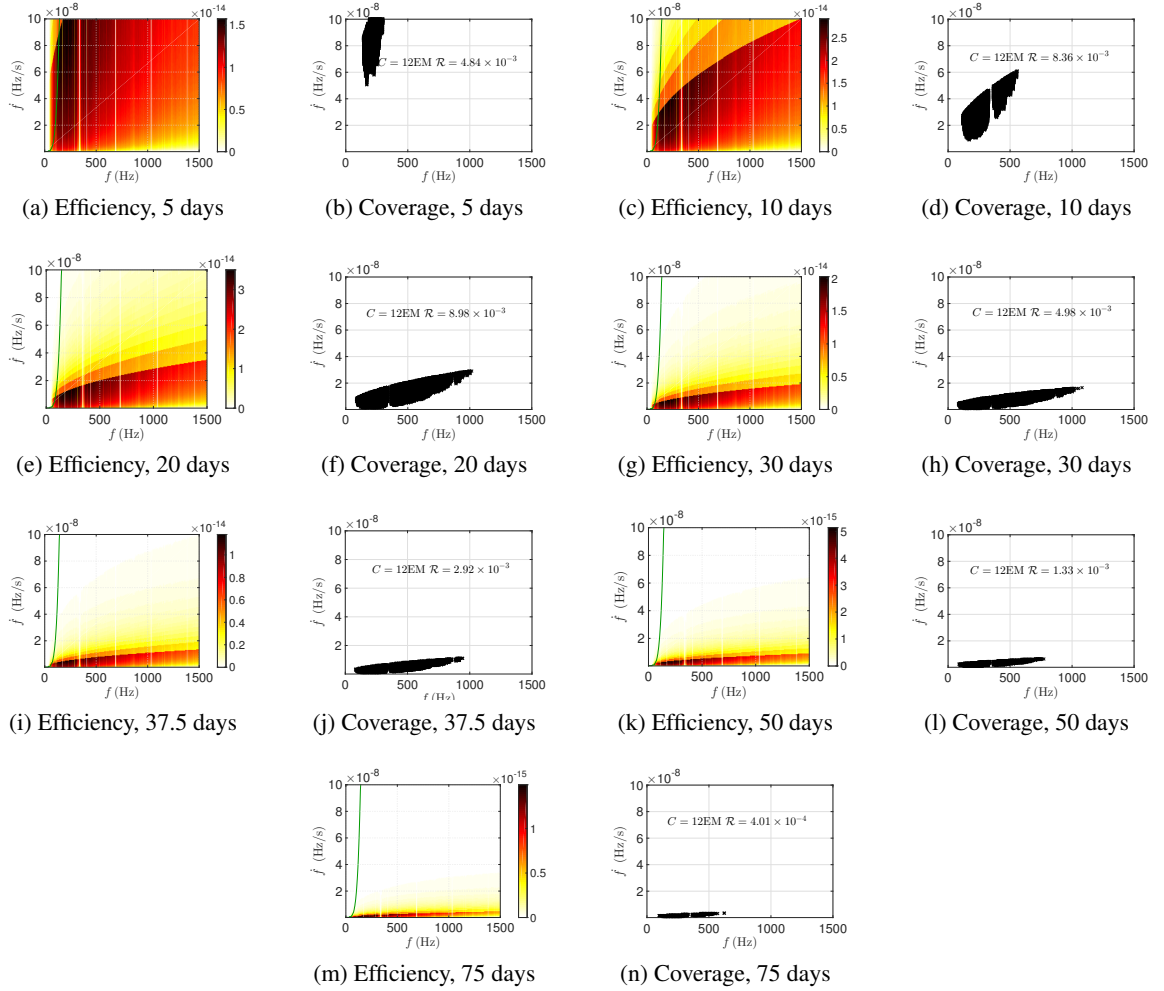[11]LP results for G347.3 are shown in Figure 6 in Ref. [29].

Figure 4.5: Optimisation results for Vela Jr at 200 pc, assuming uniform and distance-based priors, for various coherent search durations: 5, 10, 20, 30, 37.5, 50 and 75 days. The total computing budget is assumed to be 12 EM.

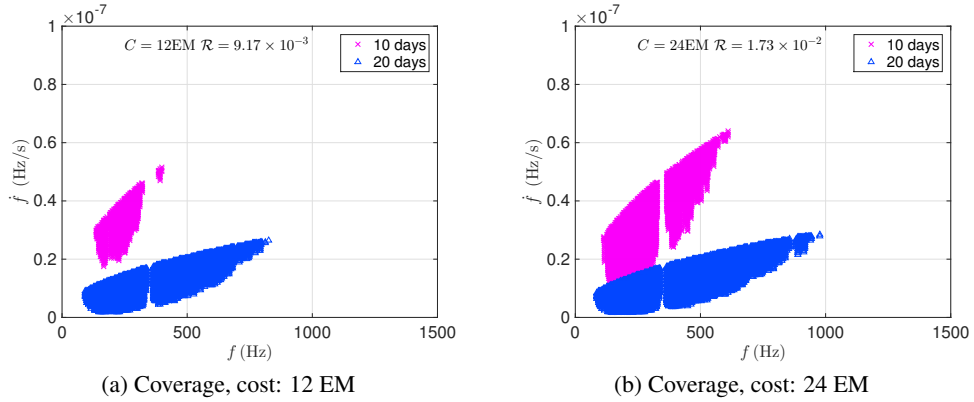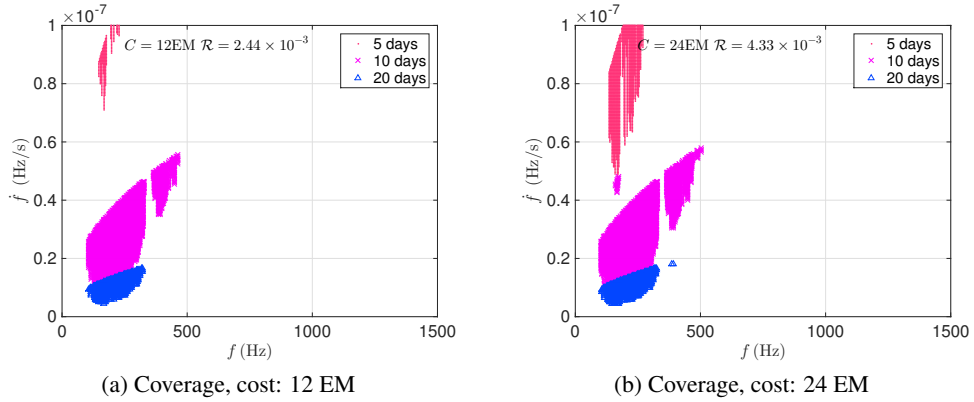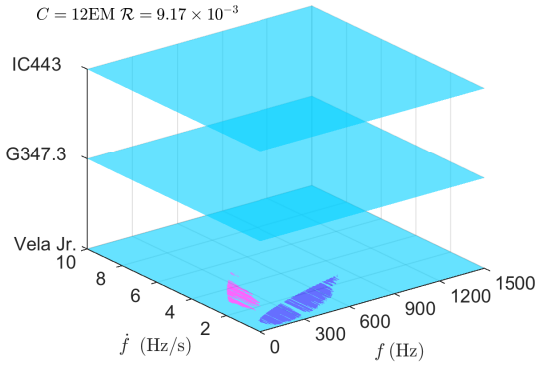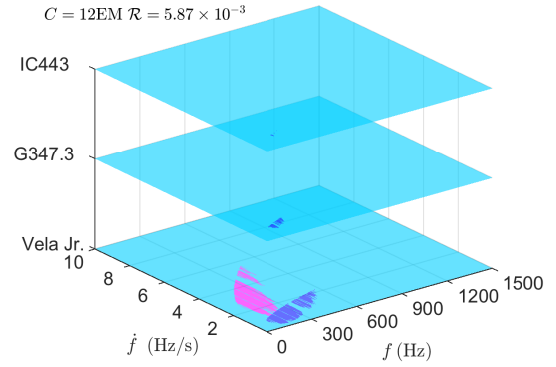(a) Coverage, cost: 12 EM   (b) Coverage, cost: 24 EM

Figure 4.6: Parameter space coverage for Vela Jr at 200 pc, assuming uniform and distance-based priors and optimizing over the 7 search set-ups also considered above at 12 EM (left plot) and 24 EM (right plot).
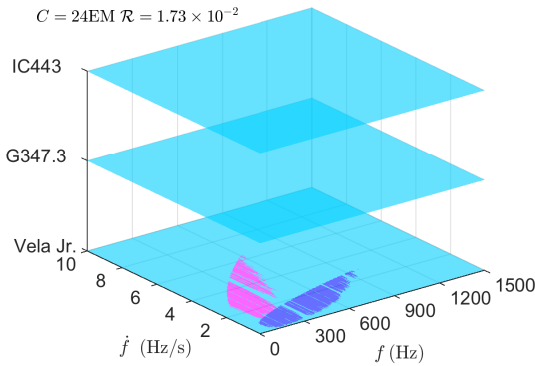

(a) Coverage, cost: 12 EM   (b) Coverage, cost: 24 EM

Figure 4.7: Parameter space coverage for Cas A at 3500 pc, assuming uniform and distance-based priors and optimizing over the 7 search set-ups also considered above at 12 EM (left plot) and 24 EM (right plot).

(a) Coverage of 3 sources, Vela Jr at 200 pc, computing budget 12EM

(b) Coverage of 3 sources, Vela Jr at 750 pc, computing budget 12EM

(c) Coverage of 3 sources, Vela Jr at 200 pc, computing budget 24 EM
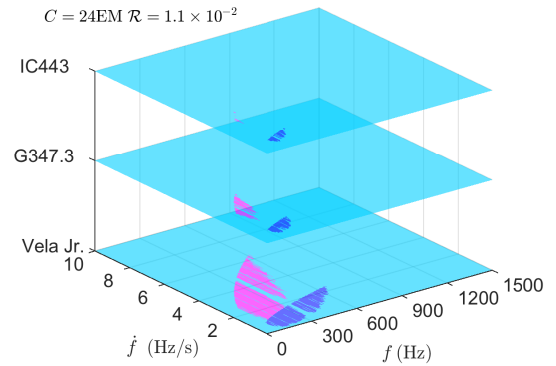
(d) Coverage of 3 sources, Vela Jr at 750 pc, computing budget 24 EM
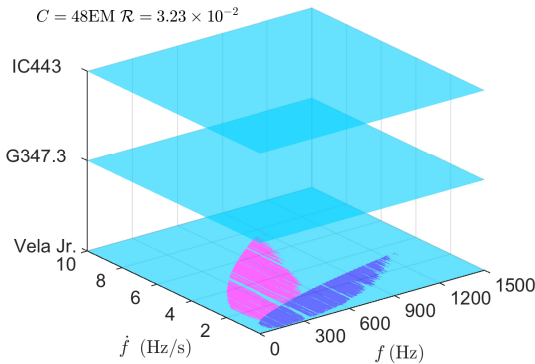
(e) Coverage of 3 sources, Vela Jr at 200 pc, computing budget 48 EM
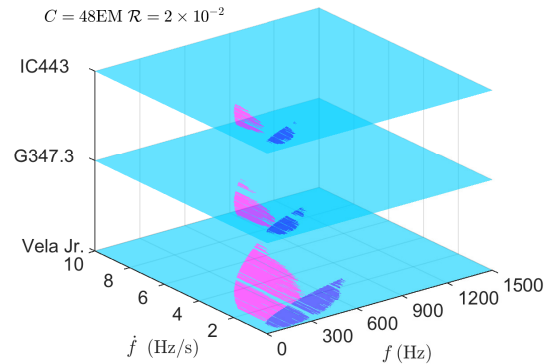
(f) Coverage of 3 sources, Vela Jr at 750 pc, computing budget 48 EM

Figure 4.8: Parameter space coverage assuming uniform and distance-based priors and optimizing over the 7 search set-ups also considered above and over the three closest targets (left plots: Vela Jr at 200 pc, G347.3, IC443 and right plots: Vela Jr at 750 pc, G347.3, IC443) at 12, 24 and 48 EMs.

Table 4.3: $\mathcal{R}$ result with f and $\dot{f}$ uniform priors and age-based priors. The highest $\mathcal{R}$ with respect to set-up is in bold font.

Name	D_{kpc}	τ_{kyr}	$10^3\mathcal{R}$									
			5D	10D	20D	30D	37.5D	50D	75D	LP Optimized		
					Computing Budget: 12EM					12EM	24EM	48EM
Cas A	3.5	0.35	1.22	**2.26**	1.38	0.446	0.164	0.036	0.003	2.26	3.32	–
G350.1	4.5	0.9	0.142	0.303	0.480	**0.569**	0.474	0.187	0.027	0.559	0.640	–
G347.3	1.3	1.6	3.45	5.78	**7.89**	7.16	4.34	1.89	0.330	8.27	9.89	–
Vela Jr	0.2	0.7	10.2	**19.7**	17.7	6.62	3.03	0.850	0.097	21.6	38.8	–
Vela Jr	0.2	4.3	33.2	56.7	**67.1**(11.3EM)	56.2	38.5	20.3	5.35	–	–	–
Vela Jr	0.75	4.3	5.75	7.76	9.66(11.3EM)	**11.2**	11.0	7.96	2.55	11.6	13.0	–
Top 3 (CY)	–	–	–	–	–	–	–	–	–	21.6	38.8	69.8
Top 3 (FO)	–	–	–	–	–	–	–	–	–	11.7	14.1	16.6

this effect becomes even more prominent if I quadruple the budget. However, even at $C_{\mathrm{max}} = 48$ EM most of the searched parameter space targets Vela Jr. Table 4.2 lists the $\mathcal{R}$ numbers and Figure 4.2(c) diplays them as a function of C_{max}. Note that the highest $\mathcal{R}$ with respect to set-up is in bold font.

Results with age-based priors

I illustrate the results of the optimisation when using the priors of Equation (4.20) that fold in the information on the age of the target. Figure 4.10 in this subsection shows the color-coded P_{D}-maps and the selected parameter space to target with a 12 EM computing budget allocated to the closest target Vela Jr. Because of the uncertainty in the age and the distance of Vela Jr, I have investigated the two extreme scenarios: a close and young Vela Jr (CY) and an far and old Vela Jr (FO). Other three sources Cas A (youngest), G347.3 and G350.1 (close and young) are also investigated (see Figure 7 to 10 in Ref. [29]). As done in the previous section I also optimize the search with respect to set-ups and further with respect to targets. The complete set of results is summarized in Table 4.3 and Figure 4.9. I note the following:

- The younger the target, the steeper is the slope that determines the prior $f - \dot{f}$ volume. This means that for younger targets higher values of $\dot{f}$ are allowed. At the same distance and frequency, more detection probability can be accumulated at higher $\dot{f}$ values because of the higher limit in h_0.

- However, even when optimizing separately for every target the main factor that determines the detection probability at fixed computing cost is the distance. This is summarized in Figure 4.9(a).

- For the eldest target, Vela Jr with $\tau_{\mathrm{c}} = 4300$ yrs shown in Figure 4.10, the prior $f - \dot{f}$ volume is small enough that with the 20-day set-up I do not exhaust the available computing budget. For shorter coherent time-baselines the computational cost is dominated by the incoherent step. As
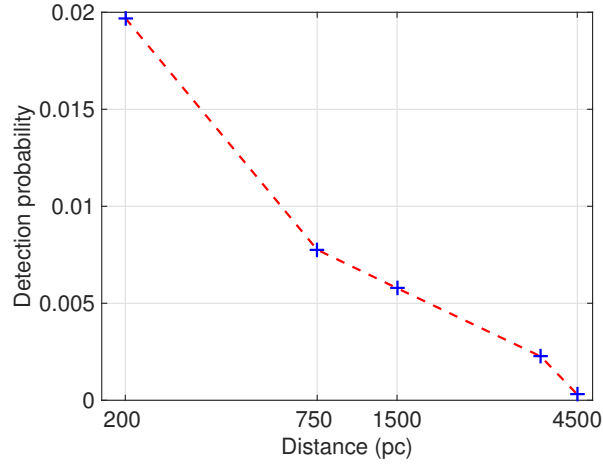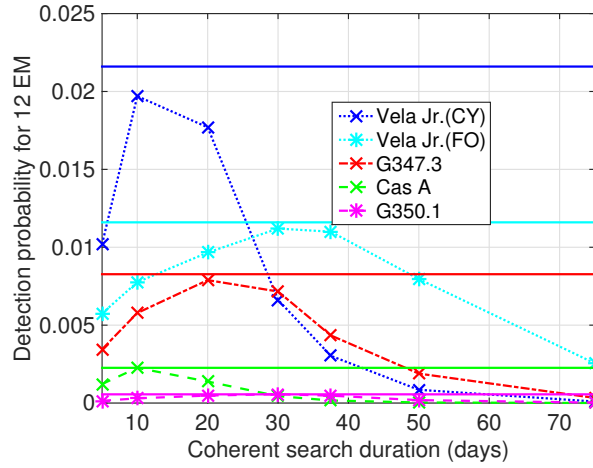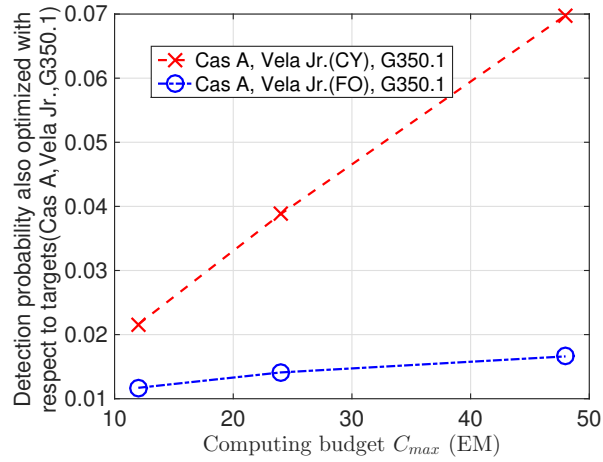
(a) $\mathcal{R}$ versus distance

(b) $\mathcal{R}$ versus T_{coh}

(c) $\mathcal{R}$ versus C_{max}

Figure 4.9: Detection probability for various targets and search set-ups having assumed uniform and age-based priors. The distances that were assumed for the targets are: Vela Jr (C) 200 pc, Vela Jr (F) 750 pc, G 347.3 1.3 kpc, Cas A 3.5 kpc, G350.1 4.5 kpc.

the coherent time-baseline increases the cost of the incoherent sum decreases because there are fewer segments to sum while the cost of coherent step increases rapidly, shifting the balance.

- Unlike in the case where I do not fold in the age information, doubling the computing budget does not bring a significant gain in detection probability. The reason is that the parameter space that is available for searching extends just to higher frequencies, not to higher spindowns, and there the sensitivity is lower and hence the increase in detection probability is marginal.

- For the older sources the optimal search set-ups with age-based priors favour longer segment durations than those found with distance-based priors because their parameter space is limited to lower $\dot{f}$ regions.

I now optimize also with respect to sources. Figure 4.12 shows that the covered parameter space increases as computing cost increases. I note the following:

- At 12 EM the preferred target is Vela Jr solely, if I assume that it is CY. The cells picked by the optimisation procedure are obviously the same as the cells picked in the Figure 4.11(a), corresponding to 10 and 20-day set-ups that gave the highest $\mathcal{R} = 2.16 \times 10^{-2}$.

- If instead I assume that Vela Jr is FO then, at 12 EM, the detection probability is maximized by spending some fraction of the computing budget also on G350.1 and Cas A 54% of the prior parameter space of Vela Jr FO is searched leaving out high f - low $\dot{f}$ cells which have a low detection probability. Again the optimal set-up is a combination of the 20, 30 and 37.5-day set-ups which yield the top three $\mathcal{R}$ in the fixed-set-up optimisation, cfr. Figures 4.10(f), (h) and (j). 10.2 EM (84.9% of total) were spent to accumulate 1.12×10^{-2} (95.3%) detection probability from Vela Jr FO and 1.8 EM (15.1%) were spent to accumulate 5.48×10^{-4} (4.7%) detection probability jointly from G350.1 and Cas A. So one could say that the Vela Jr FO searched cells are, on average, a factor of 3.57 more efficient at accumulating detection probability per computing cost unit than the cells of the other two targets. The set-ups for the cells picked for Cas A are the same as those picked when optimizing with respect to set-up for Cas A only, cfr. Figure 4.13. This is not the case for G350.1: for the selected cells it turns out that it is more efficient to use the small computational budget on more cells with a shorter coherent time-baseline, than with a longer coherent baseline as when optimizing the 12 EM for G350.1 alone, cfr. Figure 4.14.

- 24 EM buys more parameter space cells for Vela Jr CY, nearly doubling the detection probability with respect to the 12 EM case: from 2.16×10^{-2} to 3.88×10^{-2}.

- Under the assumption that Vela Jr is FO, the additional 12 EM (total 24 EM) only increase the detection probability by less than 21%: from 1.17×10^{-2} to 1.41×10^{-2}. This is reasonable: I know in fact that if I had 12 EM to spend just on Cas A the maximum probability that I could achieve is 2.26×10^{-3} and on G350.1 it is 5.59×10^{-4}. So if I had an additional 24EM to spend, at most I could achieve an increase in detection probability of 2.82×10^{-3} which amounts to 24% of the 1.17×10^{-2}. With half of that computing power I achieve just over half of this

(a) Efficiency, 5 days (b) Coverage, 5 days (c) Efficiency, 10 days (d) Coverage, 10 days

(e) Efficiency, 20 days (f) Coverage, 20 days (g) Efficiency, 30 days (h) Coverage, 30 days

(i) Efficiency, 37.5 days (j) Coverage, 37.5 days (k) Efficiency, 50 days (l) Coverage, 50 days
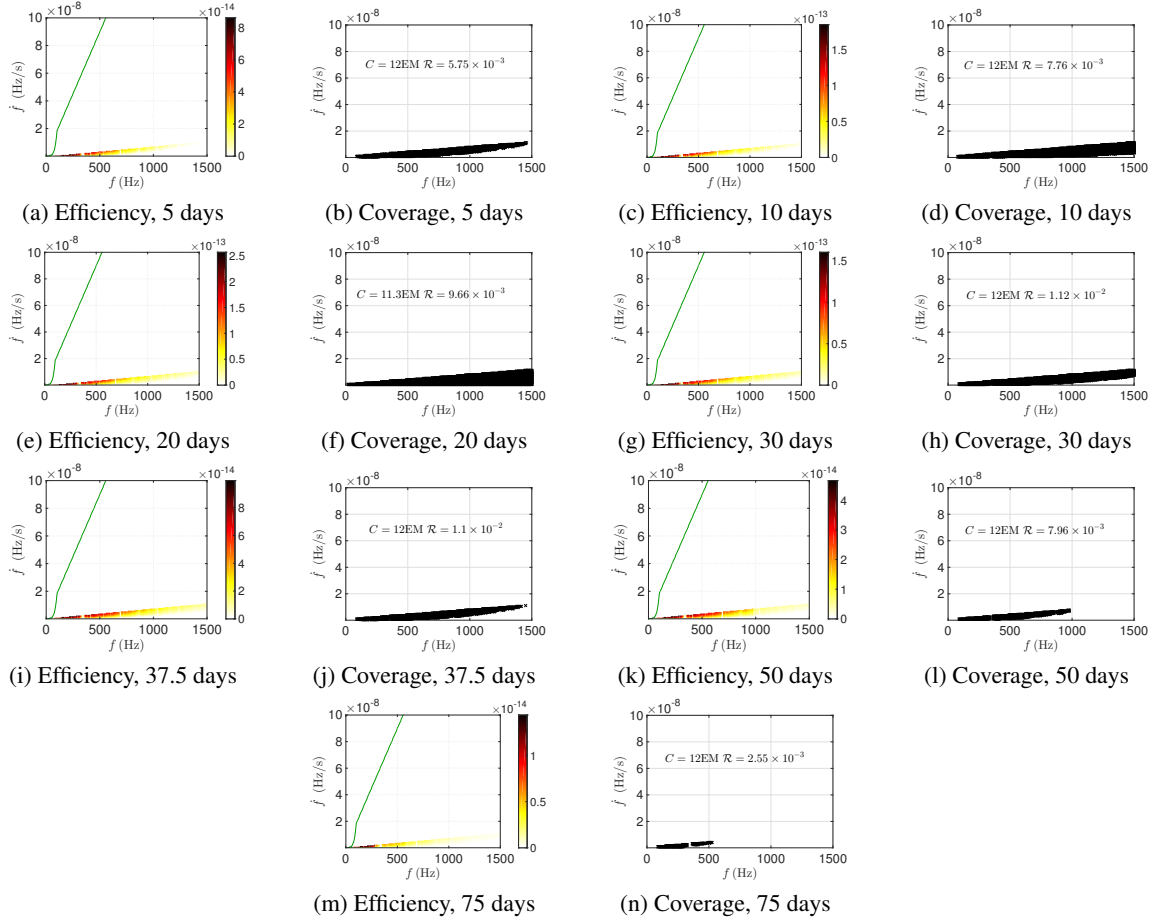
(m) Efficiency, 75 days (n) Coverage, 75 days

Figure 4.10: Optimisation results for Vela Jr at 750 pc and 4300 years old, assuming uniform and age-based priors, for various coherent search durations: 5, 10, 20, 30, 37.5, 50 and 75 days. The total computing budget assumed is 12EM.

(a) Coverage, cost: 12 EM   (b) Coverage, cost: 24 EM
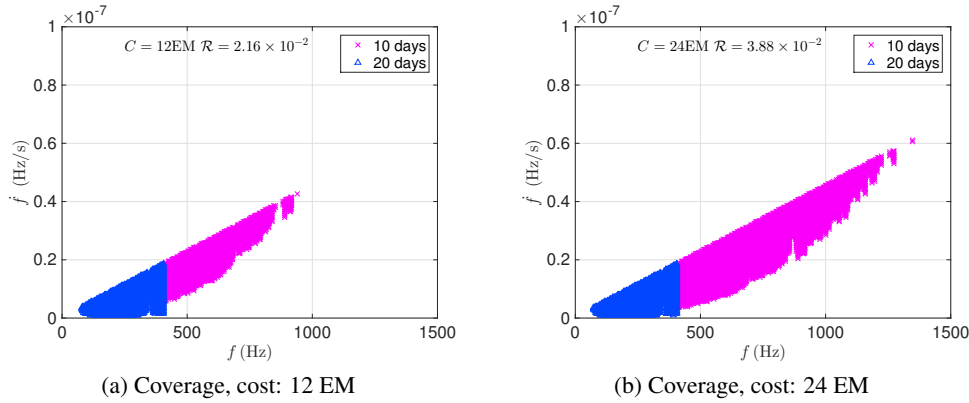
Figure 4.11: Parameter space coverage for Vela Jr at 200 pc, 700 years old, assuming uniform and age-based priors and optimizing over the 7 search set-ups also considered above at 12 EM (left plot) and 24 EM (right plot).

maximum gain. Regarding the set-ups picked for the different sources the same considerations hold as I made for the 12 EM case.

• With 48 EM more than half of the whole prior parameter space of Vela Jr CY is covered. With such a high amount of budget the highest sensitivity cells are still searched with the most efficient search set-up: 10 and 20-day. Detection probability is nearly doubled again and still no computing budget will be spent on Cas A and G350.1. This is because Vela Jr CY has larger parameter space in $\dot{f}$ and more computing power could be spent on those cells in the higher $\dot{f}$ region.

• Under the assumption that Vela Jr is FO, the additional 24 EM (total 48 EM) only increase the detection probability by less than 18%. Not only more cells from Cas A and G350.1 are searched, but also cells in Vela Jr trend to use longer coherent segments. This is because rather than to spend more computing power on the sources with less potential like Cas A and G350.1, it could be better to use more expense and also more efficient set-ups for Vela Jr.

Figure 4.15 shows how $\mathcal{R}$ and the used computing budget C vary with age, having assumed a search for Vela Jr. at 200 and 750 pc, a coherent time-baseline of 20 days and a computing budget $C_{\min}$ of 12 and 24 EM. In the young age region, C is always flat. That's because the older the object, the smaller is the prior $f - \dot{f}$ volume available for searching. Hence there is an age τ_{plat} at which the allocated $C_{\max}$ is large enough to just cover such a volume. For higher values of the age the prior space shrinks and less computing power is needed to cover it. For lower values of the age the prior volume is larger and the optimisation method will select what cells are the most promising to search while using up all the computational power, hence the plateau at low age values.

Let us now look at $\mathcal{R}$. In all these four cases, $\mathcal{R}$ has a maximum value $\mathcal{R}_{\mathrm{peak}}$ at a certain age τ_{peak}. A larger computing budget gives a higher $\mathcal{R}_{\mathrm{peak}}$ and this happens at a lower age. However τ_{peak} does
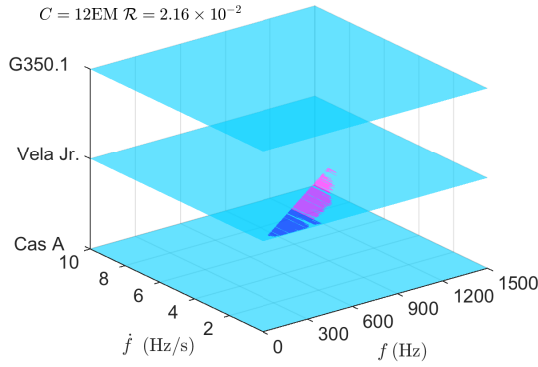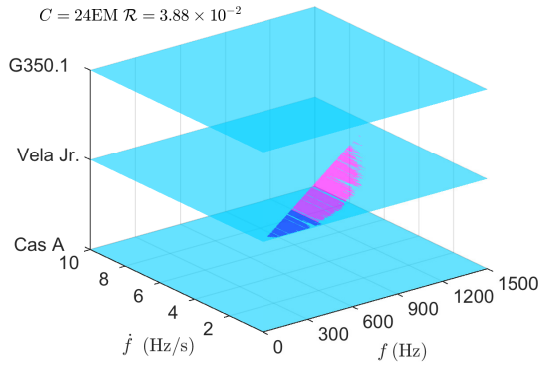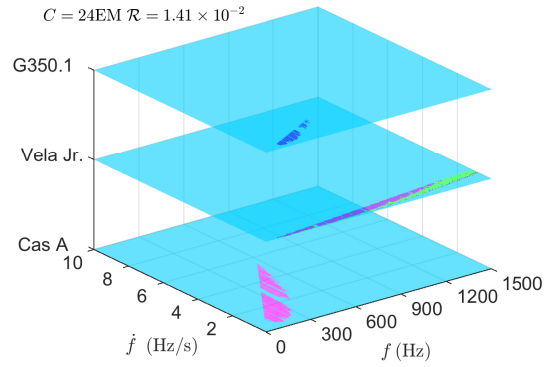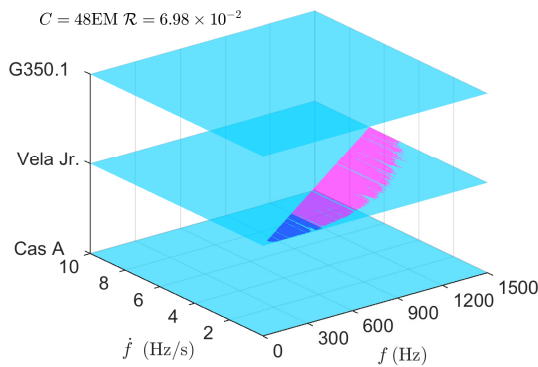
(a) Coverage of 3 sources, CY, Cost 12 EM
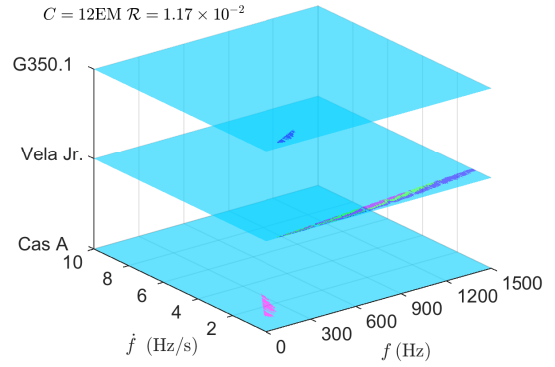
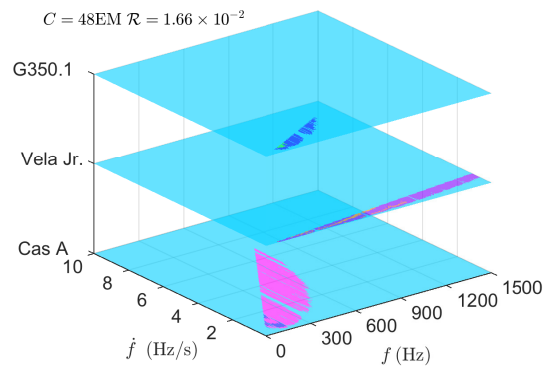(b) Coverage of 3 sources, FO, Cost 12 EM

(c) Coverage of 3 sources, CY, Cost 24 EM

(d) Coverage of 3 sources, FO, Cost 24 EM

(e) Coverage of 3 sources, CY, Cost 48 EM

(f) Coverage of 3 sources, FO, Cost 48 EM

Figure 4.12: Parameter space coverage assuming uniform and age-based priors and optimizing over the 7 search set-ups also considered above and over the three youngest targets (left plots: Cas A, Vela Jr at 200 pc and 700 years old (CY), G350.1 and right plots: Cas A, Vela Jr at 750 pc and 4300 years old (FO), G350.1) at 12, 24 and 48 EMs.
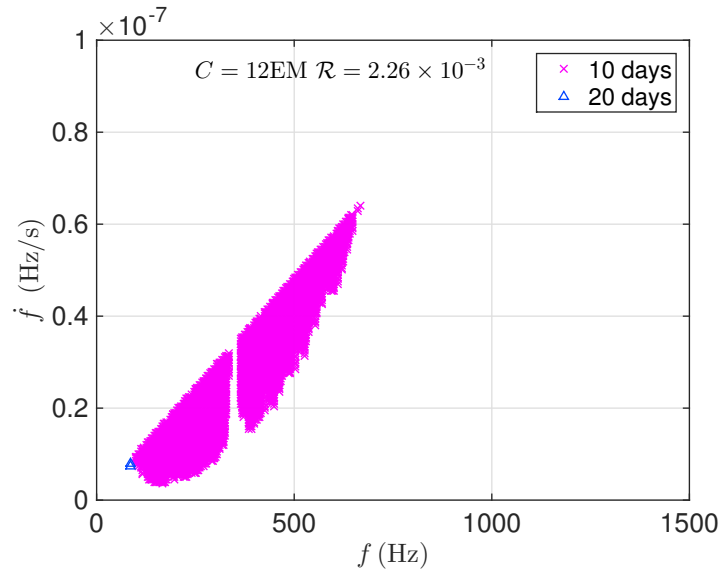
Figure 4.13: Parameter space coverage for Cas A at 3500 pc, 330 years old, assuming uniform and age-based priors and optimizing over the 7 search set-ups also considered above at 12 EM.
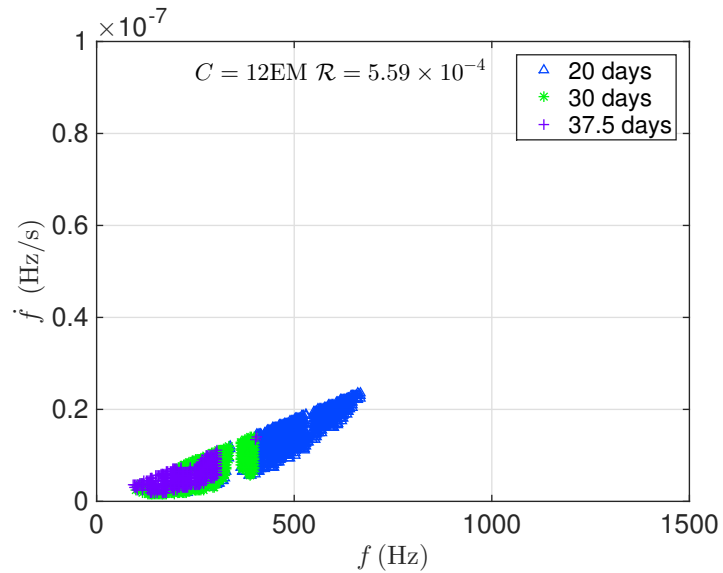

Figure 4.14: Parameter space coverage for G350.1 at 4500 pc, 900 years old, assuming uniform and age-based priors and optimizing over the 7 search set-ups also considered above at 12 EM.

(a) 0.2 kpc, 12 EM budget

(b) 0.75 kpc, 12 EM budget
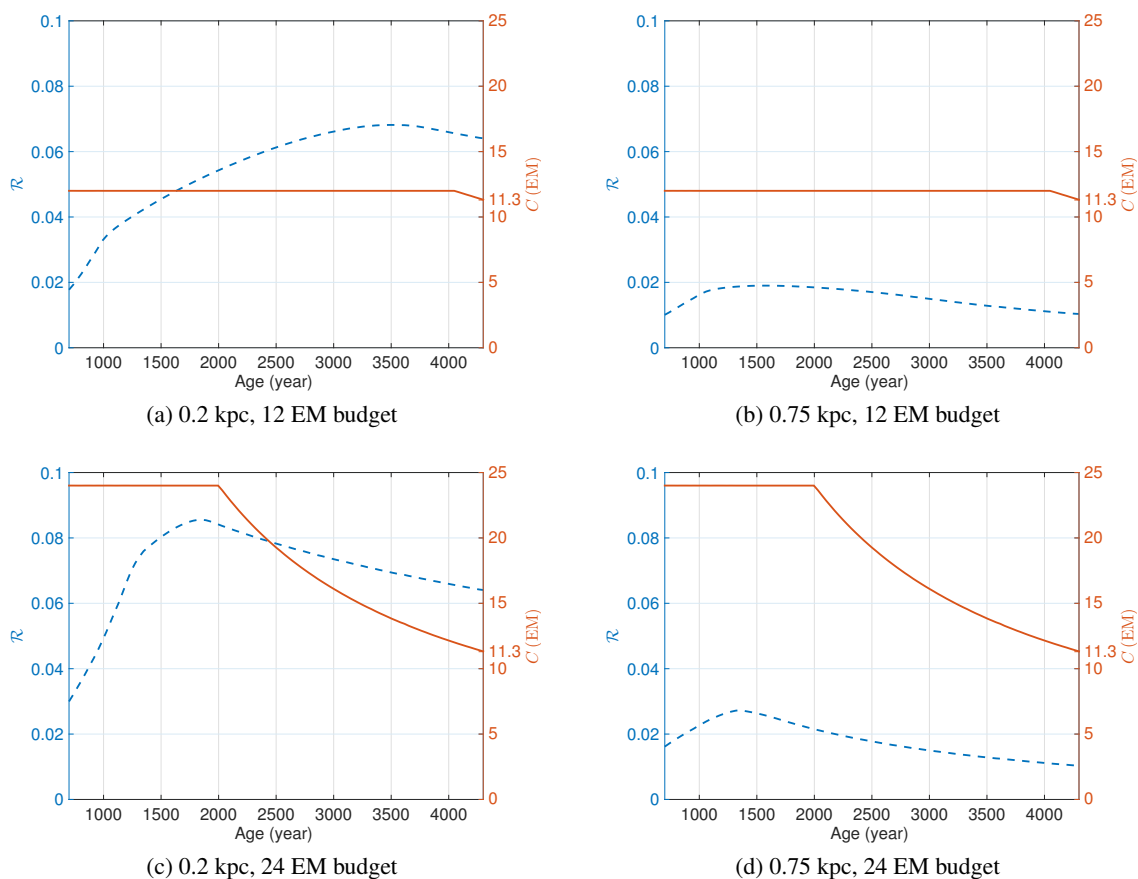
(c) 0.2 kpc, 24 EM budget

(d) 0.75 kpc, 24 EM budget

Figure 4.15: $\mathcal{R}$ and C as a function of age for an optimised search for Vela Jr, assuming uniform and age-based priors, a computing budget of 12 and 24 EMs and a 20-day coherent segment search set-up.

Table 4.4: $\mathcal{R}$ result with f and $\dot{f}$ log-uniform priors and distance-based priors. The highest $\mathcal{R}$ with respect to set-up is in bold font.

Name	D_kpc	5D	10D	20D	30D	37.5D	50D	75D	LP Optimized		
				Computing Budget: 12EM					12EM	24EM	48EM
Cas A	3.5	0.167	**0.278**	0.257	0.187	0.147	0.093	0.039	0.319	0.414	–
IC 443	1.5	0.418	0.669	**0.714**	0.560	0.481	0.341	0.189	0.804	0.991	–
G347.3	1.3	0.544	0.807	**0.820**	0.661	0.569	0.422	0.248	0.937	1.15	–
Vela Jr	0.2	2.97	3.91	**4.26**	3.94	3.54	3.06	2.34	4.51	5.16	–
Vela Jr	0.75	0.906	1.37	**1.47**	1.29	1.12	0.880	0.604	1.64	1.96	–
Top 3 (0.2 kpc)	–	–	–	–	–	–	–	–	4.96	5.92	6.95
Top 3 (0.75 kpc)	–	–	–	–	–	–	–	–	2.32	2.99	3.70

Table 4.5: $\mathcal{R}$ result with f and $\dot{f}$ log-uniform priors and age-based priors. The highest $\mathcal{R}$ with respect to set-up is in bold font.

| Name	D_kpc	τ_kyr	5D	10D	20D	30D	37.5D	50D	75D	LP Optimized		
					Computing Budget: 12EM					12EM	24EM	48EM
Cas A	3.5	0.35	0.960	1.38	**1.44**	0.821	0.347	0.091	0.008	1.56	1.81	–
G350.1	4.5	0.9	0.099	0.200	0.300	0.374	**0.414**	0.236	0.037	0.469	0.504	–
G347.3	1.3	1.6	2.13	2.83	3.52	**4.31**	3.73	3.30	1.22	4.50	4.75	–
Vela Jr	0.2	0.7	22.9	27.8	**29.9**	25.5	21.8	14.6	4.62	31.0	33.8	–
Vela Jr	0.2	4.3	26.9	31.5	36.4(11.3EM)	**36.6**	36.4	31.0	33.8	–	–	–
Vela Jr	0.75	4.3	3.84	4.93	5.90(11.3EM)	6.78	7.49	**7.80**	6.40	8.12	8.36	–
Top 3 (CY)	–	–	–	–	–	–	–	–	–	31.1	34.2	37.2
Top 3 (FO)	–	–	–	–	–	–	–	–	–	9.13	9.93	10.5

not coincide with τ_plat because even though as the age increases towards τ_plat the fractional covered volume of parameter space is increasing, at the same time the total volume is shrinking and the cells that are not any more included are actually the ones contributing the most to the detection probability. This is because the dropped cells are the higher spindown ones which have the highest amplitude cut-off value $h_{0\max}$.

## 4.4.2   Log-uniform priors in f and $\dot{f}$

I do not comment here on the findings with the same level of detail used in the previous section, as that was done in order to highlight the main factors contributing to the results[12]. Based on the material presented there, I am confident that the interested reader can do this himself/herself here. I highlight instead the following points:

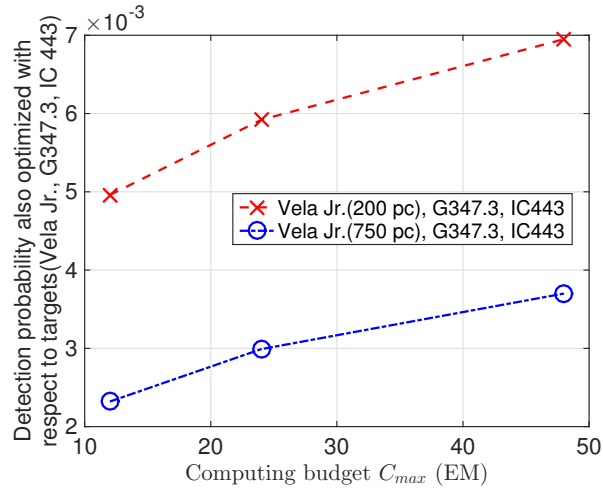[12] All results of assuming log-uniform prior are shown in Figures 14 to 28 in Ref. [29]
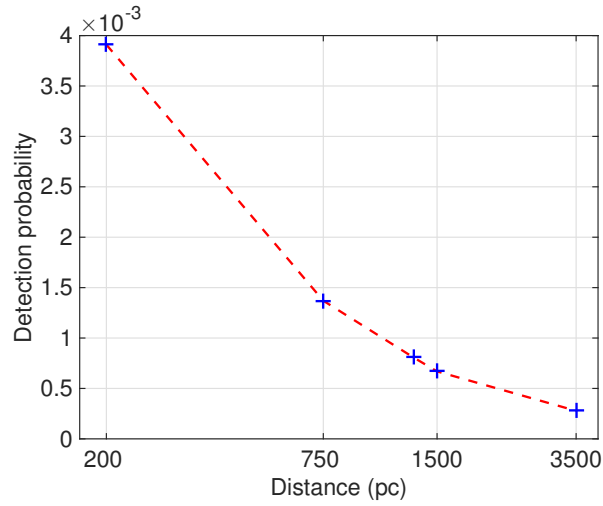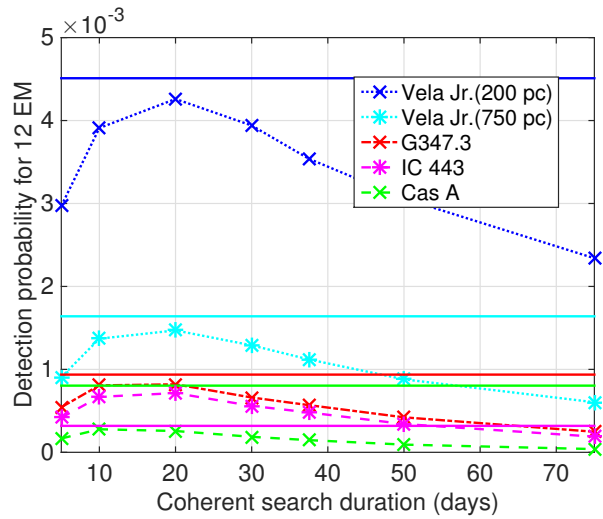
(a) $\mathcal{R}$ versus distance

(b) $\mathcal{R}$ versus T_{coh}

(c) $\mathcal{R}$ versus C_{max}

Figure 4.16: Detection probability for various targets and search set-ups having assumed log-uniform and distance-based priors. The distances that were assumed for the targets are: Vela Jr (C) 200 pc, Vela Jr (F) 750 pc, G 347.3 1.3 kpc, IC443 1.5kpc, Cas A 3.5 kpc.
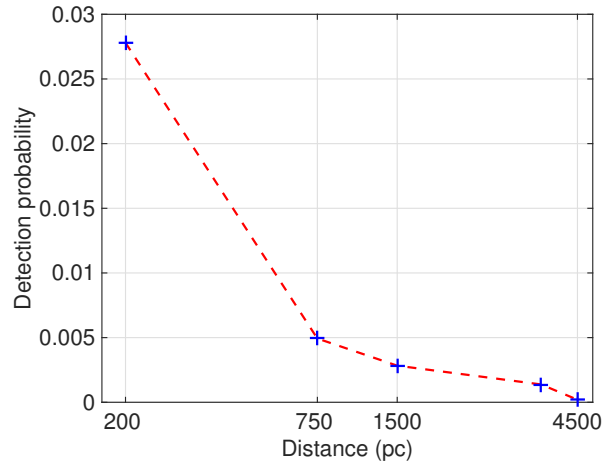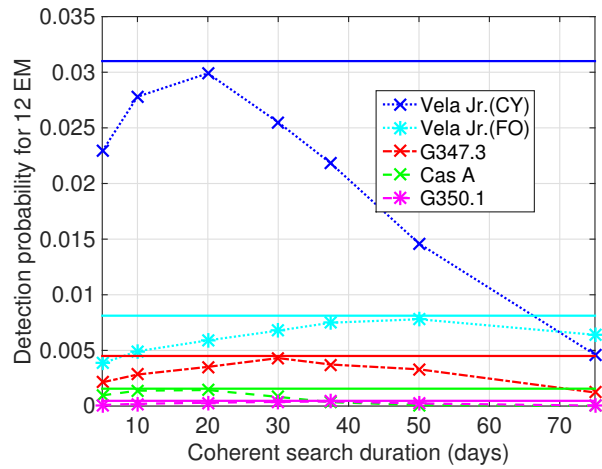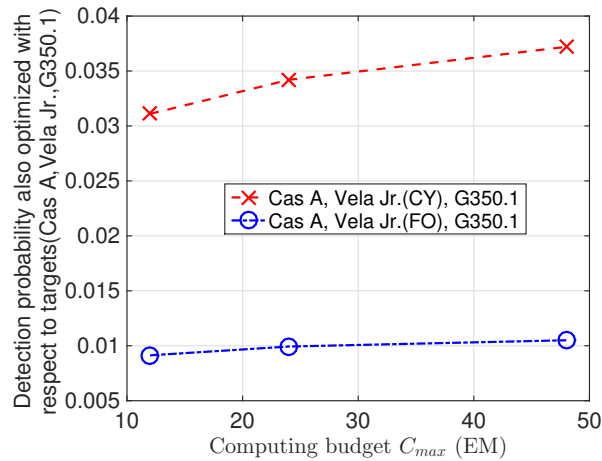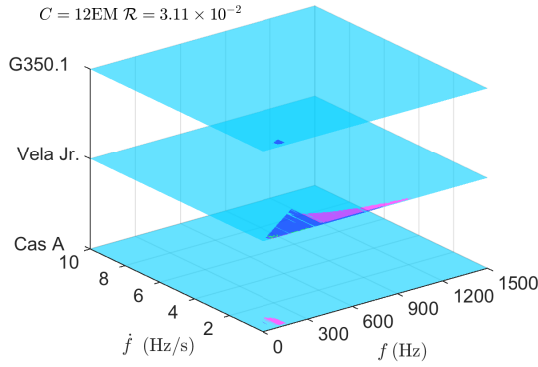
(a) $\mathcal{R}$ versus distance

(b) $\mathcal{R}$ versus T_{coh}

(c) $\mathcal{R}$ versus C_{max}

Figure 4.17: Detection probability for various targets and search set-ups having assumed log-uniform and age-based priors. The distances that were assumed for the targets are: Vela Jr (C) 200 pc, Vela Jr (F) 750 pc, G 347.3 1.3 kpc, Cas A 3.5 kpc, G350.1 4.5 kpc.

(a) Coverage of 3 sources, Cost 12 EM
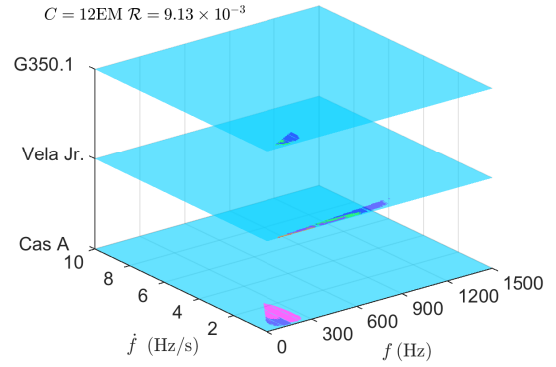
(b) Coverage of 3 sources, Cost 12 EM
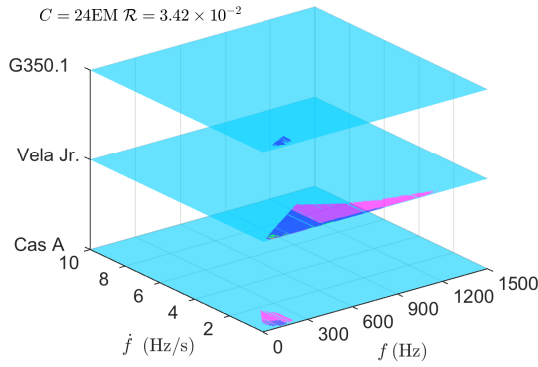
(c) Coverage of 3 sources, Cost 24 EM
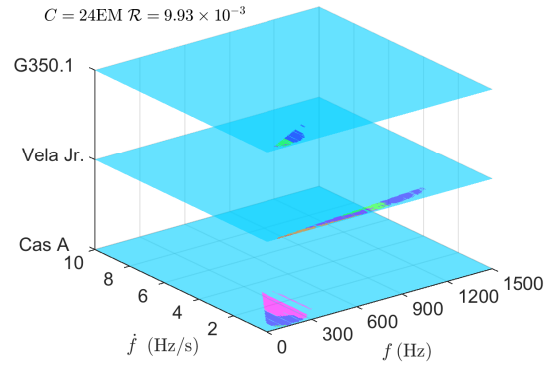
(d) Coverage of 3 sources, Cost 24 EM
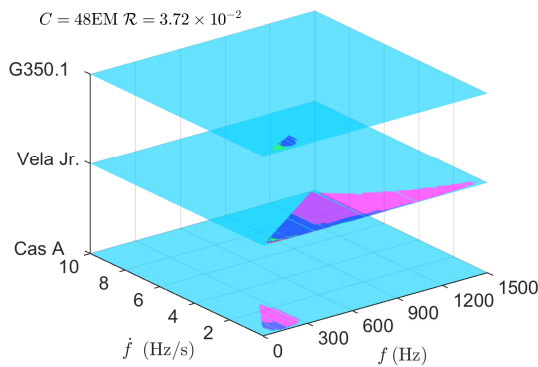
(e) Coverage of 3 sources, Cost 48 EM
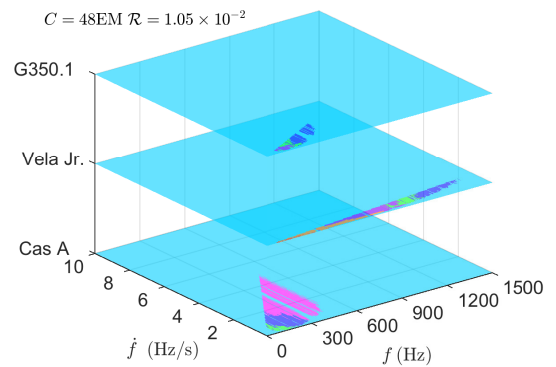
(f) Coverage of 3 sources, Cost 48 EM

Figure 4.18: Parameter space coverage assuming log-uniform and age-based priors and optimizing over the 7 search set-ups also considered above and over the three youngest targets (left plots: Cas A, Vela Jr at 200 pc and 700 years old (CY), G350.1 and right plots: Cas A, Vela Jr at 750 pc and 4300 years old (FO), G350.1) at 12, 24 and 48 EMs.

(a) 0.2 kpc, 12 EM budget

(b) 0.75 kpc, 12 EM budget

(c) 0.2 kpc, 24 EM budget

(d) 0.75 kpc, 24 EM budget

Figure 4.19: $\mathcal{R}$ and C as a function of age for an optimised search for Vela Jr, assuming log-uniform and age-based priors, a computing budget of 12 and 24 EMs and a 20-day coherent segment search set-up.

- The log-uniform priors favour lower frequency and lower spindown values with respect to the uniform priors.

- Generally when assuming distance-based priors, this decreases the detection probability because the computing power is more eagerly invested in searching for signals with lower spindowns which typically have smaller maximum amplitudes (through Equations (4.13) and (5.8)). I note about a factor 2-7.6 decrease across the board.
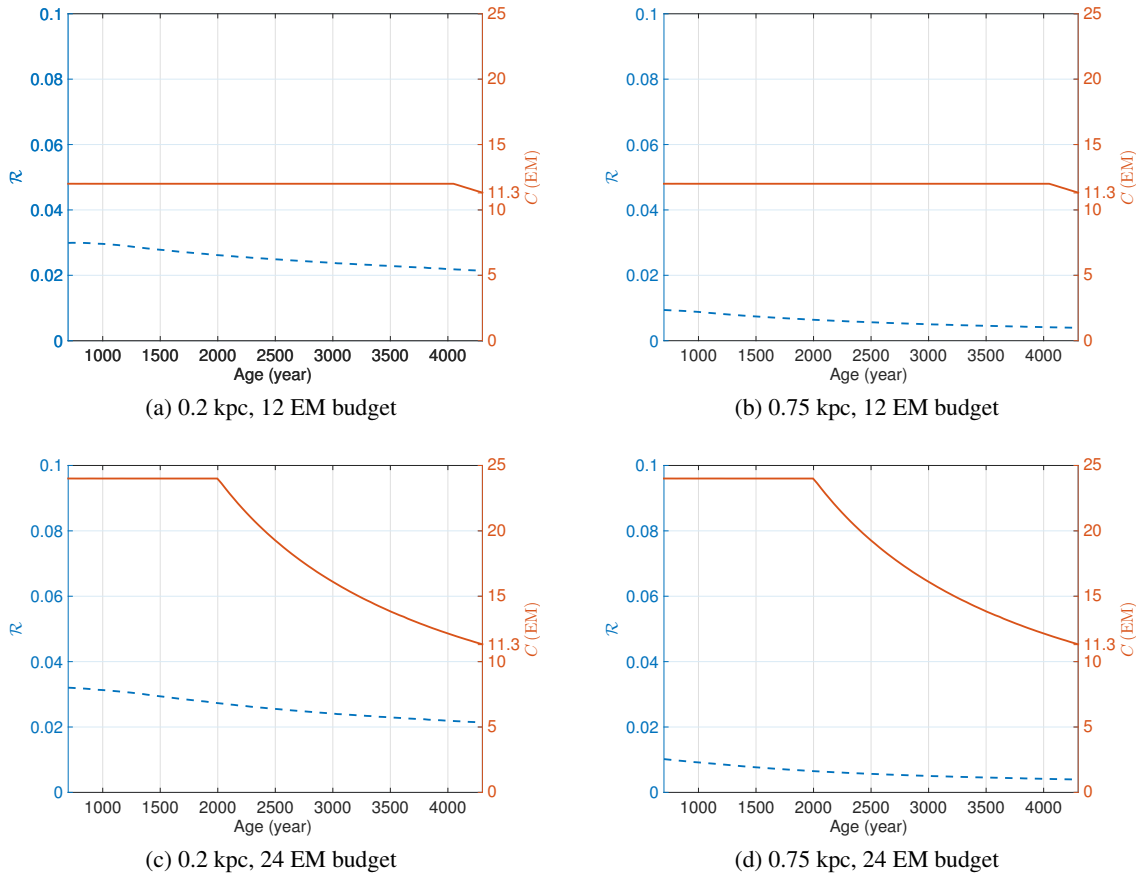
- This is not strictly true when assuming age-based priors in fact for Vela Jr (CY) the detection probability at 12 EM increases from 2.16% (uniform and age-based) to 3.10% (log-uniform and age-based). For all the other sources the detection probability decreases but not as much as in the distance-based case.

- At fixed source, the optimisation scheme prescribes segment lengths which are higher with respect to those of the uniform-priors searches. The reason for this is that longer duration segments can be more easily afforded at lower $\dot{f}$ regions, where the $\ddot{f}$ costs are lower.

- The prescription for the parameter volumes to search is quite different: this is evident for all sources and set-ups. For example from the 3D plots shown in Figures 4.12 and 4.18 I see how markedly the log-uniform priors disfavour high $f - \dot{f}$ combinations with respect to the uniform priors.

- Figure 4.19 shows how $\mathcal{R}$ and C vary with age. The cost curve is the same as the cost curve of Figure 4.15. This is quite obvious because the f and $\dot{f}$ log-uniform prior does not change the computing cost in each cell. However the log-uniform prior has a large influence on the detection probability: the τ_{peak} is 700 years, the smallest. The reason is that the contribution to the detection probability from higher spindown cells that are excluded with respect to the uniform-prior case, is not compensated for by the higher fractional volume of searched parameter space. This means, for log-uniform priors, for the sources with the same distance, "The younger, the better".

4.5 Conclusions

Searches for continuous GWs, even the directed ones from sources with known sky-positions, are computationally limited and decisions regarding the parameter space, search set-up and the astrophysical target can make the difference between making or missing a detection. I have described and implemented an optimisation scheme with the goal of maximizing the detection probability constrained by a limited computing budget. Specifically, I have addressed the following questions:

- On which target(s) should we spend our computing resources?

- What parameter space region in frequency and spindown should we search?

- What is the optimal search set-up that we should use?

- What is the probability of making a detection, given prior assumptions on the signal parameters?

The crucial step in the procedure is that of choosing the priors on the frequency, spindown and ellipticity of the source. I choose the broadest range of plausible values under combinations of two different assumptions: namely using or not the information on the age of the object (age-based priors) and using uniform priors or log-uniform priors for the frequency and frequency derivative. The uniform priors are useful to illustrate the method. The log-uniform priors are more realistic. With these I find the following:

- Distance-based priors yield detection probabilities on average a factor of 4 smaller when used in conjunction with log-uniform priors than when used in conjunction with uniform priors. For age-based priors this difference is no more than a factor of two.

- The highest detection probability for a search at the LIGO S6 run sensitivity level, using about a year of data from two detectors with a duty factor of 50% and assuming a computing budget of 12 EM, is 6.7%. This is obtained under the assumption that Vela Jr is old, 200 pc away, a uniform distribution for f and $\dot{f}$, an age-based prior, and assuming that these priors reflect reality. If the f and $\dot{f}$ are instead log-uniformly distributed and I match the priors to this assumption, the detection probability drops to 3.6%.

- The optimisation over set-up for every cell in parameter space yields at most 15% increase in detection probability with respect to single set-up search. Given the complexity of setting up and analysing the results of a search that uses different segment lengths for different areas of parameter space, this result is relevant because it indicates that using a single set-up or at most two (a practical solution), does not significantly impact the chances of making a detection.

- Independently of all prior assumptions, all optimal searches cover the broadest fraction of the prior spin down range around the instruments' maximum sensitivity frequencies.

In forthcoming work I will investigate different priors, consider a range of search set-ups including different mismatch parameters, grids, number of segments and segment durations, and optimise over all these. I will fold in the mismatch distribution arising from the choices of nominal mismatch values and of the grids, and not only work with the expected values as done here. Furthermore here I have not considered any uncertainty on the distance of the target and presented results separately having assumed different distances. A more general approach is to marginalize over the distance range using an appropriate prior, for example that given by [66]. The same applies to the age estimates.

What I want to stress here is that the parameter space to be searched and the targets to be searched should be part of the search optimisation procedure, as well as the search parameters themselves. In previous works these aspects have been considered separately: e.g. [140, 89, 152] and [141, 121, 170, 139]. The interplay between these quantities, for some assumed prior, is very difficult to intuitively predict and hence it is important to have a rational method to do so. The method that I propose here effectively achieves this goal and lends itself to further generalisations.

4.6 Appendix: linear programming

In this appendix I provide some further details of the method of Linear Programming (LP) and its application to this problem.

Recall that the occupation numbers $X_{i,s}$ (or equivalently X_j) were originally specified as binary numbers, i.e. $X_{i,s}$ could be either 0 or 1. It is however non-trivial to design an algorithm which solves the optimisation problem described in Sec. 4.2.2. Rather than trying to do so, I have formulated the problem by taking $X_{i,s}$ to be real and requiring $0 \leq X_{i,s} \leq 1$. I have seen how the optimisation problem can be solved using linear programming (LP).

The first question that arises is: by allowing $X_{i,s}$ to be real, do the solutions which maximize P_{sum} have the vast majority of the $X_{i,s}$ as either 0 or 1? This is observed empirically to be true in all the cases that I have studied in this chapter. I shall now demonstrate that this is in fact a more general feature. I shall restrict ourselves here to the case when there are two possible set-ups for each cell.

To illustrate this I define the efficiency $E_{i,s} = P_{i,s}/C_{i,s}$. LP yields a set of non trivially occupied cells which can be ordered in decreasing values of $E_{i,s}$; thus, $i = 1$ corresponds to the cell with the largest efficiency, $i = 2$ the second largest and so on. Consider first the non-degenerate case where all $E_{i,s}$ are mutually different and I assume that in each cell i only one of the two $X_{i,s}$ is strictly bigger than 0. I will show in this case that the cell with the lowest efficiency (let j be the index for this cell) is the only one which can have a fractional occupation: $0 < X_{j,s_j} \leq 1$. If any cell with index l with a higher efficiency would have a fractional occupation, the total P_{sum} can be increased by decreasing X_{j,s_j} and increasing X_{l,s_l} until either $X_{l,s_l} = 1$ or $X_{j,s_j} = 0$ such that the total cost C_{max} remains constant. This argument holds for all $l < j$, hence, all X_{l,s_l} with $l < j$ must be unity. If X_{j,s_j} is set to be 0 the cell with index $j - 1$ is now the one with the lowest efficiency among all non-trivially occupied cells. Since $C_{i,s} \ll C_{\text{max}}, \forall i$ the total cost will be changed marginally if I set X_{j,s_j} either to 0 or to 1.

If a subset of non-trivially occupied cells has the same efficiency, P_{sum} and C_{max} do not change if I decrease the occupation $X_{i,s}$ by an amount $\Delta_{i,s}$ and increase the occupation of another cell X_{j,s_j} by Δ_{j,s_j} if both cells have the same efficiency and if $\Delta_{j,s_j}/\Delta_{i,s} = P_{i,s}/P_{j,s_j}$ is fulfilled. I can shift the occupation among these cells such that one part has occupation 1 and another part 0. One cell of this subset will likely have a fractional occupation which can be set as well to either 0 or 1 without changing the total C_{max} significantly. Following the previous argument, all cells with higher efficiency must have the occupation number equal to unity.

I would now like to show that for each cell i with non-trivial occupation numbers, only one of the two $X_{i,s} > 0$, unless the cell has the lowest efficiency. I illustrate this by using the geometrical interpretation of LP. The set of inequalities described earlier define a polygon in the space of the $X_{i,s}$ in which valid solutions exist. The set of inequalities can lead to either no solutions, an unbounded problem, a unique solution or infinity many solutions. In the situation only the latter two cases are possible. If only a single solution is possible the optimal point lies in one corner of the polygon. If more than one corner points were to lead to the same optimal P_{sum} any point in the volume enveloped by these points yield the same P_{sum}. The costs of the ordered set of non-trivially occupied cells can be summed from cell 1 (the one with the highest efficiency) up to the cell $j - 1$. The remaining cost is then $C_j = C - \sum_{i=1}^{j-1} \sum_s C_{i,s} X_{i,s}$. We consider now a subset of inequalities valid for cell j. There
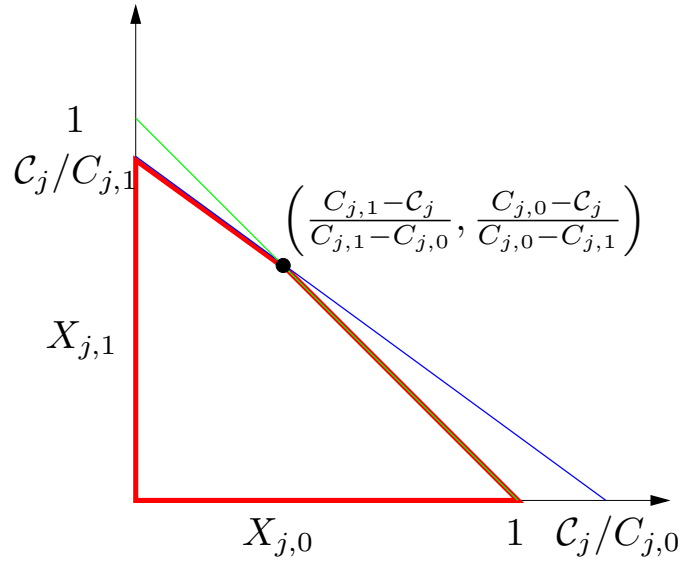
Figure 4.20: The red tetragon envelops a volume of variable space in which all inequalities are fulfilled.

is $X_{j,s_j} > 0$, $\sum_{s_j} X_{j,s_j} < 1$ and $\sum_{s_j} C_{j,s_j} X_{j,s_j} < \mathcal{C}_j$. The polygon is either a triangle, if $\mathcal{C}_j/C_{j,s_j}$ is either bigger than 1 or smaller than 1 for both s_j. As depicted in Figure 4.20, the polygon is a tetragon if one $\mathcal{C}_j/C_{j,s_j}$ is bigger than 1 for one of the s_j and smaller than 1 for the other. Both fractions being bigger than 1 means that enough remaining cost is left to fully occupy the cell with one of the two X_{j,s_j}. Smaller than 1 means, the cell is the non-trivially occupied cell with the smallest efficiency. The remaining costs will be used in this cell.

   If the enveloping polygon is a tetragon for the cell j with the lowest efficiency, P_{sum} is maximized if I chose the X_{j,s_j} to be in one of the corners $(\min(\mathcal{C}_j/C_{j,0}, 1), 0)$,$(0, \min(\mathcal{C}_j/C_{j,0}, 1))$ or $((C_{j,1} - \mathcal{C}_j)/(C_{j,1} - C_{j,0}), (C_{j,0} - \mathcal{C}_j)/(C_{j,0} - C_{j,1}))$. The latter case means that the LP optimisation leads to a fractional occupation of both X_{j,s_j} simultaneously. Again, setting one X_{j,s_j} to 0, the other one to 1 or both to 0 will not change C_{max} significantly. I can however not exclude that pathological cases which are not covered by the assumptions. In practice I only observed the cases decribed here and moreover, I can always shift a few $X_{i,s}$ such that I only have integer occupations for only a small change in the computational cost budget.

Chapter 5

First application of the optimisation method and its expansion

Caveats:
This work has been submitted to *Phys. Rev. D* [134]. Most of the material presented in this chapter is taken from it. Refer to Appendix B for the description of my contributions.

In Chapter 4 I presented an optimisation method which tells us how to distribute computing resources in targeted CW searches so that the detection probability is maximized. The method also provides the optimal search set-ups for the different targets in different waveform frequencies. The basic idea is to break the large parameter space[1] into many small *cells* and to estimate the computing cost and the detection probability (P) for a signal with waveform parameters in each cell for a number of different search set-ups. I use these two quantities to rank what cells and with what search set-up should be searched first so that the overall detection probability is maximized. This is done with a linear programming technique. The interplay between the different factors is not trivial and the results are not easy to guess without using the optimisation method.

In this chapter I present the first application of this method to set up a directed search by using the first observing run (O1) data of Advanced LIGO [56]. Following Chapter 4, I investigate different astrophysical targets and priors and consider a range of search set-ups for different coherent segment durations, and optimise over all these. I expand with respect to Chapter 4 because i) whereas in Chapter 4 for each coherent segment duration I considered a single grid spacing combination (corresponding to $m_f = m_{\dot{f}} = m_{\ddot{f}} = 0.18$) now I consider for each coherent segment duration many different combinations of grid spacings and optimise over these, ii) for each grid spacing combination, I fold in the *measured* mismatch distributions obtained from the existing search codes for all the grid spacings and set-ups considered, rather than the analytical estimate which can have very large errors,

---

[1] I refer here to the waveform parameter space. In the following I will use the shorthand "parameter space" to indicate it.

iii) I revise the computational cost model for the search software to account for recent enhancements in computational efficiency, iv) I evaluate the loss in detection efficiency due to a mistake in the estimate of the age of the objects, and v) I introduce simplifications with respect to the strictly optimal solution based on practical considerations and estimate the impact on the detection probability.

5.1 The Search

Based on the results of Chapter 4 I concentrate on three targets, Vela Jr., Cas A and G347.3, and illustrate the design of three directed searches for continuous GW signals from these. I assume using the volunteer computing project Einstein@Home [23], data with the average noise of the Advanced LIGO detectors during their first science run (designated as O1), and with the duration and average duty factor of the LIGO O1 data.

5.1.1 Search method

Ideally, a fully coherent search would be the most sensitive. However, when the span of a data exceed a few days and the search extends to frequencies above 100 Hz, the computational cost of such search becomes too high. I hence take a semi-coherent approach in which the data is divided into shorter segments each spanning the same observation time T_{coh}. Each of these segments are analyzed coherently and afterwards combined incoherently. I consider the same detection statistic, $\widehat{2\mathcal{F}}$, as in Chapter 4 and its GCT (Global correlation transform) implementation [150], used in the most recent Einstein@Home papers [55, 142, 177].

In Gaussian noise, $N_{\mathrm{seg}}\widehat{2\mathcal{F}}$ follows a non-central chi-squared distribution with $4N_{\mathrm{seg}}$ degrees of freedom [111].

5.1.2 Template banks

I search for different waveforms. Each waveform is defined by the parameters $(h_0, f, \dot{f}, \ddot{f}, \alpha, \delta, \psi, \iota, \phi_0$) introduced in Chapter 3. However the coherent search method analytically maximizes over the parameters $(h_0, \psi, \iota, \phi_0$) and so I only need to explicitly search over $(f, \dot{f}, \ddot{f}, \alpha, \delta)$. Since I consider directed searches the sky position is known and the different waveforms are determined by only ($f, \dot{f}, \ddot{f}$).

With the term "template bank" I indicate the collection of waveforms that I explicitly search for. These are defined by values of the waveform parameters $(f, \dot{f}, \ddot{f})$. The spacings in these parameters in principle has to be fine enough that a real signal, with waveform parameters lying between adjacent points in the template bank would still be detectable.

Two grids are set-up: a coarse grid, used for the coherent searches, and a fine grid, used for the incoherent searches. The frequency spacing δf is the same for both the coherent and incoherent searches whereas the frequency derivative spacings are refined by a factor of $\gamma^{(1)}$ and $\gamma^{(2)}$ going from the coherent to the incoherent grids: $\delta \dot{f}_f = \frac{\delta \dot{f}_c}{\gamma^{(1)}}$ and $\delta \ddot{f}_f = \frac{\delta \ddot{f}_c}{\gamma^{(2)}}$. The total number of waveforms

that are searched is $N_{\text{fine}} = \gamma^{(1)}\gamma^{(2)}N_{\text{coh}}$ with $N_{\text{coh}} = N_{f_c}N_{\dot{f}_c}N_{\ddot{f}_c}$, where N_{f_c}, $N_{\dot{f}_c}$ and $N_{\ddot{f}_c}$ are the number of coarse grid points in f, $\dot{f}$ and $\ddot{f}$ respectively.

As mentioned in previous chapters, the grid spacings $\delta f_c, \delta \dot{f}_c, \delta \ddot{f}_c$ are parametrized by the parameters m_f, $m_{\dot{f}}$, $m_{\ddot{f}}$ as follows [149]:

$$\delta f_c = \frac{\sqrt{12m_f}}{\pi T}, \tag{5.1}$$

$$\delta \dot{f}_c = \frac{\sqrt{180m_{\dot{f}}}}{\pi T^2}, \tag{5.2}$$

$$\delta \ddot{f}_c = \frac{\sqrt{25200m_{\ddot{f}}}}{\pi T^3}. \tag{5.3}$$

Every template bank for a given search set-up (T_{coh} and N) is characterized by its mismatch distribution. The mismatch μ is the quantity that measures how much signal-to-noise may be lost due to the mismatch between a signal parameters and the discrete template bank. The finer the template bank is, in general the smaller the mismatch. The mismatch distribution can be measured by simulating signals (no noise) and measuring the signal-to-noise ratio $\rho^2_{\text{no-mismatch}}$ associated with a search performed with a perfectly matched template (i.e. a template with parameters identical to the signal parameters) and the signal-to-noise ratio ρ^2_{mismatch} associated with the maximum of the detection statistic from a search performed with the template grid that I want to characterize:

$$\mu := \frac{\rho^2_{\text{no-mismatch}} - \rho^2_{\text{mismatch}}}{\rho^2_{\text{no-mismatch}}}. \tag{5.4}$$

The signal-to-noise ratio ρ^2 for a semi-coherent $\mathcal{F}$-statistic search with N segments is connected to the expectation value of $\hat{\mathcal{F}}$ as follows: $E[2\hat{\mathcal{F}}] = \rho^2 + E[n]$, where $E[n]$ is the expected value of noise alone.

I derive the mismatch distribution for a given search set-up T_{coh}, N and a template bank defined by $m_f, m_{\dot{f}}, m_{\ddot{f}}, \gamma^{(1)}$ and $\gamma^{(2)}$ by injection-and-recovery Monte Carlos following Equation (5.4). In particular, 500 artificial signals are produced with gaps simulating the realistic output from the LIGO O1 detectors. These data streams are jointly searched with our standard semi-coherent search[2]. Because these injection-and-recovery Monte Carlos are performed on the noise-free data streams, the computed values of the search code correspond to the expectation values of the statistic, $E[\hat{\mathcal{F}}]$, and therefore I obtain the mismatches directly from Equation (5.4). The range of the parameters of the 500 signals is given in Table 5.1. I have considered over 2000 different spacings. The ranges for these spacings are listed in Table 5.2. For illustration purposes, Figure. 5.1 shows the mismatch distribution for $T_{\text{coh}} = 15$ days, $m_f = 0.15$, $m_{\dot{f}} = 0.3$, $m_{\ddot{f}} = 0.003$, $\gamma^{(1)} = 8$ and $\gamma^{(2)} = 20$.

---

[2]The artificial data is created with `lalapps_Makefakedata_v4`. The search is performed using `lalapps_HierarchSearchGCT` (GCT). Both programs are part of the LIGO Algorithm Library (LALSuite) [20].

Table 5.1: Injection parameters used in mismatch investigation

Parameter	Range
Frequency [Hz]	$151\,\text{Hz} \leq f \leq 152\,\text{Hz}$
First spin-down [Hz/s]	$-10^{-7}\,\text{Hz/s} \leq \dot{f} \leq -10^{-12}\,\text{Hz/s}$
Second spin-down [Hz/s^2]	$10^{-22}\,\text{Hz/s}^2 \leq \ddot{f} \leq 5 \times 1500\,\text{Hz}/(330\,\text{yr})^2$

Notes: Parameters of the fake signals used to derive the mismatch distributions. f is uniformly randomly distributed; $\dot{f}$ and $\ddot{f}$ are log-uniformly randomly distributed.

Table 5.2: Template bank parameters

Parameter	Range
T_{coh} [Days]	10, 15, 20, 30, 60 Days
m_f	$0.1 \leq m_f \leq 1.0$
$m_{\dot{f}}$	$0.1 \leq m_{\dot{f}} \leq 1.0$
$m_{\ddot{f}}$	$0.001 \leq m_{\ddot{f}} \leq 1.5$
$\gamma^{(1)}$	$1 \leq \gamma^{(1)} \leq 50$
$\gamma^{(2)}$	$5 \leq \gamma^{(2)} \leq 100$

Notes: The total observation duration is 120 days. It is divided into $N = 120/T_{\text{coh}}$ coherent segments.
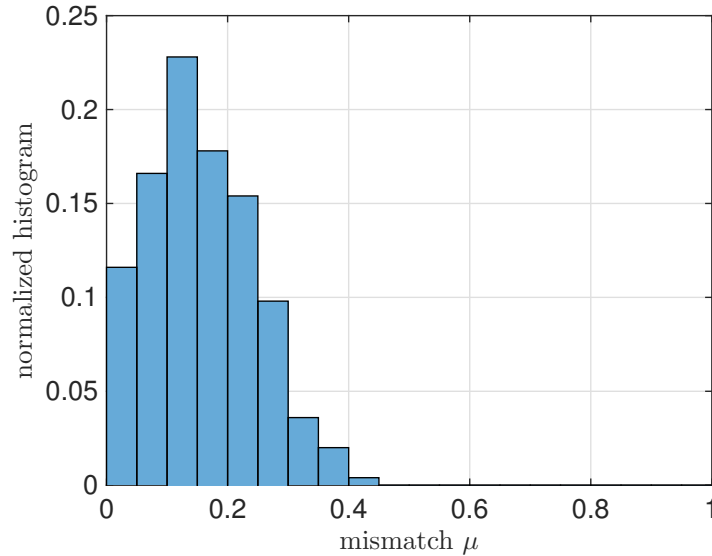

Figure 5.1: This histogram shows the mismatch distribution for the grid spacing: $m_f = 0.15$, $m_{\dot{f}} = 0.3$, $m_{\ddot{f}} = 0.003$, $\gamma^{(1)} = 8$, $\gamma^{(2)} = 20$ and T_{coh}=15 days. The average measured mismatch is $\langle \mu \rangle = 15.8\%$.

5.1.3 Search software timing

In computationally limited problems, one needs a rational process for allocating computational resources amongst different competing proposals. For example, should I allocate equal resources for each of Vela Jr., Cas A and G347.3 ? If not, then what is the optimal distribution of computing power ?

An important ingredient in the optimization is an accurate estimation of the run-time of the search pipeline for a given search set-up over a given parameter space. CW searches are the most computationally expensive gravitational wave searches and a great effort has been employed to optimise them. As a result, a well developed timing model has been developed for this main search pipeline. Furthermore, the use of Einstein@Home demands that I am able to predict the run-time of the work-units assigned to each of the host machines, which adds a further incentive to characterize the software accurately.

The time τ_{total} that it takes to perform a search a parameter-space volume covered by N_{coh} coarse grid templates and N_{fine} fine grid templates, using data from N_{det} detectors, divided among N segments can be written as:

$$
\begin{aligned}
\tau_{\text{total}} =& N N_{\text{det}} N_{\text{coh}} \tau_{\text{RS}} + N N_{\text{inc}} \tau_{\text{sum}\mathcal{F}} \\
&+ N_{\text{inc}} \tau_{\text{Bayes}} + N_{\text{can}} \tau_{\text{Recalc}}.
\end{aligned}
\tag{5.5}
$$

The timing coefficients τ_{RS}, $\tau_{\text{sum}\mathcal{F}}$, τ_{Bayes} and τ_{Recalc} are determined based on computing time measurements executed with various search set-ups on `Intel Xeon E3-1231 v3` CPUs, [3].

The first term in Equation (5.5) is the cost of the coherent step. When searching over several thousand signal frequency bins corresponding to the same sky position and spindown values, the best algorithmic implementation of the $\mathcal{F}$-statistic is obtained by carrying out the frequency demodulation of the signal by resampling a down-sampled time-series according to τ_{SSB} and then performing an FFT [111, 144]. Our most recent enhancement of the search codes uses this resampling + FFT method. τ_{RS} is the time that it takes to calculate a value of the coherent detection statistic, corresponding to a single template, using data from a single detector and from a single segment. It can be written as [31]

$$
\tau_{\text{RS}} = \tau_{\text{Fbin}} + \frac{N_{\text{samp}}^{\text{FFT}}}{N_{\text{Fbin}}} (\tau_{\text{FFT}} + R \tau_{\text{spin}}),
\tag{5.6}
$$

where τ_{Fbin} is the time spent on operations on each output frequency bin, τ_{FFT} is the time spent on the FFT per sample $N_{\text{samp}}^{\text{FFT}}$ of the resampled and zero-padded time series, and τ_{spin} is the time spent per sample of the source-frame resampled time series without zero-padding, with length $R N_{\text{samp}}^{\text{FFT}}$ where $R \leq 1$. Zero-padding is used in order to obtain the desired frequency resolution of the resulting $\mathcal{F}$-statistic. The timing coefficients of Equation (5.6) are: $\tau_{\text{Fbin}} = 6.0 \times 10^{-8}$ s, $\tau_{\text{FFT}} = 3.3 \times 10^{-8}$ s, $\tau_{\text{spin}} = 7.5 \times 10^{-8}$ s.

The second term in Equation (5.5) is the **cost of the incoherent step**: For every fine grid point I sum N detection statistic values. For $2 \leq N \leq 12$ the timing coefficient $\tau_{\text{sum}\mathcal{F}}$ is

$$
\tau_{\text{sum}\mathcal{F}} = 7.28 \times 10^{-9} - 3.72 \times 10^{-10} N \ (\text{s}) \ .
\tag{5.7}
$$

---

[3] http://ark.intel.com/de/products/80910/Intel-Xeon-Processor-E3-1231-v3-8M-Cache-3_40-GH

Since the efficiency of adding up detection statistic values increases with the number of segments, there is a negative term in Equation (5.7) proportional to number of segments N. Note that Equation (5.7) has been measured by timing the search on set-ups where N varies between 2 and 12. Hence, relation (5.7) may not hold outside of this range.

As done in [55, 142] the main detection statistic is augmented with variants that are robust to detector artefacts, namely the line-robust $\hat{B}_{\mathrm{S/GL}}$ and the transient-robust $\hat{B}_{\mathrm{S/GLtL}}$, as well as a detection statistic which is sensitive to some types of transient signals, $\hat{B}_{\mathrm{tS/GLtL}}$ [119, 118, 117]. The third term in Equation (5.5) is the time to compute these specialized statistics given the single detector and multi detector coherent detection statistic values (see Equation (13) of [117]). This is the reason why τ_{Bayes} is independent of the number of segments. $\tau_{\mathrm{Bayes}} = 4.4 \times 10^{-8}$ s. For set-ups with just a few segments, the cost of computing these various statistics can be larger than the cost of the incoherent step.

The last term in Equation (5.5) is the computing cost for the recalculation all these detection statistics at the exact fine grid point in all the coherent segments. This is done only for the N_{can} candidates that are in the top list[4]. In the last few Einstein@Home searches the number of candidates in the top-list is $N_{\mathrm{can}} = O(1000)$ and this recalculation cost is negligible with respect to the costs of the other three terms.

The computing time, and consequently the values of the timing coefficients, in general depend on the CPU on which the search is performed. Since the volunteer computing project Einstein@Home comprises a broad range of different CPUs, as I optimize this search for running on Einstein@Home for a predetermined length of time, we need to determine how much computing power that corresponds to. A timing analysis based on duration of the work units (WUs) of the O1 all-sky low frequency Einstein@Home search [126], yields the results shown in Figure 5.2: run times are bi-modally distributed, with a mode centered at 8 hours, the other at 24 hours. Based on this I divide the host population of Einstein@Home into two types: hosts that showed a runtime of less than 14 hours were put in one category (A) and hosts that needed more time than that were placed in the other category (B). The CPU models in host class (A) have an average 8-hours runtime which is equivalent to the fast nodes on the ATLAS computational cluster at the Albert Einstein Institute in Hannover [32]. Therefore the timings from fast nodes on ATLAS can be ideally used for these Einstein@Home (A)-cores. Based on the O1 low frequency all-sky search I estimate there are about 5300 cores in category (A) and a similar number of cores in category (B). In the following I will assume using only the (A)-type hosts of Einstein@Home, and hence that one Einstein@Home month (EM) corresponds to 5300 (A)-type cores used continuously for 1 month.

5.2 Astrophysical priors

An important feature of this optimization scheme is that it forces me to explicitly incorporate the astrophysical priors on the signal parameters. In particular, I need to choose the astrophysical priors on the following parameters for each target:

---

[4]The top list is the list of top candidates that is returned by the Einstein@Home volunteer computer to the main Einstein@Home server. Typically multiple top lists will be returned, each ranked according to a different detection statistic.
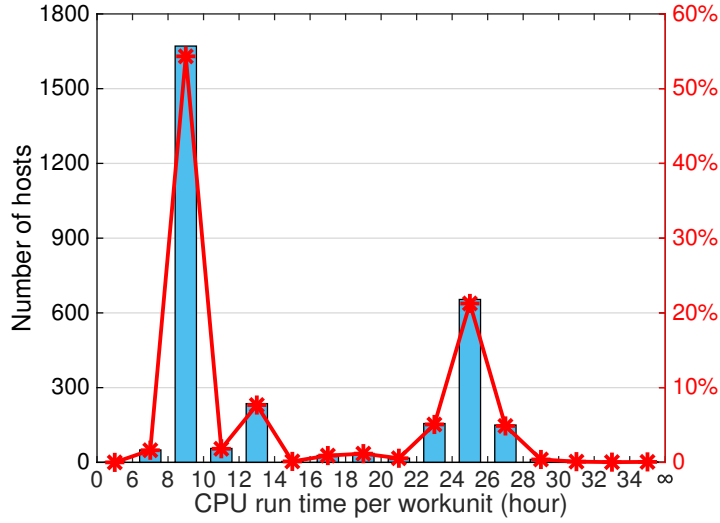
Figure 5.2: Distribution of the run-times of the Einstein@Home O1 low frequency all-sky search WUs. The data in this figure is taken from a sample of 3076 hosts out of total 28764 hosts of Einstein@Home.

- the age and distance of the target sources. The age influences the spindown range that should in principle be searched. The distance of the source directly influences the amplitude h_0 of the signal. For some targets such as Cas A there is very little uncertainty in the distance and/or age of the object, so the prior is chosen as a delta function. Other sources like Vela Jr., for instance, have large uncertainty in age and distance. However as was done in Chapter 4, I pick delta-functions at the extremes of the possible range. In doing this I might also include non-physically motivated age-distance combinations. I do this only to give a sense of the impact of different priors on the final results. Note that the uncertainty in measurement on distance of the sources will might be improved by Gaia spacecraft [33].

- The star's ellipticity ε and the fraction x of spin-down energy carried away in GWs influence the GW signal amplitude h_0. For the former I pick a log-uniform distribution; for the latter I pick a value inspired by the upper limits measured with targeted searches [62]

- The P_c depends not only on h_0, but also on the prior probability $P(f, \dot{f}, \ddot{f})$ that the actual signal is in the cell defined by specific values of $(f, \dot{f}, \ddot{f})$.

The results in Chapter 4 indicate that the distance of an object is the most important parameter in determining its GW detectability. Among the targets considered in Chapter 4 targets Vela Jr. is the only source which has large uncertainties both in age and distance [35]. However, even assuming the a fairly pessimistic value of 750 pc for the distance of Vela Jr. [67], it still contributes the most to the total detection probability with respect to all other targets. I pick the four extremes for the priors on age and distance of Vela Jr.: close and young (CY), close and old (CO), far and young (FY) and far

Table 5.3: Point source targets considered in this paper

SNR G name	Other name	Point source J	D_{kpc}	τ_{kyr}
111.7–2.1	Cas A	232327.9+584842	3.3–3.7	0.31–0.35
266.2–1.2	Vela Jr.	085201.4–461753	0.2–0.75	0.7–4.3
347.3–0.5		171328.3–394953	1.3	1.6

and old (FO) Vela Jr.. It is important to keep in mind that the astrophysically viable alternatives are CY and FO and there is no support for CO and FY. However, I shall include all four alternatives for the purpose of illustrating the impact on the optimization scheme. Realistic searches will obviously consider only CY and FO.

Table 5.3 details the parameters of the three objects that I consider in this paper. Searches for signals from one of the youngest known SNR, Cas A, have been carried out with LIGO data [42, 177, 40]. The reason for targeting this source is that a young object is more likely to be spinning down faster and hence there is more kinetic energy that could potentially be radiated away in GWs. Here I will see that Cas A is the third source that contributes the overall detection probability. Vela Jr. and G347.3 contribute much more to the total detection probability and are thus more promising targets. While [40] presents searches and upper limits for Vela Jr. and G347.3, these have not been the primary targets for any CW search to date. Thus there have not been any deep CW searches for these two objects so far.

The ellipticity ε is the least known parameter so here I take a flat probability density on $\log \varepsilon$ within a conservative range of values. I target weak signals and hence the maximum value of ε I allow in the ith cell is:

$$\varepsilon_i^{\mathrm{max}} = \min(\, \varepsilon_i^{\mathrm{sd}}, \, \varepsilon_i^{\mathrm{age}}, \, 10^{-6}\,), \tag{5.8}$$

where $\varepsilon_i^{\mathrm{sd}}$ and $\varepsilon_i^{\mathrm{age}}$ are the spin-down ellipticity upper limit and the spindown age-based ellipticity upper limit respectively:

$$\varepsilon^{\mathrm{sd}} = \sqrt{\frac{5c^5}{32\pi^4 G} \frac{x|\dot{f}|}{I f^5}}\,. \tag{5.9}$$

and

$$\varepsilon^{\mathrm{age}} = \frac{c^2}{16\pi^2 f^2} \sqrt{\frac{10c}{GI\tau}}\,. \tag{5.10}$$

In Equations (5.9) and (5.10), f is the instantaneous frequency of the emitted GW signal, G Newton's constant, c the speed of light, and τ the age of the source. I is the the moment of inertia and I use its standard value $10^{38}\,\mathrm{kg\,m^2}$ for all the results in this paper. x is the fraction of spin-down energy loss due to GW emission. The latest observational limits on GW emission from the Crab and Vela pulsars constrain x to less than 0.2% and 1% respectively [62]. In this paper, I will assume $x = 1\%$. According to the results of [107], the realistic maximum value of ε is expected to be smaller than 4×10^{-6}. Hence the third limit I use in this paper is 10^{-6}. I take $\varepsilon^{\mathrm{min}} = 10^{-14}$ because deformations

of a compact star due to the internal magnetic field (at least 10^{11} G) are not expected to be smaller than $\sim 10^{-14}$ [70]. Based on the above discussion, the prior $p(\varepsilon)$ is:

$$p(\varepsilon) = \begin{cases} \frac{1}{\varepsilon} \frac{1}{\log(\varepsilon^{\text{max}}/\varepsilon^{\text{min}})} & \varepsilon^{\text{min}} < \varepsilon < \varepsilon^{\text{max}} \\ 0 & \text{elsewhere}. \end{cases} \tag{5.11}$$

Since the GW frequencies emission frequencies are unknown, this search encompasses a large range; namely, from 20 to 1500 Hz. For a given f, the $\dot{f}$ and $\ddot{f}$ ranges are determined by the fiducial age of the source τ:

$$\begin{cases} 20\,\text{Hz} \leq f \leq 1500\,\text{Hz} \\ -f/(n-1)\,\tau \leq \dot{f} \leq 0\,\text{Hz/s} \\ 0\,\text{Hz/s}^2 \leq \ddot{f} \leq n\dot{f}^2/f. \end{cases} \tag{5.12}$$

In the second equation I take $n = 2$ to encompass the broadest range of $\dot{f}$ values. In the third equation I assume a braking index $n = 5$, corresponding to phase evolution purely due to GW emission. For all other mechanisms $n < 5$ and in particular for pure dipole electromagnetic emission $n = 3$ (see e.g. [164]). Therefore, the search ranges for $\dot{f}$ and $\ddot{f}$ in (5.12) encompasse all combinations of emission mechanisms. After dropping the $\ddot{f}$ dependence, for the signal probability density $P(f, \dot{f})$, I consider both uniform and log-uniform priors on the search range of f and $\dot{f}$ which reflect my ignorance on those signal parameters.

5.3 The optimization

The optimization scheme is introduced in Chapter 4. The starting point is to divide the parameter space into non-overlapping small cells such that the computing cost to search each cell and the resulting detection probability are roughly constant within each cell. The cost for each should also be much smaller than the full computing cost budget available to us. For each cell, I calculate the computing cost and detection probability. For each cell I define the efficiency, that is the ratio of detection probability to computing cost. In the absence of any constraint apart from the total budget, one could proceed simply by picking the most efficient cells till the computing budget is exhausted. However, I do have an additional constraint, namely that I do not want to search the same parameter space cell with multiple search set-ups. It is shown in Chapter 4 how this constraint can be included in the optimization using linear programming techniques.

The search set-ups are defined by 6 parameters: the segment coherent duration T_{coh}, the nominal mismatch parameters m_f, $m_{\dot{f}}$, $m_{\ddot{f}}$, and the refinement factors $\gamma^{(1)}$ and $\gamma^{(2)}$ (see details in Section 5.1.2). For each given search set-up I can compute the mismatch distribution, i.e. the distribution of the fractional loss in signal-to-noise ratio due to the discreteness of the template bank[5].

The optimization not only determines the best search set-ups but also how to distribute the computing budget among the different astrophysical targets and over the parameter space. In Chapter 4 I

---

[5]Mismatch distributions of these set-ups are computed for Vela Jr., since it is responsible for most of the detection probability

presented this optimization scheme under a set of simplifications. I now take Chapter 4 as the starting point for an actual search design but here I forego the simplifications that I made in Chapter 4 and take into account issues of feasibility and practicality. I shall take rectangular cells in $(f, \dot{f})$ space, and each cell will be $10\,\mathrm{Hz}$ wide in frequency and $10^{-9}\,\mathrm{Hz/s}$ in $\dot{f}$. To completely specify the parameter space cells, I need to include $\ddot{f}$, and each of the $(f, \dot{f})$ cells are allowed to take all permissible values of $\ddot{f}$. As mentioned above, for each cell, each search set up, and every choice of astrophysical prior, I calculate the computing cost and detection probability. Since it is not possible to predict the mismatch distribution of the GCT search for a given set-up, these are produced from thousands of injection-and-recovery Monte Carlos.

In principle, the above ingredients are sufficient for the optimization scheme. However, certain obvious simplifications can be made based on practical considerations:

- Among all the set-ups with the same T_{coh}, for every value of the computing cost, I select the set-up which has the lowest average mismatch. In this case, as I shall describe in greater detail below, this results in 71 seeded set-ups for all the different values of T_{coh} considered.

- Among all the cells, each with 71 set-ups, I select those so that the sum of relative detection probabilities constrained by the available computing budget, is maximized. This is done through linear programming.

- Since I find that the optimal choice of cells spans a very broad frequency range, I determine the loss in detection probability caused by extending the search parameter space to include the broadest frequency band. I further evaluate the loss incurred with respect to the optimal solution due to utilizing the same set-up across all cells for every astrophysical target. Both these choices, when viable, greatly simplify the post-processing of the results.

- I compare the final results from different sets of priors, estimate the loss in detection efficiency due to having optimized assuming a wrong age and choose the set-up such that this loss is the smallest.

In the next sections I describe the above steps in greater detail.

5.3.1   Set-ups: primary selection

Running the optimization scheme on ~ 2000 set-ups is computationally too burdensome. I hence down-select, among the ones with the same T_{coh}, those that yield the lowest average mismatch at fixed computing cost over the entire prior parameter range of Vela Jr.. In principle this selection should be done separately for every target, but here I simplify the procedure in this manner because Vela Jr. contributes the bulk of the detection probability.

Figure 5.3 shows computing cost and average mismatch for 432 set-ups corresponding to different grid spacings and $T_{\mathrm{coh}} = 15$ days. Out of these, 19 are selected which have the lowest measured average mismatch at fixed computing cost. Considering different values for T_{coh} I select 71 set-ups : 13 are from $T_{\mathrm{coh}} = 10$ days, 19 from $T_{\mathrm{coh}} = 15$ days, 15 from $T_{\mathrm{coh}} = 20$ days, 14 from $T_{\mathrm{coh}} = 30$ days and 10 from $T_{\mathrm{coh}} = 60$ days.
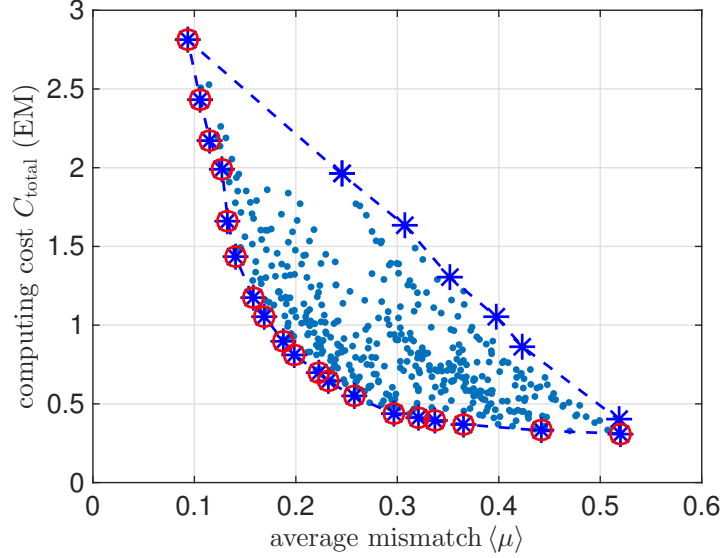
Figure 5.3: 432 set-ups with $T_{\mathrm{coh}} = 15$ days. The 19 blue stars in red circle are selected for further consideration as explained in the text.

The measured average mismatch $\langle\mu\rangle$ of each of these distributions is used to reduce the expected signal-to-noise ratio ρ^2 of a putative signal. More specifically, with respect to Equation (3.55) I now use a more realistic estimate

$$\rho^2 \rightarrow (1 - \langle\mu\rangle) \times \rho^2. \tag{5.13}$$

This estimate folds-in the sensitivity-loss effect of using finite grids and does it realistically because it is based on the measured mismatch distributions of the actual search codes.

5.3.2 Optimization under different assumptions

Following Section 4.4, I now use linear programming to determine how to best pick targets, waveform parameter space to search and search set-ups under a set of different assumptions on the age and distance of the source. I consider 71 different set-ups. A significant difference with respect to [133] is that here I consider a number of different grid spacings for the same T_{coh} and, as explained above, *the actual* mismatch associated to each of them.

Figure 5.4 shows the results of the optimization under the assumptions that Vela Jr. is at a distance of 200 pc (C), that the signal frequency f and spindown $\dot{f}$ are uniformly distributed within their ranges (defined in Equation (5.12)) and with a 3 EM computing budget.

Figure 5.4 shows the result of the optimization procedure. Different colors represent search set-ups having different T_{coh}. The total detection probability $\mathcal{R}$ is defined in Equation (4.30) as the sum of detection probabilities of the selected parameter space cells. It is obvious that the higher $\mathcal{R}$ is, the more promising is the corresponding search. C indicates the total computational cost and in general
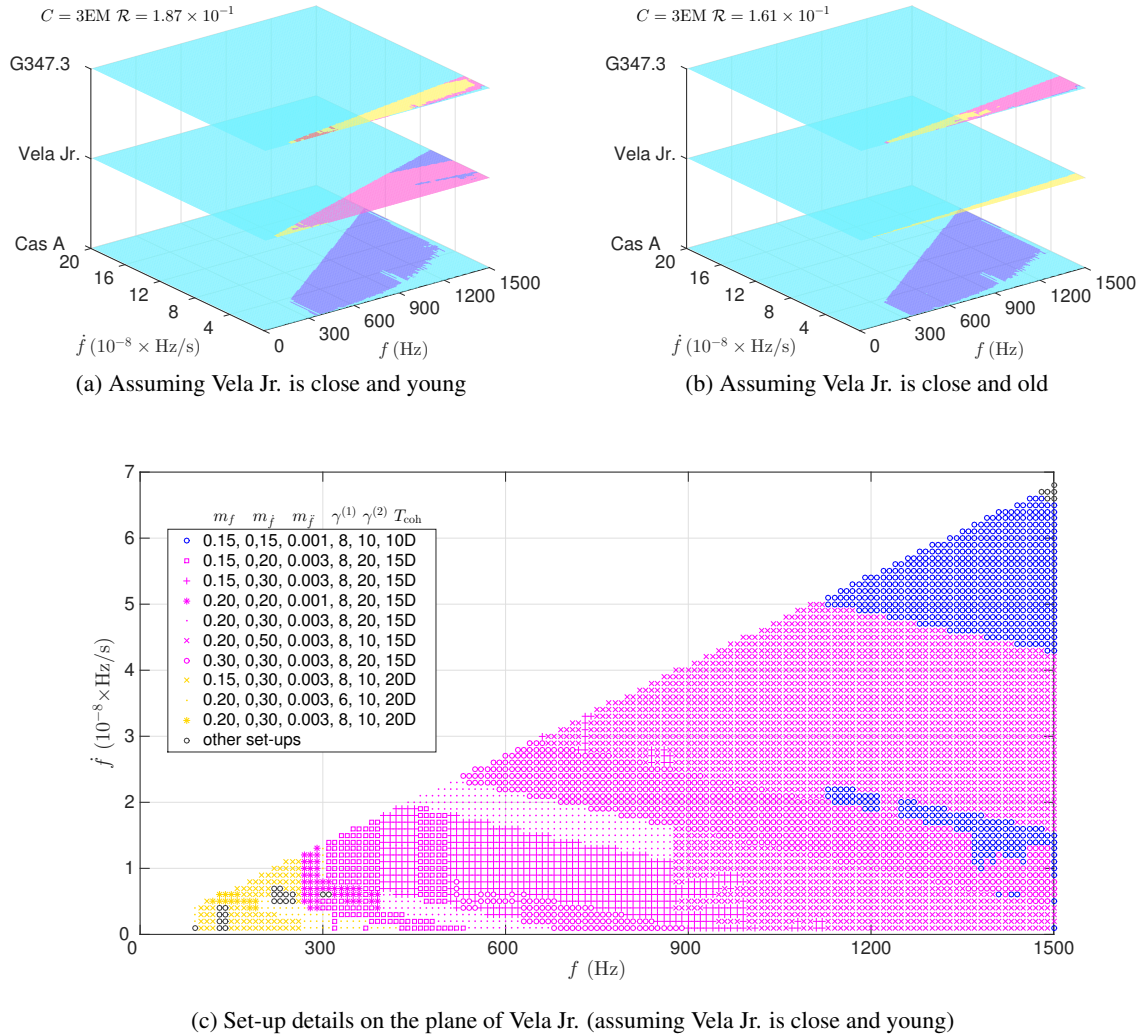
(a) Assuming Vela Jr. is close and young

(b) Assuming Vela Jr. is close and old

(c) Set-up details on the plane of Vela Jr. (assuming Vela Jr. is close and young)

Figure 5.4: Parameter space coverage assuming uniform f, $\dot{f}$ priors, Vela Jr. at 200 pc (C) and 3 EM computing budget. In panel (a) I assume Vela Jr.'s age is 700 years (Y) and in panel (b) I assume that Vela Jr. is 4300 years old (O). Cells in blue have 10-day T_{coh} set-ups, magenta indicates 15-day T_{coh}, yellow the 20-day T_{coh}, red the 30-day T_{coh}, and green the 60-day T_{coh} (although not used in either cases). The computing power used on Cas A, Vela Jr. and G347.3 is 1.36 EM, 1.14 EM and 0.50 EM, respectively, for the set-ups of panel (a), and 1.97 EM, 0.21 EM and 0.82 EM for the set-ups of panel (b). The contribution to the total detection probability from Cas A, Vela Jr. and G347.3 is 1.3%, 14.4% and 3.1% for panel (a), and 1.4%, 11.5% and 3.1% for panel (b). Note that each color represents set-ups which have the same length of coherent duration, but might differ in the grid spacings. Figure (c) shows the set-up details on Vela Jr. plane in Figure (a). For example, the blue circles represent the cells need to be searched by using the set-up: $m_f = 0.15$, $m_{\dot{f}} = 0.15$, $m_{\ddot{f}} = 0.001$, $\gamma^{(1)} = 8$, $\gamma^{(2)} = 10$, and $T_{\mathrm{coh}} = 10$ day.
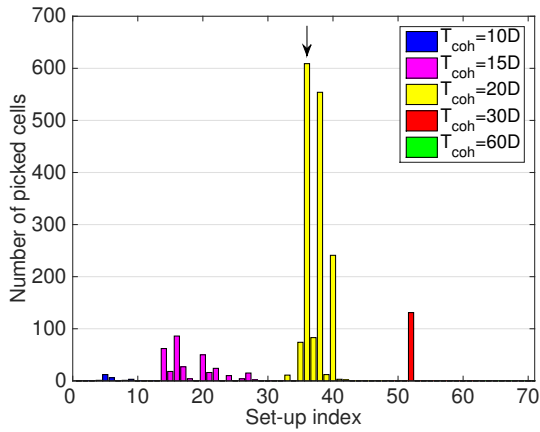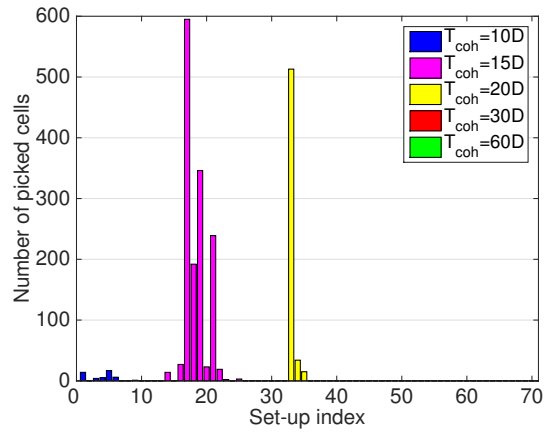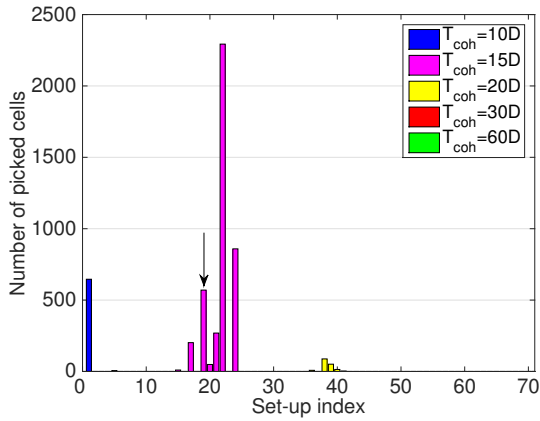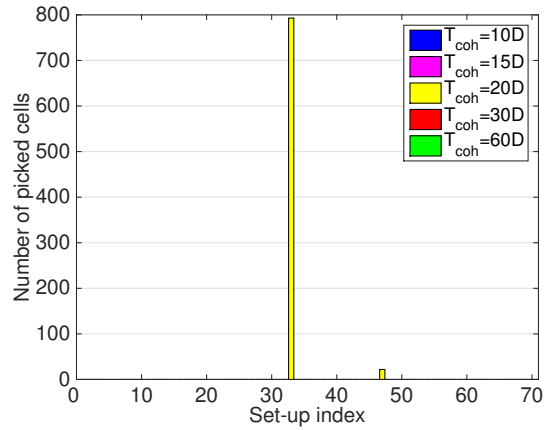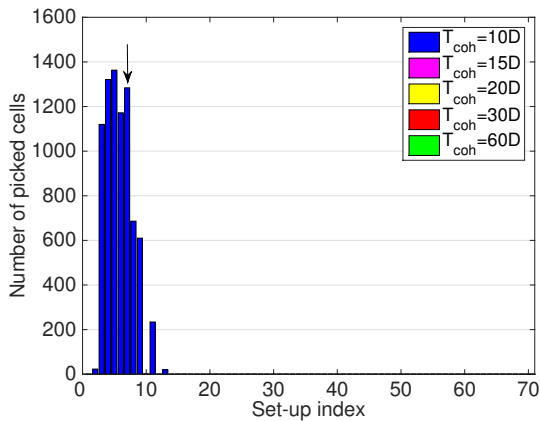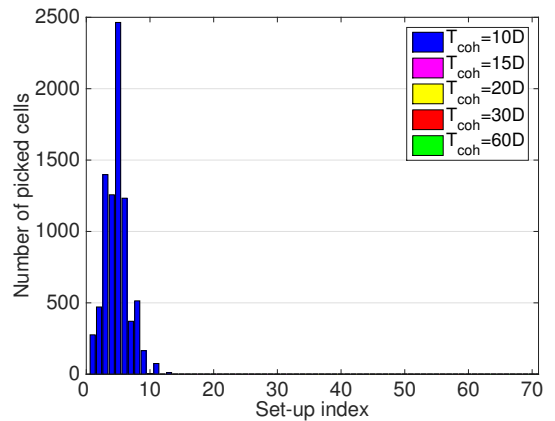
Figure 5.5: Optimal set-up details. The left hand-side figures show the set-ups assuming Vela Jr. is close and young. The right hand-side figures show the set-ups assuming Vela Jr. is close and old. As explained in in Section 5.3.4, the arrows indicate the set-ups that will finally be adopted in the search.

this will be equal to or smaller than the maximum budgeted 3EM. The results for Vela Jr. for the CY and CO cases can be summarized as follows:

- When Vela Jr.'s age is assumed to be 700 years, the spin-down parameter space to search is large and the T_{coh} chosen set-ups for Vela Jr. are 10 days, 15 days and 20 days (see Figure 5.4(a)). Figure 5.4(c) shows the Vela Jr. plane of Figure 5.4(a) and I can appreciate that more than 10 different set-ups constitute the optimal search for young Vela Jr.

- When Vela Jr.'s age is assumed at 4300 years, the spin-down parameter space shrinks and the T_{coh} chosen set-ups for Vela Jr. are all 20 days (see Figure 5.4(b)). This is the CO case and I emphasize again that there is no astrophysical support for this scenario. I include this to illustrate the effect of the priors on the optimization results.

The total detection probability $\mathcal{R}$ corresponding to the two different age priors is also different: 18.7% and 16.1% for the young and for the old Vela Jr., respectively. Under either assumptions Vela Jr. contributes the bulk of the total probability: 14.4% out of 18.7% and 11.5% out of 16.1%. However in the former case the Vela Jr. search uses up 38% of the computing budget whereas in the latter it only uses 7%.

Figures 5.5 reveals further details of the chosen set-ups. In particular panels (a), (c) and (e) show how many cells are searched with each of the different set-ups for G347.3, Vela Jr. (CY) and Cas A, respectively. Panels (b), (d), (f) show the same quantities but under the CO assumption for Vela Jr.. Assuming Vela Jr. is 700 yr old (CY), 20-day set-ups are mostly selected for G347.3, 15-day set-ups mostly for Vela Jr., and only 10-day set-ups for Cas A. If I assume that Vela Jr. is 4300 yr old, the parameter space of Vela Jr. shrinks due to the age limit. Only 20-day set-ups are selected for Vela Jr.. The computing savings incurred due to the smaller parameter space are re-invested in longer T_{coh}. The dominant set-ups for G347.3 use shorter T_{coh} compared to the ones derived under the Vela Jr. CY prior. This is due to the fact that, with a smaller parameter space for Vela Jr., the most probability is harvested by exploiting it to the most, with long (expensive) T_{coh} and this is balanced by spending less on the other targets. Finally, because of the distance of Cas A is much larger than Vela Jr. and G347.3, the optimal way to distribute the computing budget is by searching Cas A with relatively cheap (less-sensitive) 10-day set-ups.

Since I do not know the age of Vela Jr., the set-up corresponding to which of the two priors should I pick? To answer this question, I investigate the consequences of having picked the prior that not corresponding to its true astrophysical value, namely the impact on the detection probability if I assume that Vela Jr. is 700 yrs old when Vela Jr. is 4300 yr old and if I assume that Vela Jr. is 4300 yrs old when Vela Jr. is 700 yr old. In the first case I search a broader spin-down range than I need to, in order to gather all the detection probability. To do this I use a less-sensitive set-up (shorter T_{coh}) for the most of the frequency band for Vela Jr. and, partly also for Cas A and G347.3 (see Figure 5.5(a), (c), (e)). The consequence of this is that I waste computing power in the high $\dot{f}$ region and lose detection probability due to the shorter T_{coh} set-ups used in the low $\dot{f}$ region. In the second case, I just search the low $\dot{f}$ region with longer Tcoh set-ups (see Figure 5.5(d)). I gain some detection probability due to adopting longer Tcoh set-ups in the low $\dot{f}$ of Vela Jr. and in parameter space of Cas A and G347.3. Meanwhile, I lose detection probability because I give up the whole high $\dot{f}$ range of Vela Jr..

Table 5.4: Effect of using the discrepant age prior for Vela Jr.

| | uniform distribution on f, $\dot{f}$ | | log-uniform distribution on f, $\dot{f}$ | | |
	C for Vela Jr.	F for Vela Jr.	C for Vela Jr.	F for Vela Jr.	$\langle loss \rangle$
$\mathcal{R}$ if Vela Jr. is 4300 yrs old but prior assumes 700 yrs of age	14.8%(16.1%): $loss =$**7.9%**	7.9%(8.6%): $loss =$**9.0%**	6.4%(11.4%): $loss =$**43.9%**	4.7%(4.9%): $loss =$**3.7%**	**16.1%**
$\mathcal{R}$ if Vela Jr. is 700 yrs old but prior assumes 4300 yrs of age	6.1%(18.7%): $loss =$**67.4%**	5.1%(11.4%): $loss =$**55.1%**	4.3%(9.2%): $loss =$**53.5%**	3.0%(4.5%): $loss =$**33.3%**	**52.3%**

Notes: The first number in each table cell is the $\mathcal{R}$ assuming a mismatch between the prior used in the optimization and the true age of the object. The number in parenthesis is the $\mathcal{R}$ if the prior is matched to the age of the object. The first number is always smaller than the $\mathcal{R}$ in parenthesis and the ratio in detection probability is in bold font.
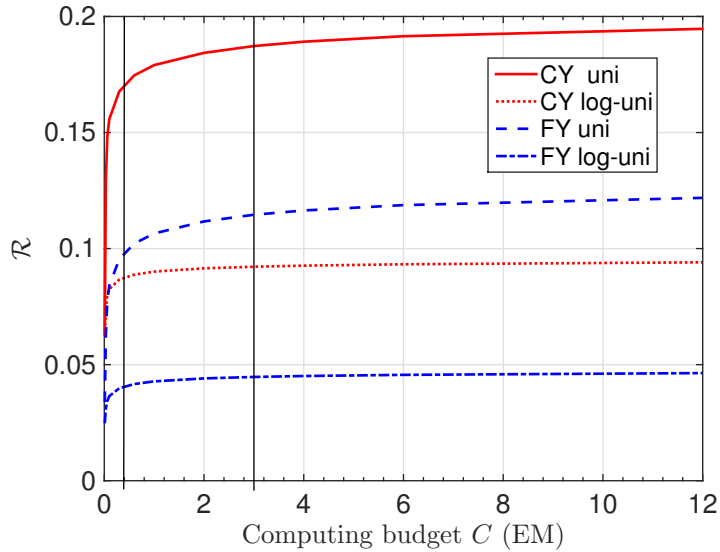
Figure 5.6: $\mathcal{R}$ versus computing budget C

The results are summarized in Table 5.4.

From these it is clear that using the youngest-age prior for Vela Jr. leads to the smallest loss in detection probability if this assumption is wrong, hence I use this prior in my optimizations.

5.3.3 The total computing budget

In the previous discussion I found that, if the likelihood of Vela Jr.'s frequency and spindown is uniform between 20 and 1500 Hz, and if Vela Jr. is 700 yrs old and at a distance of 200 pc, by optimally choosing set-ups and target parameter space to search with 3 EMs, the total detection probability $\mathcal{R}$ is 18.7%. It is then natural to ask whether by investing more computing resources I could achieve an even higher detection probability. Assuming a set of computing budgets from 0.1 EM to 12 EM, the optimization procedure yields the $\mathcal{R}$s shown in Figure 5.6 as a function of C. Although $\mathcal{R}$ always grows as C increases, the growth rate decreases as $\mathcal{R}$ increases. I identify three stages. In the first stage, when C is from 0.1 to 0.4 EM, $\mathcal{R}$ increases very fast. In the second stage when C is from 0.4 to

Table 5.5: Profile of the chosen set-ups

Targets	m_f	$m_{\dot{f}}$	$m_{\ddot{f}}$	$\gamma^{(1)}$	$\gamma^{(2)}$	T_{coh}	$\langle \mu \rangle$
Cas A	0.3	0.5	0.003	4	20	10D	41.2%
Vela Jr.	0.15	0.3	0.003	8	20	15D	15.8%
G347.3	0.15	0.2	0.003	8	10	20D	12.1%

$\sim$3 EM, $\mathcal{R}$ still increases but not as fast as before. In the last stage when C is larger than $\sim$3 EM, $\mathcal{R}$ increases even more slowly. In this regime a gain in the $\mathcal{R}$ due to 9 additional EMs, is less than 1%. Based on this I decide to invest around 3 EM in this search, covering the first two stages of $C(\mathcal{R})$.

5.3.4   Simplifications

As shown in the previous Sections, the optimal search set-up may well comprise different coherent time baselines T_{coh} in different $f - \dot{f}$ ranges for each target, and different grid spacings for the same T_{coh}. For instance, under the CY and uniform priors assumption for Vela Jr., the set-prescription comprises 2 different set-ups for $T_{\mathrm{coh}} = 10$ days, 7 set-ups for $T_{\mathrm{coh}} = 15$ days, and 5 set-ups for $T_{\mathrm{coh}} = 20$ days for Vela Jr.; 11 set-ups for $T_{\mathrm{coh}} = 10$ days for Cas A and 27 set-ups distributed over four different T_{coh} values (10, 15, 20, 30 days) for G347.3.

The analysis of the results from a search comprising this diversity in set-ups and coherent time baselines is quite daunting. So I examine the following question: how much detection probability would be lost if i) I considered only a single set-up per target ii) I extended the search frequency range for all targets to be fixed between 20-1500 Hz?

Limiting the set-up for each target to the 71 set-ups considered in Section 5.3.1 I have $71^3 = 357911$ combinations of setups. The computing costs of these ranges from a few 0.1EM to a few hundreds EM. I want a computing budget of a few EM. In Figure 5.7 I zoom in the cost range from 0 to 6EM and determine the total detection probability for all the set-up combinations.

I find that the loss due to having restricted the choice to a single set-up per target is smaller than $\sim$0.3% across all priors. Since this loss is much smaller than the total detection probability, I am persuaded to adopt this simplification and save ourselves a great deal of effort in the results post-processing phase.

I pick a computing budget just below 5 EM and hence the set-ups corresponding to the right-most golden star of Figure 5.7. Actually, all these golden stars correspond to the same set-ups independently of the priors for both the distance of Vela Jr. and f and $\dot{f}$. The details of the chosen set-up are listed in Table 5.5.

I use arrows to indicate the three chosen set-ups in Figure 5.5. Under the CY and uniform $f, \dot{f}$ assumption for Vela Jr., the chosen set-up for G347.3 is also the dominant one from the optimization scheme; the chosen set-up for Cas A is the second dominant one from the optimization scheme. Although the chosen set-up for Vela Jr. is the fourth dominant one from the optimization procedure (see Figure 5.5(c)) the chosen $T_{\mathrm{coh}} = 15$ days is the same that of the dominant set-up from the optimization scheme. These differences can be explained considering that I take different prior combinations
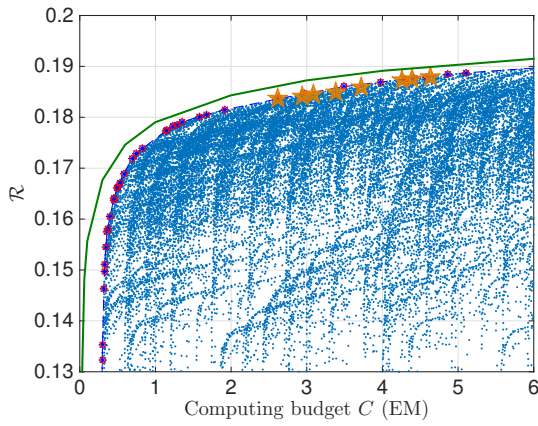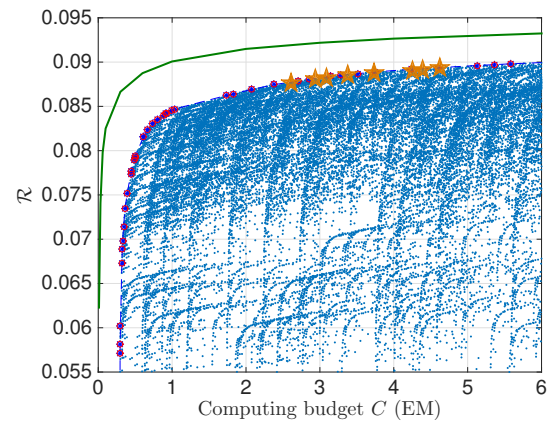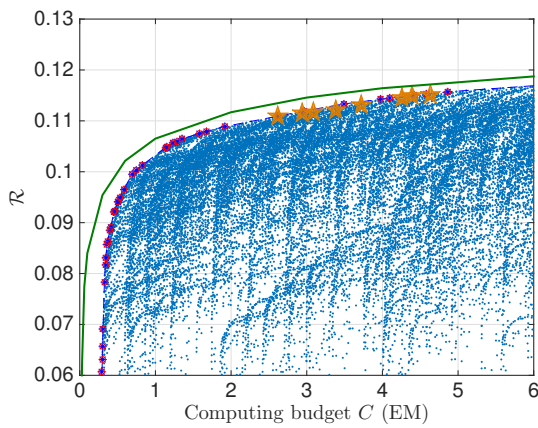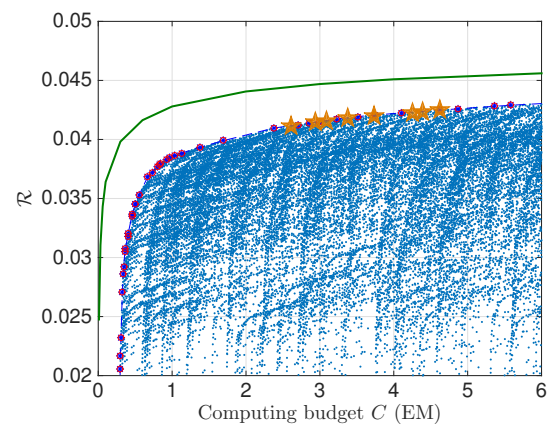
(a) Close and young, uniform distribution on f and $\dot{f}$

(b) Close and young, log-uniform distribution on f and $\dot{f}$

(c) Far and young, uniform distribution on f and $\dot{f}$

(d) Far and young, log-uniform distribution on f and $\dot{f}$

Figure 5.7: $\mathcal{R}$ versus computing budget C from 357911 combinations of setups with different priors. Each dot on this plot is a combination of setups, one per target. The green curve shows the optimal $\mathcal{R}$ as a function of C. The golden stars highlight the best setup combinations around 3 EM.

into account overall and the computing budget set for Figure 5.5 is 3 EM which is below the final-set budget 5 EM.

5.4 Conclusions

Following the search optimization procedure proposed in Chapter 4, I design a search using a few months of Einstein@Home optimized for a data set like the LIGO O1 data. I concentrate on 3 targets: Vela Jr., Cas A and G347.3. I extend the method proposed in Chapter 4 by adding more dimensions to the optimization : i.e. I consider different search set-ups for the same coherent time baseline T_{coh}, varying the template banks in frequency and spindown, and I fold-in the *measured* mismatch distributions from the different banks.

I also investigate how a mistake in choice of the astrophysical prior on the age of the target that contributes the most to the detection probability (Vela Jr.) would impact the detection probability, and then pick the prior that minimizes the loss.

I study the dependency of the attainable detection probability on the computing budget, and, within practical constraints from running the search, I make sure that I have nearly saturated the detection probability growth. I pick a computing budget of ~ 5 EM.

After having obtained the optimal combination of set-ups for the different targets in the different regions of parameter space, I significantly simplify it in order to make the post-processing of the results less cumbersome. Even limiting the search set-up to a single one per target, I am able to achieve this without significant degradation in the detection probability. One may wonder if this doesn't prove that the optimization scheme is actually not very important. In a sense it does, at least for this data set. However, without knowing what the optimal is, I would not have been able to judge the goodness of any empirically motivated set-up.

This is the final set-up chosen:

- For the youngest source Cas A, a set-up with 10 days coherent time baseline (12 segments) will be used. The computing cost employed on searching for a signal from Cas A is 1.7 EM. The detection probability is 1.2%, if I assume uniform priors in frequency and spin-down; the detection probability is 0.2%, if I assume log-uniform priors.

- For the closest source Vela Jr., a set-up with 15 days coherent time baseline (8 segments) will be used. The computing cost employed on searching for a signal from Vela Jr. is 2.2 EM. If I assume uniform priors in frequency and spin-down, a distance of 200 pc and an age of 700 yrs, the detection probability is 14.5%. The detection probability drops to 3.8% if I assume a distance of 750 pc and an age of 4300 yrs. If I assume log-uniform priors in frequency and spin-down, a distance of 200 pc and an age of 700 yrs, the detection probability is 7.4%. The detection probability drops to 3.0% if I assume a distance of 750 pc and an age of 4300 yrs.

- For the second closest source G347.3, a set-up with 20 days coherent time baseline (6 segments) will be used. The computing cost employed on searching for a signal from Vela Jr. is 0.7 EM. The detection probability is 3.1%, if I assume uniform priors in frequency and spin-down; the detection probability is 1.4%, if I assume log-uniform priors.
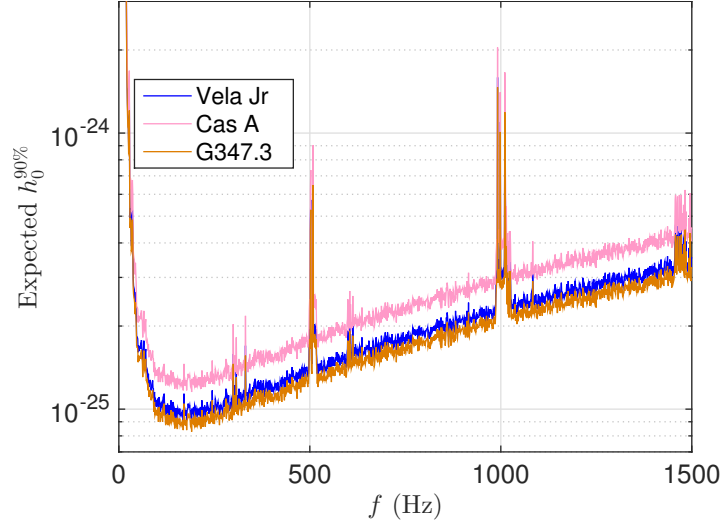
Figure 5.8: Expected 90% confidence upper limit on the GW amplitude $h_0^{90\%}$ from the directed searches proposed here.

The search that I propose here is a deep and broad frequency search for all the three targets Vela Jr., Cas A and G347.3. It was set-up and ran for a few months on the volunteer computing project Einstein@Home during the first half of 2017. The post-processing of the results will be reported in a separate paper. In case that no signal is detected the expected 90% confidence upper limit on the GW strain amplitude $h_0^{90\%}$ is shown in Figure 5.8. At the detector's most sensitive frequencies, ≈ 150 Hz, $h_0^{90\%}$ for Cas A is 1.4×10^{-25}, for Vela Jr. 1.0×10^{-25} and for G347.3 9×10^{-26}. I note that $h_0^{90\%} = 1.4 \times 10^{-25}$ for Cas A is 2 times smaller than the S6 upper limit [177] and deep searches on Vela Jr. and G347.3 have never been done yet. This can be quantified by using the notion of sensitivity depth defined in [78]. The sensitivity depth $\mathcal{D}^{90\%}$ of this search is 61.5 Hz$^{-1/2}$ for Cas A, 79.1 Hz$^{-1/2}$ for Vela Jr., and 85.8 Hz$^{-1/2}$ for G347.3.

Chapter 6

The Galactic Centre search

The Einstein@Home searches targeting Vela Jr, Cas A and G347.3 that I describe in Chapter 5 were completed by 8 April, 2017, roughly 40 days earlier than expected. This is not because of the timing model inaccuracy, but because the number of active hosts on Einstein@Home during the first 3 months was larger than expected[1].

As a consequence, we had about 5 months to complete another CW search before the new O2 data was ready to be analyzed. We decided to spend these 5 months on a search for CW emission from the Galactic Centre (GC). My third PhD project, which was unexpected, was to optimally set up this Galactic Centre search. Many details in setting up this search are similar to the details of the search described in Chapter 5, so in this chapter I will concentrate on the differences. At the time of writing this chapter (end of May, 2017), my search is deployed on Einstein@Home and tens of thousands of computers are calculating the numbers.

6.1   Motivation

As previously mentioned, many searches for CW signal have been carried out, but so far none of them has found CW signals yet. A possible explanation is that the ellipticity of spinning NSs might be much smaller than expected. Since the distribution of ellipticities is unknown, regions that contain many NSs are particularly interesting. The Galactic Centre (GC) is such a region.

The dynamical centre of our galaxy is a super massive black hole: Sgr A*. It has a mass of $4.3 \times 10^6 M_\odot$ and is 8 kpc far from the Earth [99]. The central cluster, which is nearby Sgr A* with a radius of 0.23 pc, is believed to have a very high stellar mass density [97]. It indicates that many NSs exist in the central cluster. Estimates suggest that there could be around 1000 radio pulsars within 0.02 pc of Sgr A* [145]. Generally, the entire GC area out to ~ 200 pc is thought to contain an overabundance of massive stars and NSs. About 10% of all the massive stars in the Galaxy are contained within this area [85]. Such a densely populated area is more likely to host a NS with a particularly high ellipticity.

---

[1]Perhaps, due to the an enthusiasm generated by the announcement by the first detection.

A GC search for CW emission was done using LIGO S5 data [36]. With O1 data, a factor of ~ 5 (at 150 Hz) more sensitive than the S5 data, I set out to design a new search, directed at the innermost 1 pc around Sgr A*.

6.2   The optimisation

The GC search is very similar to the search described in the previous chapter. In the GC search, the same data set and the same search method is used. Here, I won't repeat the description for them. However, there is a major difference that, the GC is not a point source like Vela Jr, Cas A or G347.3. The influence of template-signal mismatch in the sky needs to be taken into account. The main consequence of this is that the search now has two extra dimensions (the sky coordinates of the source) that need to be searched. Grids have to be set up in the sky and the contribution to the mismatch from these need to be folded-in the optimisation procedure. I recall the steps of such procedure below:

- As before, I separate the parameter space $(f, \dot{f})$ into many small enough and non-overlapping cells such that the detection probabilities and computing costs in cells vary smoothly from one cell to the next and the cost of searching any cell is much smaller that the total computing cost budget. The cell sizes are again $10\mathrm{Hz} \times 10^{-9}\mathrm{Hz/s}$.

- I compute the mismatch distributions from over 13000 different search set-ups. The number of search set-ups investigated here is about 5 times larger than the number in the multi-targets search because the mismatch in sky now needs to be considered. These are still produced from injection-and-recovery Monte Carlos.

- For each search set-up, I then calculate the detection probability and computing cost for each cell.

- I repeat the detection probability calculations for different astrophysical priors.

- Among all the set-ups with the same T_{coh} values, I select the ones that have the lowest computing cost at fixed mismatch. This results in 64 set-ups across all the different values of T_{coh}.

- Among all the cells, each with 64 set-ups, I select a set so that the sum of detection probabilities constrained by the available computing budget, is maximised. This is done through linear programming.

- Since optimal choice of cells spans a very broad frequency range, I determine the loss in detection probability caused by extending the search parameter space to include the broadest frequency band. I further evaluate the loss incurred compared to the optimal solution by utilising just two set-ups. Both these choices greatly simplify the post-processing of the Einstein@home results.

6.2.1 Astrophysical priors

The astrophysical priors need to be chosen before I compute the detection probability in each cell. In the multi-targets search, the ages of the source Cas A and G347.3 are known quite accurately, and the age of the source Vela Jr is known within a range. In the GC area, there could be over thousands of NSs with different ages. In order to include as many waveforms as possible, the age is set to be 300 years, so that the search ranges in $\dot{f}$ and $\ddot{f}$ are large enough. Since the GW emission frequencies are also unknown, I again include a large frequency range, from 20 to 1500 Hz. In contrast to the previous GC search [36], which only included the first order spin-down, the new GC search also includes the second order spin-down. For a given f, the $\dot{f}$ and $\ddot{f}$ ranges are determined by the fiducial age of the source $\tau = 300$ years:

$$\begin{cases} 20\,\text{Hz} \leq f \leq 1500\,\text{Hz} \\ -f/\tau \leq \dot{f} \leq 0\,\text{Hz/s} \\ 0\,\text{Hz/s}^2 \leq \ddot{f} \leq n\dot{f}^2/f. \end{cases} \tag{6.1}$$

The braking index is set to be $n = 5$ here so that the search encompasses all combinations of emission mechanisms. Both uniform and log-uniform priors on the search range of f and $\dot{f}$ are considered. However, the log-uniform priors are thought to be more realistic, so in the end the optimisation results based on the log-uniform priors mainly.

Similar to the multi-targets search, the prior $p(\varepsilon)$ is:

$$p(\varepsilon) = \begin{cases} \frac{1}{\varepsilon} \frac{1}{\log(\varepsilon^{\text{max}}/\varepsilon^{\text{min}})} & \varepsilon^{\text{min}} < \varepsilon < \varepsilon^{\text{max}} \\ 0 & \text{elsewhere}\,. \end{cases} \tag{6.2}$$

Where the $\varepsilon^{\text{min}} = 10^{-14}$ and $\varepsilon_i^{\text{max}} = \min(\varepsilon^{\text{sd}}, \varepsilon^{\text{age}}, 10^{-4})$. Note that, in the multi-targets search, the third limit on ε was set to be 10^{-6} because this is more realistic than 10^{-4}. However, there are a large number of NSs in the GC area and it is possible that some of them could have values of ε up to 10^{-4}. If we are able to detect any CW signals in the GC, they would be first from those NSs with larger ε. The other priors are exactly the same as the priors used for the multi-targets search described in the previous chapter (see Section 5.2)

6.2.2 Grid spacing and mismatch

In the GC search, the source encompasses an area of the sky rather than a single point. For each T_{coh}, a template bank is defined by the 7 spacings $\delta f, \delta \dot{f}_c, \delta \ddot{f}_c, \delta \dot{f}_f, \delta \ddot{f}_f, \delta\alpha, \delta\delta$, with $\delta\alpha$ and $\delta\delta$ including the spacings in right ascension and declination, respectively. In order to reduce the number of free parameters that define a template bank, I use $\delta\alpha$ and $\delta\delta$ such that the ratio $\frac{\delta\delta}{\delta\alpha} = \text{const}$. Both simulation results and considerations from the theoretical estimates [175] show a reasonable value for $\frac{\delta\delta}{\delta\alpha}$ is 9. Thus, for a given coherent duration T_{coh}, a template bank is defined by six parameters: the three nominal mismatch parameters $m_f, m_{\dot{f}}, m_{\ddot{f}}$, two refinement factors $\gamma^{(1)}$ and $\gamma^{(2)}$, and one sky grid spacing $\delta\alpha$.

The mismatch distribution of a template bank is then determined by injection-and-recovery Monte Carlos. More specifically, 500 artificial signals (including second-order spin-down) are created with

Table 6.1: Injection parameters used in mismatch investigation

Parameter	Range
Signal strength	$h_0^{\text{injected}} = 4$ (signal only)
Frequency [Hz]	$751\,\text{Hz} \leq f \leq 752\,\text{Hz}$
First spin-down [Hz/s]	$-10^{-7}\,\text{Hz/s} \leq \dot{f} \leq -10^{-12}\,\text{Hz/s}$
Second spin-down [Hz/s^2]	$10^{-22}\,\text{Hz/s}^2 \leq \ddot{f} \leq 5 \times 1500\,\text{Hz}/(300\,\text{yr})^2$
α [rad]	$4.649707 \leq \alpha \leq 4.649993$
δ [rad]	$-0.506405 \leq \alpha \leq -0.506155$

Notes: Parameters of the fake signals used to derive the mismatch distributions. f, α and δ are uniformly randomly distributed; $\dot{f}$ and $\ddot{f}$ are log-uniformly randomly distributed.

time stamps equal to the ones of the ER8+O1 LIGO data set[2]. These 500 artificial signals are randomly distributed in the 2×2 pc^2 square centred at Sgr A*. They are then searched with the given grid spacings and T_{coh}, and hence the measured detection statistic $\hat{\mathcal{F}}_{\text{meas}}$ is obtained. Then I repeat the search with a template that matches the signal parameters exactly and obtain the maximum detection statistic $\hat{\mathcal{F}}_{\text{max}}$. Repeating for 500 signals and following Equation (5.4), the mismatch distributions are obtained. Figures 6.1 and 6.2 show two examples of mismatch distribution from two grid spacings with $T_{\text{coh}} = 10$ days and 20 days, respectively. The parameters of the 500 artificial signals can be found in Table 6.1. Over 13 thousand different spacings are considered and the ranges for these spacings are listed in Table 6.2.

As shown in Table 6.1, all the injections are made between 751 and 752 Hz which is in the middle of the f range. After obtaining the mismatches from the signal recovery simulations at this frequency, I assume that the mismatch distributions at other frequencies are the same as long as the sky grid space at f is:

$$\delta\delta(f) = \delta\delta(751.5\,[\text{Hz}]) \times \frac{751.5\,[\text{Hz}]}{f} \,, \tag{6.3}$$

$$\delta\alpha(f) = \delta\alpha(751.5\,[\text{Hz}]) \times \frac{751.5\,[\text{Hz}]}{f} \,. \tag{6.4}$$

6.2.3   Set-ups: primary selection

As discussed in the last chapter, running the optimisation scheme on ~ 13 thousand set-ups is too computationally burdensome. I again down-select, among the ones with the same T_{coh}, those that yield the lowest average mismatch at fixed computing cost over the entire prior parameter range. Figure 6.3 shows that from 3375 set-ups (blue dots) with 10-day T_{coh}, 20 of them are selected as seeded set-ups (red circles). Considering different values for T_{coh}, I select 64 set-ups in total: 20 are from $T_{\text{coh}} = 10$ days, 18 from $T_{\text{coh}} = 15$ days, 12 from $T_{\text{coh}} = 20$ days, and 14 from $T_{\text{coh}} = 30$ days.

---

[2]ER8 is the the last engineering run before O1 and the data quality during ER8 is as good as O1 data.

Table 6.2: Parameters of candidate grid spaces

Parameter	Range
T_{coh} [Days]	10, 15, 20, 30 Days
m_f	$0.1 \le f \le 0.5$
$m_{\dot{f}}$	$0.1 \le m_{\dot{f}} \le 0.5$
$m_{\ddot{f}}$	$0.002 \le m_{\ddot{f}} \le 0.004$
$\gamma^{(1)}$	$5 \le \gamma^{(1)} \le 9$
$\gamma^{(2)}$	$11 \le \gamma^{(2)} \le 23$
$\delta\alpha$	$10^{-5} \le \delta\alpha \le 2.5 \times 10^{-4}$

Notes: due to the fixed relative sky spacing of $\frac{\delta\delta}{\delta\alpha} = 9$, the sky spacing $\delta\delta$ is not listed in this table.
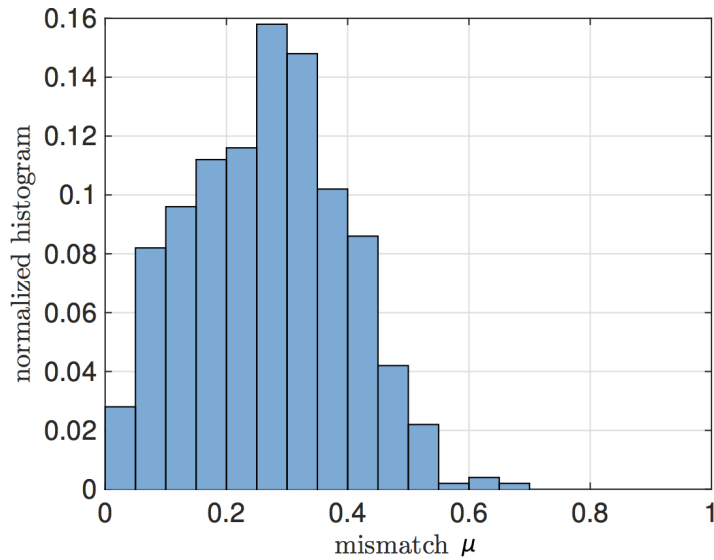

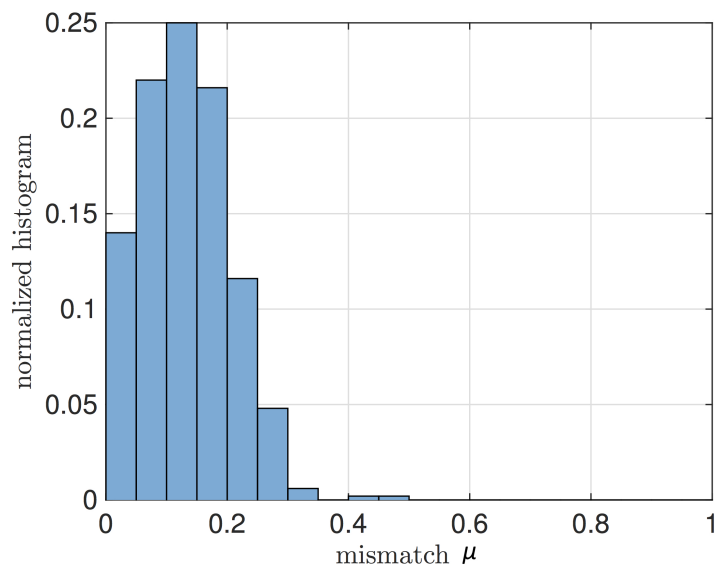
Figure 6.1: This histogram shows the mismatch distribution for the grid spacing: $m_f = 0.2$, $m_{\dot{f}} = 0.5$, $m_{\ddot{f}} = 0.004$, $\gamma^{(1)} = 9$, $\gamma^{(2)} = 23$, T_{coh}=10 days, and $\delta\alpha = 2 \times 10^{-4}$. The average measured mismatch is $\langle\mu\rangle = 26.8\%$.

Figure 6.2: This histogram shows the mismatch distribution for the grid spacing: $m_f = 0.15$, $m_{\dot{f}} = 0.5$, $m_{\ddot{f}} = 0.004$, $\gamma^{(1)} = 9$, $\gamma^{(2)} = 11$, T_{coh}=20 days, and $\delta\alpha = 1 \times 10^{-4}$. The average measured mismatch is $\langle\mu\rangle = 13.2\%$.

The measured average mismatch $\langle\mu\rangle$ of each of these distributions is used to reduce the expected SNR ρ^2 of a putative signal.

6.2.4   Computing budget

As mentioned in the beginning of this chapter, we had about 5 months to run a search on Einstein@Home. Based on the number of daily returned WUs from hosts in the multi-targets search, the estimation of the computing power of Einstein@Home is a factor of 1.8 larger than 5300 (A)-type cores. For the consistency of this thesis, in this chapter, 1 Einstein@Home month (EM) is still defined as 5300 (A)-type cores used continuously for 1 month. Therefore, the computing budget we have is 9 EM and this value is given to the LP optimisation procedure.

6.2.5   LP optimisation under different assumptions

I now use linear programming to determine the best search set-ups and the waveform parameter space to search. The 64 set-ups mentioned before are considered in this step.

Figure 6.4 shows the results of the optimisation given by LP assuming that the signals' frequency f and spindown $\dot{f}$ are (a) uniformly and (b) log-uniformly distributed within their ranges and with a 9 EM computing budget. The $\mathcal{R}$ is the sum of detection probabilities of the picked parameter space cells and C is the total computational cost. Both priors result in a value of a $\mathcal{R}$ around 0.36% which seems much smaller than the $\mathcal{R}$ (18.7%) in the multi-targets search. However, note that this detection
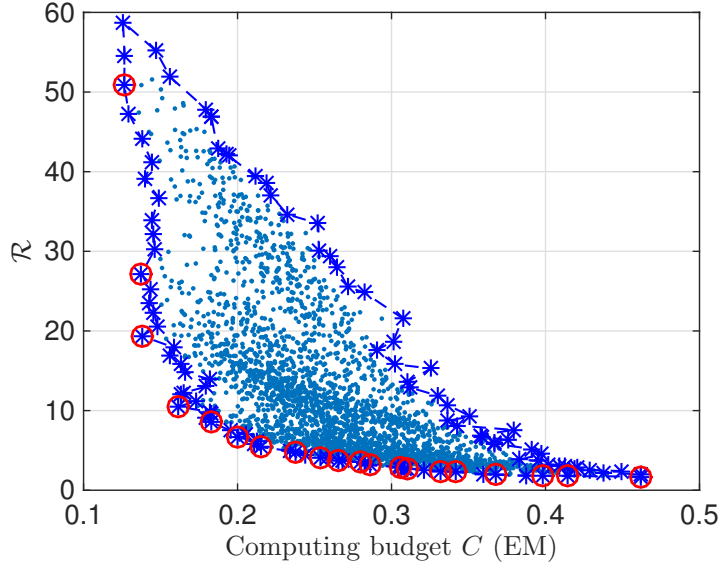
Figure 6.3: 3375 set-ups with $T_{\mathrm{coh}} = 10$ days. The 20 blue stars in red circle are selected for further consideration as explained in the text.

probability is obtained under the assumption that there is only one NS in the GC area. As discussed, the number of NS in the GC area could be more than 100. If I simply multiply this 0.36% by 100, I get a very promising detection probability 36%.

In Figure 6.4, different colours represent the set-ups with different T_{coh}. Cells in blue represent the 10-day T_{coh} seeded set-ups, magenta the 15-day T_{coh}, yellow the 20-day T_{coh}, and red the 30-day T_{coh}. In figure (a), the picked cell are using either 10, 15 or 20 days set-ups. At low f region, because the computing cost in each cell is relatively low, the 20-day set-ups are favored. As f increases, the computing cost of each cell increases rapidly and the shorter T_{coh} set-ups are used. In contrast, in figure (b), the cells in the low f region are favored because of the log prior. Therefore, for $f < 260$ Hz, the 30-day set-ups are mostly used. Similar to figure (a), as f goes up, the 20, 15 and 10 days set-ups are dominant in succession. This feature of the optimisation result indicates that it might be not a good idea to use just a single set-up in the whole parameter space in the next simplification step. Figure 6.5 further reveals details of the picked set-ups. It shows the number of cells searched by different set-ups assuming uniform priors (a) and log-uniform priors (b). For the uniform prior case, most of the selected set-ups have coherent lengths of less than 20 days. 28 of the original 64 set-ups are used for the uniform prior case (Figure 6.5 (a)): 8 from the 10-day sub set, 12 from the 15-day sub set, 6 from the 20-day sub set and 2 from the 30-day sub set (although both are used in a very small number of cells). In contrast, for the log-uniform prior case, many set-ups with 30 days T_{coh} were also chosen. 28 of the 64 set-ups were selected for the log-uniform prior (Figure 6.5 (b)): 11 from the 10-day sub set, 9 from the 15-day sub set, 6 from the 20-day sub set and 2 from the 30-day sub set.
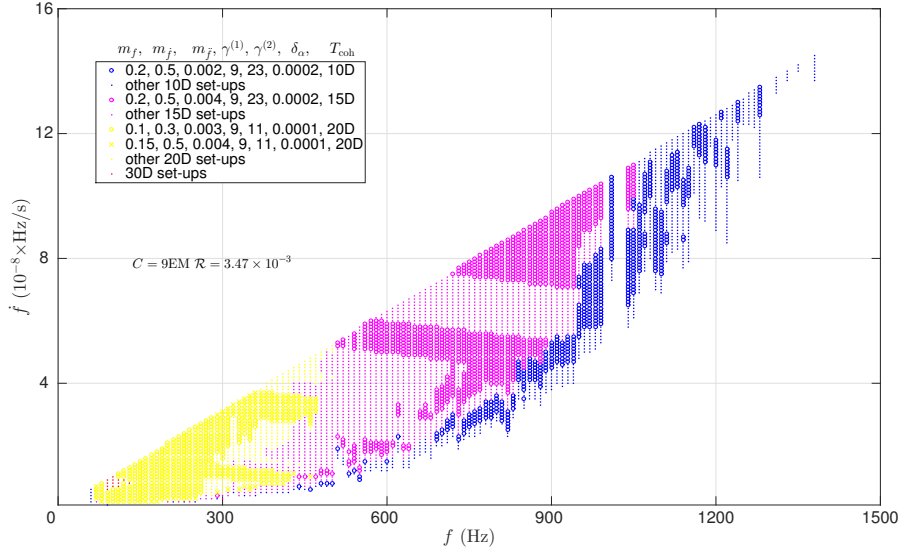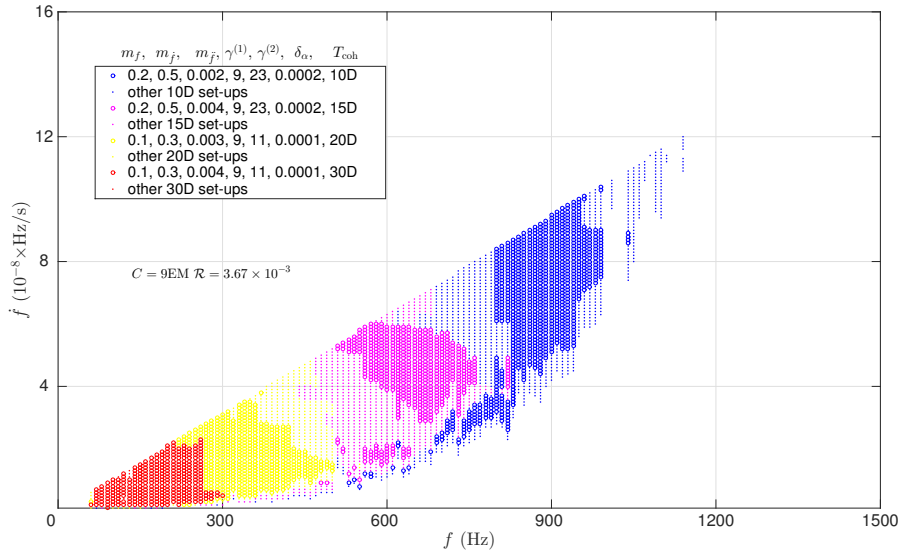
(a) Set-up details assuming uniform prior on f and $\dot{f}$

(b) Set-up details assuming log-uniform prior on f and $\dot{f}$

Figure 6.4: Optimization results given by LP. Parameter space coverage assuming uniform prior (A) and log-uniform prior (B), with 9 EM computing budget. Cells in blue represent these seeded set-ups of 10-day T_{coh} are used in that region of parameter space, magenta the 15-day T_{coh}, yellow the 20-day T_{coh},and red the 30-day T_{coh}. In figure (a), almost all the picked cell are using 10, 15 and 20 days set-ups. At low f region, because of the computing cost in each cell is relatively low, 20-day set-ups are used mostly. As f goes higher, the computing cost of each cells increases rapidly. Therefore the shorter T_{coh} set-ups are used. Whereas in figure (b), it favors the cells in low f region because of the log prior. Therefore, at region OF $f < 260$ Hz, the 30-day set-ups are used mostly. Similar to figure (a), as the f goes up, 20, 15 and 10-day set-ups are dominant in succession.

(a) Assuming uniform prior
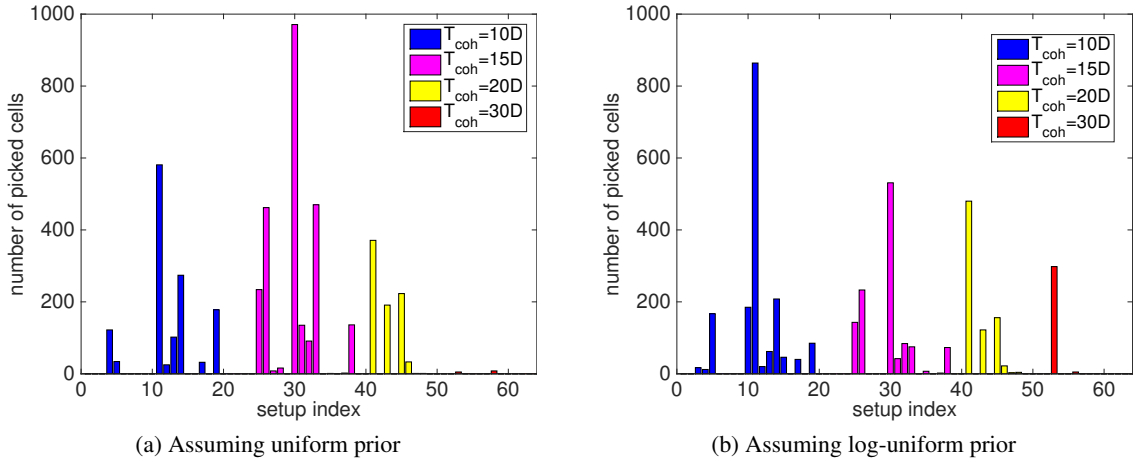
(b) Assuming log-uniform prior

Figure 6.5: Optimal set-up details. Figure (a) shows the set-ups assuming uniform prior and Figure (b) shows the set-ups assuming log-uniform prior.

6.2.6 Simplifications

As discussed in Section 5.3.4, I now try to reduce the number of set-ups for practical reasons. In the multi-targets search, I considered only a single set-up per target and I extended the search frequency range to be fixed between 20-1500 Hz. The relative loss in $\mathcal{R}$ from this simplification was less than 10%.

The cells in high f region require more computing resources. Larger values of f allow for larger values of $\dot{f}$, so the search range in $\ddot{f}$ is also larger (Equation (6.1)). In addition, the number of required sky grid points also increases with f (Equations (6.3) and (6.4)). After applying LP, I find that set-ups with longer coherent lengths are favored in low f regions while set-ups with shorter coherent lengths tend to be used in the high f regions (Figure 6.4). Therefore, the simplification for the GC search is inspired by this feature: fix the frequency range to 20-1500 Hz, and use two different set-ups. The whole parameter space is divided into two sub space: a low f region and a high f region, with a single set-up in each.

After this simplification, I have over 30000 combinations of setups. The computing costs range from 5 EM to a few hundred EM. I want a computing budget around 9 EM. In Figure 6.6 I zoom in the cost range from 0 to 30 EM and compare the actual (blue dots) and optimal $\mathcal{R}$ values from LP (green line) with different values of C. I find that the loss due to having restricted the choice to a single set-up per target is smaller than ~0.04% across all priors. Since this loss is only about 10% of the total detection probability, I adopt this simplification and save ourselves a great deal of effort in the post-processing. The best set-up combination is the one that has the smallest loss in $\mathcal{R}$ when considering both the uniform and log-uniform priors cases[3], near 10 EM (marked by the gold star in Figure 6.6).

---

[3]The golden star in log-uniform case is more close to the edge of blue dots region than the one in uniform case, because the log-uniform priors is favored
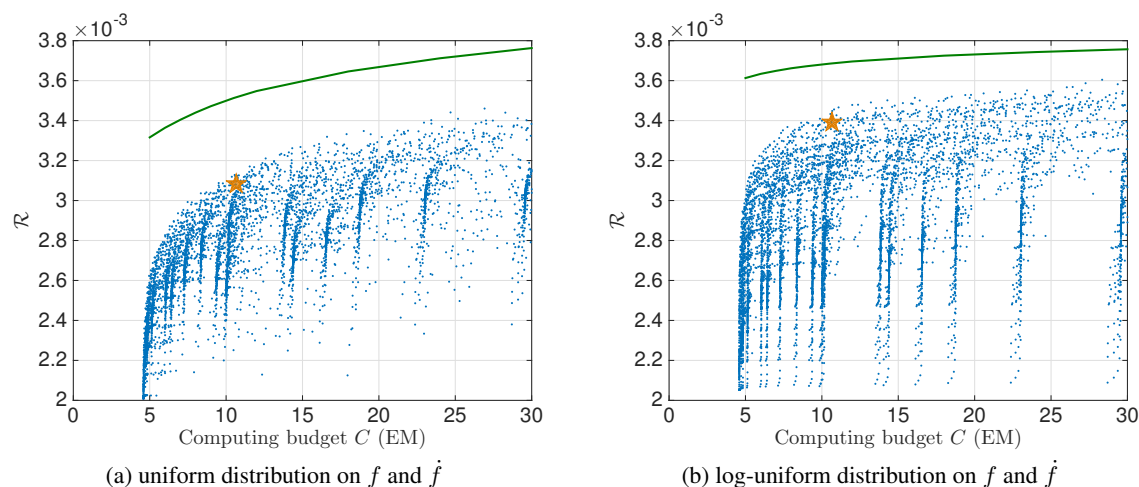
(a) uniform distribution on f and $\dot{f}$

(b) log-uniform distribution on f and $\dot{f}$

Figure 6.6: $\mathcal{R}$ versus computing budget C from combinations of set-ups with different priors. Each dot on this plot is a combination of setups. The green curve shows the optimal $\mathcal{R}$ as a function of C. The golden star highlight the best setup combinations around 10 EM.

Table 6.3: Profile of the chosen set-ups

f range	m_f	$m_{\dot{f}}$	$m_{\ddot{f}}$	$\gamma^{(1)}$	$\gamma^{(2)}$	$\delta\alpha$	T_{coh}	$\langle\mu\rangle$
20 to 500 Hz	0.15	0.5	0.004	9	11	0.0001	20D	13.2%
500 to 1500 Hz	0.2	0.5	0.004	9	23	0.0002	10D	26.8%

A 20-day set-up is used in the low f range from 20 to 500 Hz and a 10-day set-up is used in the high f range from 500 to 1500 Hz. 3.4 EM computing budget is required by the low f 20-day set-up and yields a detection probability of 0.19% in the uniform case or 0.32% in the log-uniform case; 7.2 EM computing budget is required by the high f 10-day set-up and yields a detection probability of 0.12% in the uniform case or 0.02% in the log-uniform case; The details of the chosen set-up are listed in Table 6.3. This 10.6 EM search is estimated to be finished in about 6 months.

6.3   Conclusions

Following the search optimisation procedure proposed in Chapter 4, I designed the second E@H directed search for CW signals using O1 LIGO data. This search targets a region that is most abundant in NSs ($2 \times 2 \, \mathrm{pc}^2$ around Sgr A*) and covers a broad frequency range from 20 to 1500 Hz. In contrast to the multi-targets search, the mismatch from sky grid is taken in to account for this search. Based on the optimisation results, I simplified the search set-ups in order to make the post-processing of the results less cumbersome. The final chosen set-up is:

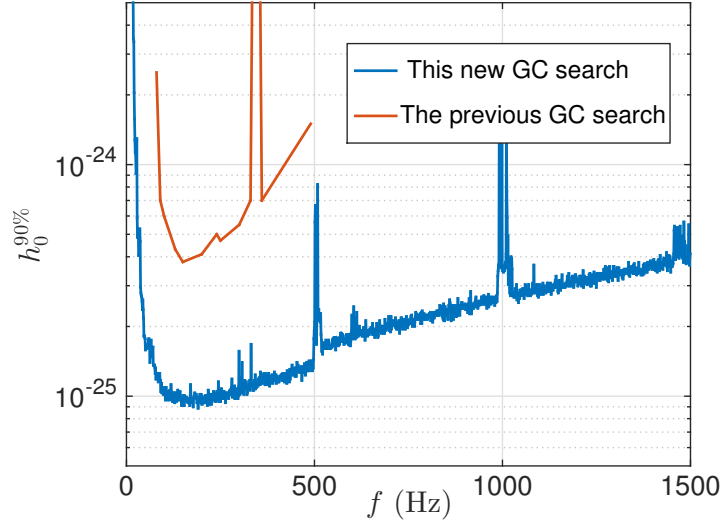- From 20 to 500 Hz, a set-up with 20 days coherent time baseline (12 segments) will be used. The

Figure 6.7: Expected 90% confidence upper limit on the GW amplitude $h_0^{90\%}$ from this GC search compared with the 90% upper limit of the previous GC search [36]. The search range in frequency of this new search is much broader than the range of the previous search and the expected $h_0^{90\%}$ of this new search is 4 to 10 times better than the $h_0^{90\%}$ of the previous search in the frequency range between 78 and 496 Hz.

computing cost employed on searching in this f range is 3.4 EM and the detection probability is 0.19% (uniform prior) and 0.32% (log-uniform prior).

- From 500 to 1500 Hz, a set-up with 10 days coherent time baseline (8 segments) will be used. The computing cost employed on searching in this high f range is 7.2 EM and the detection probability is 0.12% (uniform prior) and 0.02% (log-uniform prior).

- The above detection probabilities are obtained assuming one NS in the search area. However, there might be over 1000 NSs within the search area. Therefore, this GC search is very promising.

The search that I propose here is the first deep and broad f range search for the GC. In case that no signal is detected the expected 90% confidence upper limit of the GW strain amplitude $h_0^{90\%}$ is shown in Figure 6.7. These upper limits are good indicators of the sensitivity of the search. At the detector's most sensitive frequencies, $\approx$150 Hz, $h_0^{90\%}$ is 9×10^{-26}, a factor of 4 better than the previous GC search [36]. This new GC covers broader frequency range (20 to 1500 Hz) than the frequency range of previous GC search (78 to 496 Hz).

Chapter 7

Summary

It is computationally expensive to search for continuous gravitational waves even when we target small portions of the sky, for example supernova remnants or interesting regions like the Galactic Centre. Constrained by the available computing resources, decisions regarding the astrophysical target, the signal waveforms to search for, and search set-up, can make the difference between making a detection or not. Therefore, it is critically important to determine how intelligently to invest our computing resources. The first original part of this thesis is an optimisation method developed in order to solve this question.

The basic idea of this method is to divide the large parameter space of possible waveforms into many small cells. For many different search set-ups, the computing cost of each cell is estimated, and the detection probability of each cell is computed based on a set of reasonable astrophysical priors. The cells are ranked based on their computing cost and detection probability. By picking the cells from the ranked list until the computing budget is exhausted, the overall detection probability is maximized. I illustrate this method by using it to set up a directed search. The result indicates that Vela Jr is a more promising target than Cas A. It is interesting to note that, based on empirical considerations, up until now, far more compute cycles have been invested in searching for continuous gravitational waves from Cas A than from Vela Jr.

In the second original part of this thesis, I use the optimisation method to design an Einstein@Home search on O1 LIGO data. I expand and generalize the optimisation method, and allow for a few simplifications that considerably reduce the burden in the phase of processing of the search results: i) Instead of a single grid spacing combination, now many different combinations of grid spacings are considered for each coherent duration. ii) Instead of using analytical estimates which can have very large errors, the mismatch distributions measured from Monte Carto simulations are adopted. iii) The timing model to estimate the computing cost for each cell is revised. iv) The loss in detection probability due to a potential mistake in the choice of the object's age is evaluated. v) Simplifications with respect to the optimal solution are made and the impact on the detection probability is estimated.

In early December, 2016, my optimised search for continuous waves from Vela Jr, Cas A and G347.3 was launched. The detection probability is estimated to be $\sim 18\%$, with a GW strain amplitude sensitivity at 150 Hz of 1.0×10^{-25} for Vela Jr, 0.9×10^{-25} for G347.3 , and 1.4×10^{-25} for Cas A.

This search is the first deep and broad f range search for Cas A using the Advanced LIGO data and it is the first deep and broad f range search for Vela Jr and G347.3 ever performed. The sensitivity for Cas A is a factor of 2 better than previously obtained [177]. This search was finished on 8 April, 2017 and the analysis of the results is currently ongoing .

I also designed the set-up of a search for the continuous signals from isolated, unknown neutron stars at the Galactic Centre using O1 data. This is the third and last original part of my thesis. This search is currently being performed on Einstein@Home. In contrast to the point sources Vela Jr and Cas A of the multi-targets search, now I explore a $2 \times 2 \text{ pc}^2$ region centred around Sgr A* which adds two dimensions to the optimisation problem. With a computing budget of about 6 months on Einstein@Home, my optimisation scheme yields a detection probability of $\sim 30\%$ assuming at least 100 young neutron stars within the search region. At 150 Hz, I estimate the GW strain amplitude sensitivity to be about 9×10^{-26}, a factor of 4 better than the most constraining upper limits at the time of writing [36].

So far this proposed optimistion method has been used to set up two Einstein@Home searches. A huge amount of computing power to achieve a certain detection probability is saved because of this method. In the future, this method will be also used to set up blind searches, and hopefully will become a standard procedure for designing every CW search.

Appendix A

Main achievements and caveats of Chapter 4

In my first PhD project, as presented in Chapter 4, I develop a general framework to determine what waveforms to search for, what search set-up to use and what astrophysical targets to point to for a given computational budge and in such a way that the probability of making a detection is maximum. I carried out this research under the supervision of M. A. Papa and B. Krishnan. I developed all the software for the definition and characterization of the optimisation scheme.

I first realized that for the general case (Section 4.2.2) the efficiency ranking algorithm looks good, but mathematically, doesn't ensure the sum of detection probability is maximized. I illustrated it as the "CEO problem". Let's say you are the CEO of a multinational corporation. Recently there are positions available and the total monthly budget for these four positions is $10000. You receive a document from HR which shows that for each position there are two candidates each of them with their monthly wage demands (in red font) and work outputs (in blue font) (see Figure. A.1). The question for you as the CEO is that who will you hire so that the total work output is maximized constrained by the $10000 monthly budget (at most one person for each position). If we follow the efficiency ranking algorithm, the chosen persons would be A2+B1+C1+D2, which yields a total monthly work output $32 + 15 + 17 + 10 = 74$ and exhausts all $10000 of the budget. However, there is a better solution A1+B2+C2+D2 which yields a higher total monthly work output $50 + 9 + 8 + 10 = 77$ and spends just $9500 of the budget.

The CEO problem described above is the simplified case of the optimisation problem with more than one search set-ups. There are more than thousands of cells in parameter spaces, so the optimisation result can't be easily obtained manually. C. Aulbert, and H. Fehrmann pointed out that this problem might be solved by the method of linear programming (LP). My further investigation proved that the LP method is indeed an effective method to optimise the search set-up.

Position A		Position B		Position C		Position D	
A1:	$5000 50	**B1:**	$2500 15	**C1:**	$3000 17	**D1:**	$2000 10
A2:	$3000 32	**B2:**	$1500 9	**C2:**	$1500 8	**D2:**	$1500 10

Figure A.1: The CEO problem. The monthly wage demands (in red font) and work outputs (in blue font) of 8 candidates. A1, A2 are the candidates for position A; B1, B2 are the candidates for position B; C1, C2 are the candidates for position C; D1, D2 are the candidates for position D.

Appendix B

Main achievements and caveats of Chapter 5

Under the supervision of M. A. Papa and B. Krishnan, all of the works described in Chapter 5 was done by myself. It should be mentioned here the timing model described in Section 5.1.3 was mainly developed by R. Prix. C. Beer and I tested the timing model and contributed to the development of the model.

Appendix C

Acknowledgements

125

Appendix D

Curriculum Vitae

Personal information

Full name: Jing Ming

Date of birth: July 2rd, 1986

Place of birth: Zhejiang, China

Education

1993/09-1999/06   Jiefanglu primary school

1999/09-2002/06   Jiaxing NO.7 middle school

2002/09-2005/06   Jiaxing NO.1 high school

2005/09-2009/06   Bachelor of Civil Engineering, Shijiazhuang Railway Institute (SRI)

2010/09-2013/06   Master of Science in Astrophysics, Beijing Normal University (BNU)

Since   2013/09   PhD student of Albert-Einstein-Institut and Leibniz Universität Hannover (IMPRS stipend)

Since   2014/03   Member of the LIGO Scientific Collaboration

Appendix E

List of publications

K. Liao, Z. Li, J. Ming, and Z.-H. Zhu. 'Testing cosmic opacity from SNe Ia and Hubble parameter through three cosmological-model-independent methods'. *Physics Letters B*, 718:1166-1170, Jan. 2013.

J. Ming, B. Krishnan, M. A. Papa, C. Aulbert, and H. Fehrmann. 'Optimal directed searches for continuous gravitational waves'. *Physical Review D*, 93(6):064011, Mar. 2016.

J. Ming, M. A. Papa, B. Krishnan, R. Prix, C. Beer, S. J. Zhu, H.-B. Eggenstein, O. Bock, and B. Machenschalk. 'Optimally setting up directed searches for continuous gravitational waves in advanced ligo O1 data'. *Physical Review D*, submitted. `https://dcc.ligo.org/P1700166-x0`, 2017.

B. P. Abbott, et al. 'Observation of Gravitational Waves from a Binary Black Hole Merger'. *Physical Review Letters*, 116(6):061102, Feb. 2016.

The other publications authored as part of the LIGO scientific collaboration are not listed.

Bibliography

[1] https://en.wikipedia.org/wiki/User:Mysid.

[2] https://www.cfa.harvard.edu/CMB/bicep3/.

[3] http://igec.lnl.infn.it.

[4] https://en.wikipedia.org/wiki/Gravitational_wave.

[5] http://gwcenter.icrr.u-tokyo.ac.jp/en/researcher/parameter.

[6] http://gwpo.nao.ac.jp/en/.

[7] http://www.geo600.uni-hannover.de/.

[8] http://ligo.caltech.edu/.

[9] http://virgo4p.pg.infn.it/virgo/.

[10] http://www.gw-indigo.org/.

[11] https://dcc.ligo.org/LIGO-T0900288/public.

[12] https://intranet.aei.uni-hannover.de/geo600/
geohflogbook.nsf/f5b2cbf2a827c0198525624b00057d30/
4837a612ac990060c12575ce004e70fd.

[13] https://www.advancedligo.mit.edu/summary.html.

[14] https://www.advancedligo.mit.edu/aug_2016_news.html.

[15] The outreach article in Chinese for the first GW event. http://chuansong.me/n/
2342242.

[16] The LSC official Weibo. http://www.weibo.com/adligo.

[17] https://www.lisamission.org/proposal/LISA.pdf.

[18] `https://www.elisascience.org/articles/lisa-pathfinder/lpf-mission/lpf-mission-journal-approaching-launch`.

[19] `http://www.nature.com/news/daring-chinese-telescope-is-poised-to-transform-astr` `20681`.

[20] LAL/LALapps Software Suite.`http://www.lsc-group.phys.uwm.edu/daswg/projects/lalsuite.html`.

[21] `https://wiki.atlas.aei.uni-hannover.de/foswiki/bin/view/CW/WeaveOverview`.

[22] Details of Function linprog can be found at `http://de.mathworks.com/help/optim/ug/linprog.html`.

[23] Details of the Einstein@Home project can be found at `http://einstein.phys.uwm.edu`.

[24] Details of the BOINC project can be found at `http://boinc.berkeley.edu/`.

[25] The Einstein@Home Arecibo Radio Pulsar search.`https://einsteinathome.org/radiopulsar/html/`.

[26] Einstein@Home Gamma-ray Pulsar Discoveries in Fermi-LAT Data.`https://einsteinathome.org/gammaraypulsar/FGRP1_discoveries.html`.

[27] NOVEMBER 2016 TOP500.`https://www.top500.org/lists/2016/11/`.

[28] `http://monitor-server.atlas.aei.uni-hannover.de/ganglia/`.

[29] See Supplemental Material at [https://journals.aps.org/prd/supplemental/10.1103/PhysRevD.93.064011] for the complete set of illustrative-result figures of this paper.

[30] S6 Instrumental Lines of LIGO detectors `https://losc.ligo.org/s6speclines`.

[31] Details of resampling timing model can be found at `https://dcc.ligo.org/T1600531`.

[32] `http://www.aei.mpg.de/24838/02_Computing_and_ATLAS`.

[33] Science Gaia `http://www.esa.int/Our_Activities/Space_Science/Gaia`.

[34] J. Aasi, J. Abadie, B. P. Abbott, R. Abbott, T. Abbott, M. R. Abernathy, T. Accadia, F. Acernese, C. Adams, T. Adams, and et al. Constraints on Cosmic Strings from the LIGO-Virgo Gravitational-Wave Detectors. *Physical Review Letters*, 112(13):131101, Apr. 2014.

[35] J. Aasi, B. P. Abbott, R. Abbott, T. Abbott, M. R. Abernathy, F. Acernese, K. Ackley, C. Adams, T. Adams, T. Adams, and et al. Searches for continuous gravitational waves from nine young supernova remnants. *ArXiv e-prints*, Dec. 2014.

[36] J. Aasi et al. Directed search for continuous gravitational waves from the Galactic center. *Phys.Rev.*, D88(10):102002, 2013.

[37] J. Aasi et al. Einstein@Home all-sky search for periodic gravitational waves in LIGO S5 data. *Phys.Rev.*, D87(4):042001, 2013.

[38] J. Aasi et al. Gravitational waves from known pulsars: results from the initial detector era. *Astrophys. J.*, 785:119, 2014.

[39] J. Aasi et al. Narrow-band search of continuous gravitational-wave signals from Crab and Vela pulsars in Virgo VSR4 data. *Phys. Rev.*, D91(2):022004, 2015.

[40] J. Aasi et al. Searches for continuous gravitational waves from nine young supernova remnants. *Astrophys. J.*, 813(1):39, 2015.

[41] J. Abadie et al. First search for gravitational waves from the youngest known neutron star. *Astrophys.J.*, 722:1504–1513, 2010.

[42] J. Abadie et al. First search for gravitational waves from the youngest known neutron star. *Astrophys. J.*, 722:1504–1513, 2010.

[43] J. Abadie et al. Beating the spin-down limit on gravitational wave emission from the Vela pulsar. *Astrophys.J.*, 737:93, 2011.

[44] J. Abadie et al. All-sky Search for Periodic Gravitational Waves in the Full S5 LIGO Data. *Phys. Rev. D*, 85:022001, 2012.

[45] B. Abbott et al. First all-sky upper limits from LIGO on the strength of periodic gravitational waves using the Hough transform. *Phys. Rev. D*, 72:102004, 2005.

[46] B. Abbott et al. Coherent searches for periodic gravitational waves from unknown isolated sources and Scorpius X-1: Results from the second LIGO science run. *Phys. Rev. D*, 76:082001, 2007.

[47] B. Abbott et al. All-sky search for periodic gravitational waves in LIGO S4 data. *Phys. Rev. D*, 77:022001, 2008.

[48] B. Abbott et al. Beating the spin-down limit on gravitational wave emission from the Crab pulsar. *Astrophys.J.*, 683:L45–L50, 2008.

[49] B. Abbott et al. All-sky LIGO Search for Periodic Gravitational Waves in the Early S5 Data. *Phys. Rev. Lett.*, 102:111102, 2009.

[50] B. Abbott et al. Einstein@Home search for periodic gravitational waves in early S5 LIGO data. *Phys. Rev. D*, 80:042003, 2009.

[51] B. Abbott et al. The Einstein@Home search for periodic gravitational waves in LIGO S4 data. *Phys. Rev. D*, 79:022001, 2009.

[52] B. Abbott et al. The Einstein@Home search for periodic gravitational waves in LIGO S4 data. *Phys.Rev.*, D79:022001, 2009.

[53] B. P. Abbott, R. Abbott, T. D. Abbott, M. R. Abernathy, F. Acernese, K. Ackley, C. Adams, T. Adams, P. Addesso, R. X. Adhikari, and et al. Astrophysical Implications of the Binary Black-hole Merger GW150914. *The Astrophysical Journal, Letters*, 818:L22, Feb. 2016.

[54] B. P. Abbott, R. Abbott, T. D. Abbott, M. R. Abernathy, F. Acernese, K. Ackley, C. Adams, T. Adams, P. Addesso, R. X. Adhikari, and et al. Binary Black Hole Mergers in the First Advanced LIGO Observing Run. *Physical Review X*, 6(4):041015, Oct. 2016.

[55] B. P. Abbott, R. Abbott, T. D. Abbott, M. R. Abernathy, F. Acernese, K. Ackley, C. Adams, T. Adams, P. Addesso, R. X. Adhikari, and et al. Comprehensive all-sky search for periodic gravitational waves in the sixth science run LIGO data. *Physical Review D*, 94(4):042002, Aug. 2016.

[56] B. P. Abbott, R. Abbott, T. D. Abbott, M. R. Abernathy, F. Acernese, K. Ackley, C. Adams, T. Adams, P. Addesso, R. X. Adhikari, and et al. GW150914: The Advanced LIGO Detectors in the Era of First Discoveries. *Physical Review Letters*, 116(13):131103, Apr. 2016.

[57] B. P. Abbott, R. Abbott, T. D. Abbott, M. R. Abernathy, F. Acernese, K. Ackley, C. Adams, T. Adams, P. Addesso, R. X. Adhikari, and et al. GW151226: Observation of Gravitational Waves from a 22-Solar-Mass Binary Black Hole Coalescence. *Physical Review Letters*, 116(24):241103, June 2016.

[58] B. P. Abbott, R. Abbott, T. D. Abbott, M. R. Abernathy, F. Acernese, K. Ackley, C. Adams, T. Adams, P. Addesso, R. X. Adhikari, and et al. Observation of Gravitational Waves from a Binary Black Hole Merger. *Physical Review Letters*, 116(6):061102, Feb. 2016.

[59] B. P. Abbott, R. Abbott, T. D. Abbott, M. R. Abernathy, F. Acernese, K. Ackley, C. Adams, T. Adams, P. Addesso, R. X. Adhikari, and et al. Prospects for Observing and Localizing Gravitational-Wave Transients with Advanced LIGO and Advanced Virgo. *Living Reviews in Relativity*, 19:1, Dec. 2016.

[60] B. P. Abbott, R. Abbott, T. D. Abbott, M. R. Abernathy, F. Acernese, K. Ackley, C. Adams, T. Adams, P. Addesso, R. X. Adhikari, and et al. Tests of general relativity with gw150914. *Phys. Rev. Lett.*, 116:221101, May 2016.

[61] B. P. Abbott, R. Abbott, T. D. Abbott, M. R. Abernathy, F. Acernese, K. Ackley, C. Adams, T. Adams, P. Addesso, R. X. Adhikari, and et al. The Rate of Binary Black Hole Mergers Inferred from Advanced LIGO Observations Surrounding GW150914. *The Astrophysical Journal, Letters*, 833:L1, Dec. 2016.

[62] B. P. Abbott, R. Abbott, T. D. Abbott, M. R. Abernathy, F. Acernese, K. Ackley, C. Adams, T. Adams, P. Addesso, R. X. Adhikari, and et al. First Search for Gravitational Waves from Known Pulsars with Advanced LIGO. *The Astrophysical Journal*, 839:12, Apr. 2017.

[63] F. Acernese, M. Agathos, K. Agatsuma, D. Aisa, N. Allemandou, A. Allocca, J. Amarni, P. Astone, G. Balestri, G. Ballardin, and et al. Advanced Virgo: a second-generation interferometric gravitational wave detector. *Classical and Quantum Gravity*, 32(2):024001, Jan. 2015.

[64] O. D. Aguiar, L. A. Andrade, J. J. Barroso, F. Bortoli, L. A. Carneiro, P. J. Castro, C. A. Costa, K. M. F. Costa, J. C. N. de Araujo, A. U. de Lucena, W. de Paula, E. C. de Rey Neto, S. T. de Souza, A. C. Fauth, C. Frajuca, G. Frossati, S. R. Furtado, N. S. Magalhes, R. M. M. Jr, J. L. Melo, O. D. Miranda, N. F. O. Jr, K. L. Ribeiro, C. Stellati, W. F. V. Jr, and J. Weber. The brazilian gravitational wave detector mario schenberg: status report. *Classical and Quantum Gravity*, 23(8):S239, 2006.

[65] B. Allen and J. D. Romano. Detecting a stochastic background of gravitational radiation: Signal processing strategies and sensitivities. *Physical Review D*, 59(10):102001, May 1999.

[66] G. E. Allen, K. Chow, T. DeLaney, M. D. Filipovic, J. C. Houck, T. G. Pannuti, and M. D. Stage. On the Expansion Rate, Age, and Distance of the Supernova Remnant G266.2-1.2 (Vela Jr.). *Astrophys. J.*, 798(2):82, 2015.

[67] G. E. Allen, K. Chow, T. DeLaney, M. D. Filipovi, J. C. Houck, T. G. Pannuti, and M. D. Stage. On the expansion rate, age, and distance of the supernova remnant g266.21.2 (vela jr.). *The Astrophysical Journal*, 798(2):82, 2015.

[68] D. P. Anderson. BOINC: A System for Public-Resource Computing and Storage. In IEEE Computer Society, Washington, DC (USA), editor, *Proceedings of the Fifth IEEE/ACM International Workshop on Grid Computing (GRID04)*, pages 4–10, 2004.

[69] D. P. Anderson, C. Christensen, and B. Allen. Designing a Runtime System for Volunteer Computing. In IEEE Computer Society, Tampa, Florida (USA), editor, *Proceedings of the 2006 ACM/IEEE conference on Supercomputing*, pages 126–136, 2006.

[70] N. Andersson, V. Ferrari, D. Jones, K. Kokkotas, B. Krishnan, et al. Gravitational waves from neutron stars: Promises and challenges. *Gen.Rel.Grav.*, 43:409–436, 2011.

[71] M. Ando, S. Kawamura, N. Seto, S. Sato, T. Nakamura, K. Tsubono, T. Takashima, I. Funaki, K. Numata, N. Kanda, T. Tanaka, K. Ioka, K. Agatsuma, K. suke Aoyanagi, K. Arai,

A. Araya, H. Asada, Y. Aso, T. Chiba, T. Ebisuzaki, Y. Ejiri, M. Enoki, Y. Eriguchi, M.-K. Fu-jimoto, R. Fujita, M. Fukushima, T. Futamase, T. Harada, T. Hashimoto, K. Hayama, W. Hikida, Y. Himemoto, H. Hirabayashi, T. Hiramatsu, F.-L. Hong, H. Horisawa, M. Hosokawa, K. Ichiki, T. Ikegami, K. T. Inoue, K. Ishidoshiro, H. Ishihara, T. Ishikawa, H. Ishizaki, H. Ito, Y. Itoh, K. Izumi, I. Kawano, N. Kawashima, F. Kawazoe, N. Kishimoto, K. Kiuchi, S. Kobayashi, K. Kohri, H. Koizumi, Y. Kojima, K. Kokeyama, W. Kokuyama, K. Kotake, Y. Kozai, H. Ku-nimori, H. Kuninaka, K. Kuroda, K. ichi Maeda, H. Matsuhara, Y. Mino, O. Miyakawa, U. Miyamoto, S. Miyoki, M. Y. Morimoto, T. Morisawa, S. Moriwaki, S. Mukohyama, M. Musha, S. Nagano, I. Naito, K. Nakamura, M. Nakamura, H. Nakano, K. Nakao, S. Naka-suka, Y. Nakayama, K. Nakazawa, E. Nishida, K. Nishiyama, A. Nishizawa, Y. Niwa, T. Noumi, Y. Obuchi, M. Ohashi, N. Ohishi, M. Ohkawa, K. Okada, N. Okada, K. Oohara, N. Sago, M. Saijo, R. Saito, M. Sakagami, S. ichiro Sakai, S. Sakata, M. Sasaki, T. Sato, M. Shibata, H. Shinkai, K. Somiya, H. Sotani, N. Sugiyama, Y. Suwa, R. Suzuki, H. Tagoshi, F. Taka-hashi, K. Takahashi, K. Takahashi, R. Takahashi, R. Takahashi, T. Takahashi, H. Takahashi, T. Akiteru, T. Takano, K. Taniguchi, A. Taruya, H. Tashiro, Y. Torii, M. Toyoshima, S. Tsu-jikawa, Y. Tsunesada, A. Ueda, K. ichi Ueda, M. Utashima, Y. Wakabayashi, K. Yagi, H. Ya-makawa, K. Yamamoto, T. Yamazaki, J. Yokoyama, C.-M. Yoo, S. Yoshida, T. Yoshino, and K.-X. Sun. Decigo and decigo pathfinder. *Classical and Quantum Gravity*, 27(8):084010, 2010.

[72] M. Armano, H. Audley, G. Auger, J. T. Baird, M. Bassan, P. Binetruy, M. Born, D. Bor-toluzzi, N. Brandt, M. Caleno, L. Carbone, A. Cavalleri, A. Cesarini, G. Ciani, G. Congedo, A. M. Cruise, K. Danzmann, M. de Deus Silva, R. De Rosa, M. Diaz-Aguiló, L. Di Fiore, I. Diepholz, G. Dixon, R. Dolesi, N. Dunbar, L. Ferraioli, V. Ferroni, W. Fichter, E. D. Fitzsimons, R. Flatscher, M. Freschi, A. F. García Marín, C. García Marirrodriga, R. Gerndt, L. Gesa, F. Gibert, D. Giardini, R. Giusteri, F. Guzmán, A. Grado, C. Grimani, A. Grynagier, J. Grzymisch, I. Harrison, G. Heinzel, M. Hewitson, D. Hollington, D. Hoyland, M. Hueller, H. Inchauspé, O. Jennrich, P. Jetzer, U. Johann, B. Johlander, N. Karnesis, B. Kaune, N. Kor-sakova, C. J. Killow, J. A. Lobo, I. Lloro, L. Liu, J. P. López-Zaragoza, R. Maarschalkerweerd, D. Mance, V. Martín, L. Martin-Polo, J. Martino, F. Martin-Porqueras, S. Madden, I. Mateos, P. W. McNamara, J. Mendes, L. Mendes, A. Monsky, D. Nicolodi, M. Nofrarias, S. Paczkowski, M. Perreur-Lloyd, A. Petiteau, P. Pivato, E. Plagnol, P. Prat, U. Ragnit, B. Raïs, J. Ramos-Castro, J. Reiche, D. I. Robertson, H. Rozemeijer, F. Rivas, G. Russano, J. Sanjuán, P. Sarra, A. Schleicher, D. Shaul, J. Slutsky, C. F. Sopuerta, R. Stanga, F. Steier, T. Sumner, D. Texier, J. I. Thorpe, C. Trenkel, M. Tröbs, H. B. Tu, D. Vetrugno, S. Vitale, V. Wand, G. Wanner, H. Ward, C. Warren, P. J. Wass, D. Wealthy, W. J. Weber, L. Wissel, A. Wittchen, A. Zambotti, C. Zanoni, T. Ziegler, and P. Zweifel. Sub-femto-g free fall for space-based gravitational wave observatories: Lisa pathfinder results. *Phys. Rev. Lett.*, 116:231101, Jun 2016.

[73] P. Astone, D. Babusci, L. Baggio, M. Bassan, D. G. Blair, M. Bonaldi, P. Bonifazi, D. Busby, P. Carelli, M. Cerdonio, E. Coccia, L. Conti, C. Cosmelli, S. D'Antonio, V. Fafone, P. Falferi, P. Fortini, S. Frasca, G. Giordano, W. O. Hamilton, I. S. Heng, E. N. Ivanov, W. W. Johnson, A. Marini, E. Mauceli, M. P. McHugh, R. Mezzena, Y. Minenkov, I. Modena, G. Modestino,

A. Moleti, A. Ortolan, G. V. Pallottino, G. Pizzella, G. A. Prodi, L. Quintieri, A. Rocchi, E. Rocco, F. Ronga, F. Salemi, G. Santostasi, L. Taffarello, R. Terenzi, M. E. Tobar, G. Torrioli, G. Vedovato, A. Vinante, M. Visco, S. Vitale, and J. P. Zendri. Methods and results of the igec search for burst gravitational waves in the years 1997˘2000. *Phys. Rev. D*, 68:022001, Jul 2003.

[74] P. Astone, R. Ballantini, D. Babusci, M. Bassan, P. Bonifazi, G. Cavallari, A. Chincarini, E. Coccia, S. D'Antonio, M. D. P. Emilio, V. Fafone, S. Foffa, G. Gemme, G. Giordano, M. Maggiore, A. Marini, Y. Minenkov, I. Modena, G. Modestino, A. Moleti, G. V. Pallottino, R. Parodi, G. Pizzella, L. Quintieri, A. Rocchi, F. Ronga, R. Sturani, R. Terenzi, G. Torrioli, R. Vaccarone, G. Vandoni, and M. Visco. Explorer and nautilus gravitational wave detectors: a status report. *Classical and Quantum Gravity*, 25(11):114048, 2008.

[75] C. Aulbert and H. Fehrmann. Technical report, 2008. `http://www.mpg.de/308429/forschungsSchwerpunkt`.

[76] R. Balasubramanian, B. S. Sathyaprakash, and S. V. Dhurandhar. Gravitational waves from coalescing binaries: Detection strategies and Monte Carlo estimation of parameters. *Physical Review D*, 53:3033–3055, Mar. 1996.

[77] W. Becker. *Neutron stars and pulsars*. Springer, Berlin, 2009.

[78] B. Behnke, M. A. Papa, and R. Prix. Postprocessing methods used in the search for continuous gravitational-wave signals from the Galactic Center. *Phys. Rev.*, D91(6):064007, 2015.

[79] L. Bildsten. Gravitational Radiation and Rotation of Accreting Neutron Stars. *The Astrophysical Journal, Letters*, 501:L89–L93, July 1998.

[80] D. Blair. *Advanced gravitational wave detectors*. Cambridge University Press, Cambridge, UK New York, 2012.

[81] D. G. Blair, E. N. Ivanov, M. E. Tobar, P. J. Turner, F. van Kann, and I. S. Heng. High sensitivity gravitational wave antenna with parametric transducer readout. *Phys. Rev. Lett.*, 74:1908–1911, Mar 1995.

[82] M. Bonaldi, M. Cerdonio, L. Conti, M. Pinard, G. A. Prodi, L. Taffarello, and J. P. Zendri. Selective readout and back-action reduction for wideband acoustic gravitational wave detectors. *Phys. Rev. D*, 68:102004, Nov 2003.

[83] P. R. Brady and T. Creighton. Searching for periodic sources with LIGO. 2. Hierarchical searches. *Phys. Rev. D*, 61:082001, 2000.

[84] P. R. Brady, T. Creighton, C. Cutler, and B. F. Schutz. Searching for periodic sources with LIGO. *Phys. Rev. D*, 57:2101–2116, 1998.

[85] B. C. Bromley, S. J. Kenyon, M. J. Geller, and W. R. Brown. Binary disruption by massive black holes: Hypervelocity stars, s stars, and tidal disruption events. *The Astrophysical Journal Letters*, 749(2):L42, 2012.

[86] A. Buonanno and Y. Chen. Signal recycled laser-interferometer gravitational-wave detectors as optical springs. *Phys. Rev. D*, 65:042001, Jan 2002.

[87] Y.-F. Cai and X. Zhang. Probing the origin of our universe through primordial gravitational waves by Ali CMB project. *Science China Physics, Mechanics, and Astronomy*, 59(7):178, July 2016.

[88] M. Cerdonio, M. Bonaldi, D. Carlesso, E. Cavallini, S. Caruso, A. Colombo, P. Falferi, G. Fontana, P. L. Fortini, R. Mezzena, A. Ortolan, G. A. Prodi, L. Taffarello, G. Vedovato, S. Vitale, and J. P. Zendri. The ultracryogenic gravitational-wave detector auriga. *Classical and Quantum Gravity*, 14(6):1491, 1997.

[89] C. Cutler, I. Gholami, and B. Krishnan. Improved stack-slide searches for gravitational-wave pulsars. *Phys. Rev. D*, 72:042004, 2005.

[90] C. Cutler and B. F. Schutz. The Generalized F-statistic: Multiple detectors and multiple GW pulsars. *Phys. Rev. D*, 72:063006, 2005.

[91] T. Damour. Introductory Lectures on the Effective One Body Formalism. *International Journal of Modern Physics A*, 23:1130–1148, 2008.

[92] G. Dantzig. *Linear programming and extensions*. Rand Corporation Research Study. Princeton Univ. Press, Princeton, NJ, 1963.

[93] K. Danzmann. {LISA} an {ESA} cornerstone mission for the detection and observation of gravitational waves. *Advances in Space Research*, 32(7):1233 – 1242, 2003. Fundamental Physics in Space.

[94] K. L. Dooley, T. Akutsu, S. Dwyer, and P. Puppo. Status of advanced ground-based laser inter-ferometers for gravitational-wave detection. In *Journal of Physics Conference Series*, volume 610 of *Journal of Physics Conference Series*, page 012012, May 2015.

[95] R. D. Ferdman, R. van Haasteren, C. G. Bassa, M. Burgay, I. Cognard, A. Corongiu, N. D'Amico, G. Desvignes, J. W. T. Hessels, G. H. Janssen, A. Jessner, C. Jordan, R. Karup-pusamy, E. F. Keane, M. Kramer, K. Lazaridis, Y. Levin, A. G. Lyne, M. Pilia, A. Possenti, M. Purver, B. Stappers, S. Sanidas, R. Smits, and G. Theureau. The european pulsar timing ar-ray: current efforts and a leap toward the future. *Classical and Quantum Gravity*, 27(8):084014, 2010.

[96] J. E. Field. The mechanical and strength properties of diamond. *Reports on Progress in Physics*, 75(12):126505, 2012.

[97] D. F. Figer. *Massive-star formation in the Galactic center:*, pages 40–59. 2009.

[98] L. S. Finn and D. F. Chernoff. Observing binary inspiral in gravitational radiation: One inter-ferometer. *Phys. Rev. D*, 47:2198–2219, Mar 1993.

[99] S. Gillessen, F. Eisenhauer, S. Trippe, T. Alexander, R. Genzel, F. Martins, and T. Ott. Monitoring Stellar Orbits Around the Massive Black Hole in the Galactic Center. *The Astrophysical Journal*, 692:1075–1109, Feb. 2009.

[100] X. Gong, Y.-K. Lau, S. Xu, P. Amaro-Seoane, S. Bai, X. Bian, Z. Cao, G. Chen, X. Chen, Y. Ding, P. Dong, W. Gao, G. Heinzel, M. Li, S. Li, F. Liu, Z. Luo, M. Shao, R. Spurzem, B. Sun, W. Tang, Y. Wang, P. Xu, P. Yu, Y. Yuan, X. Zhang, and Z. Zhou. Descope of the ALIA mission. In *Journal of Physics Conference Series*, volume 610 of *Journal of Physics Conference Series*, page 012011, May 2015.

[101] L. Gottardi, A. de Waard, O. Usenko, G. Frossati, M. Podt, J. Flokstra, M. Bassan, V. Fafone, Y. Minenkov, and A. Rocchi. Sensitivity of the spherical gravitational wave detector minigrail operating at 5 k. *Phys. Rev. D*, 76:102005, Nov 2007.

[102] L. P. Grishchuk and M. Solokhin. Spectra of relic gravitons and the early history of the hubble parameter. *Physical Review D*, 43:2566–2571, Apr 1991.

[103] G. M. Harry, P. Fritschel, D. A. Shaddock, W. Folkner, and E. S. Phinney. Laser interferometry for the big bang observer. *Classical and Quantum Gravity*, 23(15):4887, 2006.

[104] G. M. Harry and LIGO Scientific Collaboration. Advanced LIGO: the next generation of gravitational wave detectors. *Classical and Quantum Gravity*, 27(8):084006, Apr. 2010.

[105] G. Hobbs, A. Archibald, Z. Arzoumanian, D. Backer, M. Bailes, N. D. R. Bhat, M. Burgay, S. Burke-Spolaor, D. Champion, I. Cognard, W. Coles, J. Cordes, P. Demorest, G. Desvignes, R. D. Ferdman, L. Finn, P. Freire, M. Gonzalez, J. Hessels, A. Hotan, G. Janssen, F. Jenet, A. Jessner, C. Jordan, V. Kaspi, M. Kramer, V. Kondratiev, J. Lazio, K. Lazaridis, K. J. Lee, Y. Levin, A. Lommen, D. Lorimer, R. Lynch, A. Lyne, R. Manchester, M. McLaughlin, D. Nice, S. Oslowski, M. Pilia, A. Possenti, M. Purver, S. Ransom, J. Reynolds, S. Sanidas, J. Sarkissian, A. Sesana, R. Shannon, X. Siemens, I. Stairs, B. Stappers, D. Stinebring, G. Theureau, R. van Haasteren, W. van Straten, J. P. W. Verbiest, D. R. B. Yardley, and X. P. You. The international pulsar timing array project: using pulsars as a gravitational wave detector. *Classical and Quantum Gravity*, 27(8):084013, 2010.

[106] G. Hobbs, R. Hollow, D. Champion, J. Khoo, D. Yardley, M. Carr, M. Keith, F. Jenet, S. Amy, M. Burgay, S. Burke-Spolaor, J. Chapman, L. Danaia, B. Homewood, A. Kovacevic, M. Mao, D. McKinnon, M. Mulcahy, S. Oslowski, and W. van Straten. The pulse@parkes project: a new observing technique for long-term pulsar monitoring. *Publications of the Astronomical Society of Australia*, 26(4):468–475, 001 2009.

[107] C. Horowitz and K. Kadau. The Breaking Strain of Neutron Star Crust and Gravitational Waves. *Phys. Rev. Lett.*, 102:191102, 2009.

[108] B. Iyer, T. Souradeep, C. Unnikrishnan, S. Dhurandhar, S. Raja, and A. Sengupta. Ligo-india, proposal of the consortium for indian initiative in gravitational-wave observations (indigo). `https://dcc.ligo.org/cgi-bin/DocDB/ShowDocument?docid=75988`, 2011.

[109] H.-T. Janka, K. Langanke, A. Marek, G. Martínez-Pinedo, and B. Müller. Theory of core-collapse supernovae. *Physics Reports*, 442:38–74, Apr. 2007.

[110] P. Jaranowski. *Analysis of gravitational-wave data*. Cambridge University Press, Cambridge New York, 2009.

[111] P. Jaranowski, A. Królak, and B. F. Schutz. Data analysis of gravitational - wave signals from spinning neutron stars. 1. The Signal and its detection. *Phys. Rev. D*, 58:063001, 1998.

[112] F. Jenet, L. S. Finn, J. Lazio, A. Lommen, M. McLaughlin, I. Stairs, D. Stinebring, J. Verbiest, A. Archibald, Z. Arzoumanian, D. Backer, J. Cordes, P. Demorest, R. Ferdman, P. Freire, M. Gonzalez, V. Kaspi, V. Kondratiev, D. Lorimer, R. Lynch, D. Nice, S. Ransom, R. Shannon, and X. Siemens. The North American Nanohertz Observatory for Gravitational Waves. *ArXiv e-prints*, Sept. 2009.

[113] L. JIANG, C.-M. ZHANG, A. TANNI, and H.-H. ZHAO. Characteristic age and true age of pulsars. *International Journal of Modern Physics: Conference Series*, 23:95–98, 2013.

[114] N. K. Johnson-McDaniel and B. J. Owen. Maximum elastic deformations of relativistic stars. *Phys. Rev.*, D88:044004, 2013.

[115] V. Kalogera and D. Psaltis. Bounds on neutron-star moments of inertia and the evidence for general relativistic frame dragging. *Physical Review D*, 61(2):024009, Jan. 2000.

[116] S. Kawamura, T. Nakamura, M. Ando, N. Seto, K. Tsubono, K. Numata, R. Takahashi, S. Nagano, T. Ishikawa, M. Musha, K. ichi Ueda, T. Sato, M. Hosokawa, K. Agatsuma, T. Akutsu, K. suke Aoyanagi, K. Arai, A. Araya, H. Asada, Y. Aso, T. Chiba, T. Ebisuzaki, Y. Eriguchi, M.-K. Fujimoto, M. Fukushima, T. Futamase, K. Ganzu, T. Harada, T. Hashimoto, K. Hayama, W. Hikida, Y. Himemoto, H. Hirabayashi, T. Hiramatsu, K. Ichiki, T. Ikegami, K. T. Inoue, K. Ioka, K. Ishidoshiro, Y. Itoh, S. Kamagasako, N. Kanda, N. Kawashima, H. Kirihara, K. Kiuchi, S. Kobayashi, K. Kohri, Y. Kojima, K. Kokeyama, Y. Kozai, H. Kudoh, H. Kunimori, K. Kuroda, K. ichi Maeda, H. Matsuhara, Y. Mino, O. Miyakawa, S. Miyoki, H. Mizusawa, T. Morisawa, S. Mukohyama, I. Naito, N. Nakagawa, K. Nakamura, H. Nakano, K. Nakao, A. Nishizawa, Y. Niwa, C. Nozawa, M. Ohashi, N. Ohishi, M. Ohkawa, A. Okutomi, K. Oohara, N. Sago, M. Saijo, M. Sakagami, S. Sakata, M. Sasaki, S. Sato, M. Shibata, H. Shinkai, K. Somiya, H. Sotani, N. Sugiyama, H. Tagoshi, T. Takahashi, H. Takahashi, R. Takahashi, T. Takano, T. Tanaka, K. Taniguchi, A. Taruya, H. Tashiro, M. Tokunari, S. Tsujikawa, Y. Tsunesada, K. Yamamoto, T. Yamazaki, J. Yokoyama, C.-M. Yoo, S. Yoshida, and T. Yoshino. The japanese space gravitational wave antennadecigo. *Classical and Quantum Gravity*, 23(8):S125, 2006.

[117] D. Keitel. Robust semicoherent searches for continuous gravitational waves with noise and signal models including hours to days long transients. *Physical Review D*, 93(8):084024, Apr. 2016.

[118] D. Keitel and R. Prix. Line-robust statistics for continuous gravitational waves: safety in the case of unequal detector sensitivities. *Classical and Quantum Gravity*, 32(3):035004, Feb. 2015.

[119] D. Keitel, R. Prix, M. A. Papa, P. Leaci, and M. Siddiqi. Search for continuous gravitational waves: Improving robustness versus instrumental artifacts. *Phys. Rev. D*, 89(6):064023, Mar. 2014.

[120] H. J. Kimble, Y. Levin, A. B. Matsko, K. S. Thorne, and S. P. Vyatchanin. Conversion of conventional gravitational-wave interferometers into quantum nondemolition interferometers by modifying their input and/or output optics. *Phys. Rev. D*, 65:022002, Dec 2001.

[121] B. Knispel and B. Allen. Blandford's Argument: The Strongest Continuous Gravitational Wave Signal. *Phys.Rev.*, D78:044031, 2008.

[122] M. Kramer, D. Backer, J. Cordes, T. Lazio, B. Stappers, and S. Johnston. Strong-field tests of gravity using pulsars and black holes. *New Astronomy Reviews*, 48(1112):993 – 1002, 2004. Science with the Square Kilometre ArrayScience with the Square Kilometre Array.

[123] B. Krishnan. Wide parameter search for isolated pulsars using the Hough transform. *Class. Quant. Grav.*, 22:S1265–S1276, 2005.

[124] B. Krishnan, A. M. Sintes, M. A. Papa, B. F. Schutz, S. Frasca, et al. The Hough transform search for continuous gravitational waves. *Phys. Rev. D*, 70:082001, 2004.

[125] LIGO Scientific Collaboration, J. Aasi, B. P. Abbott, R. Abbott, T. Abbott, M. R. Abernathy, K. Ackley, C. Adams, T. Adams, P. Addesso, and et al. Advanced LIGO. *Classical and Quantum Gravity*, 32(7):074001, Apr. 2015.

[126] LIGO Scientific Collaboration and Virgo Collaboration. First low-frequency all-sky search for continuous gravitational waves in advanced LIGO data. *https://dcc.ligo.org/P1700127*, 2017.

[127] J. Luo, L.-S. Chen, H.-Z. Duan, Y.-G. Gong, S. Hu, J. Ji, Q. Liu, J. Mei, V. Milyukov, M. Sazhin, C.-G. Shao, V. T. Toth, H.-B. Tu, Y. Wang, Y. Wang, H.-C. Yeh, M.-S. Zhan, Y. Zhang, V. Zharov, and Z.-B. Zhou. TianQin: a space-borne gravitational wave detector. *Classical and Quantum Gravity*, 33(3):035010, Feb. 2016.

[128] H. Lck, C. Affeldt, J. Degallaix, A. Freise, H. Grote, M. Hewitson, S. Hild, J. Leong, M. Prijatelj, K. A. Strain, B. Willke, H. Wittel, and K. Danzmann. The upgrade of geo 600. *Journal of Physics: Conference Series*, 228(1):012012, 2010.

[129] I. Mandel, D. A. Brown, J. R. Gair, and M. C. Miller. Rates and Characteristics of Intermediate Mass Ratio Inspirals Detectable by Advanced LIGO. *The Astrophysical Journal*, 681:1431–1447, July 2008.

[130] E. Mauceli, Z. K. Geng, W. O. Hamilton, W. W. Johnson, S. Merkowitz, A. Morse, B. Price, and N. Solomonson. The Allegro gravitational wave detector: Data acquisition and analysis. *Physical Review D*, 54:1264–1275, July 1996.

[131] K. McKenzie, N. Grosse, W. P. Bowen, S. E. Whitcomb, M. B. Gray, D. E. McClelland, and P. K. Lam. Squeezing in the audio gravitational-wave detection band. *Phys. Rev. Lett.*, 93:161105, Oct 2004.

[132] C. Messenger, R. Prix, and M. A. Papa. Random template banks and relaxed lattice coverings. *Physical Review D*, 79(10):104017, May 2009.

[133] J. Ming, B. Krishnan, M. A. Papa, C. Aulbert, and H. Fehrmann. Optimal directed searches for continuous gravitational waves. *Physical Review D*, 93(6):064011, Mar. 2016.

[134] J. Ming, M. A. Papa, B. Krishnan, R. Prix, C. Beer, S. J. Zhu, H.-B. Eggenstein, O. Bock, and B. Machenschalk. Optimally setting up directed searches for continuous gravitational waves in advanced ligo o1 data. https://arxiv.org/abs/1708.02173, 2017.

[135] S. Mirshekari. *Gravitational waves and inspiraling compact binaries in alternative theories of gravity*. PhD thesis, Washington University in St. Louis, 2013.

[136] R.-D. Nan, Q.-M. Wang, L.-C. Zhu, W.-B. Zhu, C.-J. Jin, and H.-Q. Gan. Pulsar observations with radio telescope fast. *Chinese Journal of Astronomy and Astrophysics*, 6(S2):304, 2006.

[137] J. Neyman and E. S. Pearson. On the problem of the most efficient tests of statistical hypotheses. *Philosophical Transactions of the Royal Society of London. Series A, Containing Papers of a Mathematical or Physical Character*, 231:289–337, 1933.

[138] B. J. Owen. Search templates for gravitational waves from inspiraling binaries: Choice of template spacing. *Physical Review D*, 53:6749–6761, June 1996.

[139] B. J. Owen. How photon astronomy affects searches for continuous gravitational waves. *Class.Quant.Grav.*, 26:204014, 2009.

[140] P. Brady *et al.* . *Phys. Rev. D*, 61:082001, 2000.

[141] C. Palomba. Simulation of a population of gravitational wave-driven neutron stars. *Class.Quant.Grav.*, 22:S1027–S1039, 2005.

[142] M. A. Papa et al. Hierarchical follow-up of sub-threshold candidates of an all-sky Einstein@Home search for continuous gravitational waves on LIGO sixth science run data. *Phys. Rev.*, D94(12):122006, 2016.

[143] M. A. Papa, B. F. Schutz, and A. M. Sintes. Searching for continuous gravitational wave signals: The hierarchical Hough transform algorithm. In *Gravitational waves: A challenge to theoretical astrophysics. Proceedings, Trieste, Italy, June 6-9, 2000*, pages 431–442, 2000.

[144] P. Patel, X. Siemens, R. Dupuis, and J. Betzwieser. Implementation of barycentric resampling for continuous wave searches in gravitational wave data. *Phys. Rev. D*, 81(8):084032, Apr. 2010.

[145] E. Pfahl and A. Loeb. Probing the Spacetime around Sagittarius A* with Radio Pulsars. *The Astrophysical Journal*, 615:253–258, Nov. 2004.

[146] A. Pisarski and P. Jaranowski. Banks of templates for all-sky narrow-band searches of gravitational waves from spinning neutron stars. *Classical and Quantum Gravity*, 32(14):145014, July 2015.

[147] M. Pitkin, S. Reid, S. Rowan, and J. Hough. Gravitational Wave Detection by Interferometry (Ground and Space). *Living Reviews in Relativity*, 14:5, Dec. 2011.

[148] H. J. Pletsch. Parameter-space correlations of the optimal statistic for continuous gravitational-wave detection. *Phys. Rev. D*, 78:102005, 2008.

[149] H. J. Pletsch. Parameter-space metric of semicoherent searches for continuous gravitational waves. *Phys. Rev. D*, 82:042002, 2010.

[150] H. J. Pletsch and B. Allen. Exploiting global correlations to detect continuous gravitational waves. *Phys. Rev. Lett.*, 103:181102, 2009.

[151] R. Prix. Search for continuous gravitational waves: Metric of the multi-detector F-statistic. *Phys. Rev. D*, 75:023004, 2007.

[152] R. Prix and M. Shaltev. Search for Continuous Gravitational Waves: Optimal StackSlide method at fixed computing cost. *Phys.Rev.*, D85:084010, 2012.

[153] M. Punturo, M. Abernathy, F. Acernese, B. Allen, N. Andersson, K. Arun, F. Barone, B. Barr, M. Barsuglia, M. Beker, N. Beveridge, S. Birindelli, S. Bose, L. Bosi, S. Braccini, C. Bradaschia, T. Bulik, E. Calloni, G. Cella, E. C. Mottin, S. Chelkowski, A. Chincarini, J. Clark, E. Coccia, C. Colacino, J. Colas, A. Cumming, L. Cunningham, E. Cuoco, S. Danilishin, K. Danzmann, G. D. Luca, R. D. Salvo, T. Dent, R. Derosa, L. D. Fiore, A. D. Virgilio, M. Doets, V. Fafone, P. Falferi, R. Flaminio, J. Franc, F. Frasconi, A. Freise, P. Fulda, J. Gair, G. Gemme, A. Gennai, A. Giazotto, K. Glampedakis, M. Granata, H. Grote, G. Guidi, G. Hammond, M. Hannam, J. Harms, D. Heinert, M. Hendry, I. Heng, E. Hennes, S. Hild, J. Hough, S. Husa, S. Huttner, G. Jones, F. Khalili, K. Kokeyama, K. Kokkotas, B. Krishnan, M. Lorenzini, H. Lck, E. Majorana, I. Mandel, V. Mandic, I. Martin, C. Michel, Y. Minenkov, N. Morgado, S. Mosca, B. Mours, H. Mller-Ebhardt, P. Murray, R. Nawrodt, J. Nelson, R. Oshaughnessy, C. D. Ott, C. Palomba, A. Paoli, G. Parguez, A. Pasqualetti, R. Passaquieti,

D. Passuello, L. Pinard, R. Poggiani, P. Popolizio, M. Prato, P. Puppo, D. Rabeling, P. Rapagnani, J. Read, T. Regimbau, H. Rehbein, S. Reid, L. Rezzolla, F. Ricci, F. Richard, A. Rocchi, S. Rowan, A. Rdiger, B. Sassolas, B. Sathyaprakash, R. Schnabel, C. Schwarz, P. Seidel, A. Sintes, K. Somiya, F. Speirits, K. Strain, S. Strigin, P. Sutton, S. Tarabrin, J. van den Brand, C. van Leewen, M. van Veggel, C. van den Broeck, A. Vecchio, J. Veitch, F. Vetrano, A. Vicere, S. Vyatchanin, B. Willke, G. Woan, P. Wolfango, and K. Yamamoto. The third generation of gravitational wave observatories and their science reach. *Classical and Quantum Gravity*, 27(8):084007, 2010.

[154] M. Punturo, M. Abernathy, F. Acernese, B. Allen, N. Andersson, K. Arun, F. Barone, B. Barr, M. Barsuglia, M. Beker, N. Beveridge, S. Birindelli, S. Bose, L. Bosi, S. Braccini, C. Bradaschia, T. Bulik, E. Calloni, G. Cella, E. C. Mottin, S. Chelkowski, A. Chincarini, J. Clark, E. Coccia, C. Colacino, J. Colas, A. Cumming, L. Cunningham, E. Cuoco, S. Danilishin, K. Danzmann, G. D. Luca, R. D. Salvo, T. Dent, R. D. Rosa, L. D. Fiore, A. D. Virgilio, M. Doets, V. Fafone, P. Falferi, R. Flaminio, J. Franc, F. Frasconi, A. Freise, P. Fulda, J. Gair, G. Gemme, A. Gennai, A. Giazotto, K. Glampedakis, M. Granata, H. Grote, G. Guidi, G. Hammond, M. Hannam, J. Harms, D. Heinert, M. Hendry, I. Heng, E. Hennes, S. Hild, J. Hough, S. Husa, S. Huttner, G. Jones, F. Khalili, K. Kokeyama, K. Kokkotas, B. Krishnan, M. Lorenzini, H. Lck, E. Majorana, I. Mandel, V. Mandic, I. Martin, C. Michel, Y. Minenkov, N. Morgado, S. Mosca, B. Mours, H. MllerEbhardt, P. Murray, R. Nawrodt, J. Nelson, R. Oshaughnessy, C. D. Ott, C. Palomba, A. Paoli, G. Parguez, A. Pasqualetti, R. Passaquieti, D. Passuello, L. Pinard, R. Poggiani, P. Popolizio, M. Prato, P. Puppo, D. Rabeling, P. Rapagnani, J. Read, T. Regimbau, H. Rehbein, S. Reid, L. Rezzolla, F. Ricci, F. Richard, A. Rocchi, S. Rowan, A. Rdiger, B. Sassolas, B. Sathyaprakash, R. Schnabel, C. Schwarz, P. Seidel, A. Sintes, K. Somiya, F. Speirits, K. Strain, S. Strigin, P. Sutton, S. Tarabrin, A. Thring, J. van den Brand, C. van Leewen, M. van Veggel, C. van den Broeck, A. Vecchio, J. Veitch, F. Vetrano, A. Vicere, S. Vyatchanin, B. Willke, G. Woan, P. Wolfango, and K. Yamamoto. The einstein telescope: a third-generation gravitational wave observatory. *Classical and Quantum Gravity*, 27(19):194002, 2010.

[155] M. Punturo and H. Lück. Toward a third generation of gravitational wave observatories. *General Relativity and Gravitation*, 43(2):363–385, 2011.

[156] M. Punturo, H. Lück, and M. Beker. *A Third Generation Gravitational Wave Observatory: The Einstein Telescope*, pages 333–362. Springer International Publishing, Cham, 2014.

[157] P. Purdue. Analysis of a quantum nondemolition speed-meter interferometer. *Phys. Rev. D*, 66:022001, Jun 2002.

[158] P. Purdue and Y. Chen. Practical speed meter designs for quantum nondemolition gravitational-wave interferometers. *Phys. Rev. D*, 66:122004, Dec 2002.

[159] B. S. Sathyaprakash and B. F. Schutz. Physics, Astrophysics and Cosmology with Gravitational Waves. *Living Reviews in Relativity*, 12:2, Dec. 2009.

[160] B. Schutz. *A first course in general relativity*. Cambridge University Press, Cambridge New York, 2009.

[161] B. F. Schutz and M. A. Papa. End-to-end algorithm for hierarchical area searches for long duration GW sources for GEO-600. In *34th Rencontres de Moriond: Gravitational Waves and Experimental Gravity Les Arcs, France, January 23-30, 1999*, 1999.

[162] B. F. Schutz and F. Ricci. Gravitational Waves, Sources, and Detectors. *ArXiv e-prints*, May 2010.

[163] M. Shaltev, P. Leaci, M. A. Papa, and R. Prix. Fully coherent follow-up of continuous gravitational-wave candidates: an application to Einstein@Home results. *Phys. Rev.*, D89(12):124030, 2014.

[164] S. Shapiro and S. Teukolsky. *Black holes, white dwarfs, and neutron stars*. Wiley-VCH Verlag GmbH & Co. KgaA, Weinheim, 2004.

[165] K. Somiya. Detector configuration of KAGRA-the Japanese cryogenic gravitational-wave detector. *Classical and Quantum Gravity*, 29(12):124007, June 2012.

[166] S. R. Taylor, M. Vallisneri, J. A. Ellis, C. M. F. Mingarelli, T. J. W. Lazio, and R. van Haasteren. Are We There Yet? Time to Detection of Nanohertz Gravitational Waves Based on Pulsar-timing Array Limits. *The Astrophysical Journal, Letters*, 819:L6, Mar. 2016.

[167] The LIGO Scientific Collaboration and The Virgo Collaboration. Results of the deepest all-sky survey for continuous gravitational waves on LIGO S6 data running on the Einstein@Home volunteer distributed computing project. *ArXiv e-prints*, June 2016.

[168] G. Ushomirsky, C. Cutler, and L. Bildsten. Deformations of accreting neutron star crusts and gravitational wave emission. *Mon. Not. Roy. Astron. Soc.*, 319:902, 2000.

[169] M. Volonteri, F. Haardt, and P. Madau. The Assembly and Merging History of Supermassive Black Holes in Hierarchical Models of Galaxy Formation. *The Astrophysical Journal*, 582:559–573, Jan. 2003.

[170] L. Wade, X. Siemens, D. L. Kaplan, B. Knispel, and B. Allen. Continuous Gravitational Waves from Isolated Galactic Neutron Stars in the Advanced Detector Era. *Phys.Rev.*, D86:124011, 2012.

[171] J. Weber. Gravitational radiation. *Phys. Rev. Lett.*, 18:498–501, Mar 1967.

[172] J. M. Weisberg and J. H. Taylor. The Relativistic Binary Pulsar B1913+16: Thirty Years of Observations and Analysis. In F. A. Rasio and I. H. Stairs, editors, *Binary Radio Pulsars*, volume 328 of *Astronomical Society of the Pacific Conference Series*, page 25, July 2005.

[173] K. Wette. Lattice template placement for coherent all-sky searches for gravitational-wave pulsars. *Physical Review D*, 90(12):122010, Dec. 2014.

[174] K. Wette. Parameter-space metric for all-sky semicoherent searches for gravitational-wave pulsars. *Physical Review D*, 92(8):082003, Oct. 2015.

[175] K. Wette and R. Prix. Flat parameter-space metric for all-sky searches for gravitational-wave pulsars. *Physical Review D*, 88(12):123005, Dec. 2013.

[176] C. M. Will. The Confrontation between General Relativity and Experiment. *Living Reviews in Relativity*, 17:4, Dec. 2014.

[177] S. J. Zhu, M. Alessandra Papa, H.-B. Eggenstein, R. Prix, K. Wette, B. Allen, O. Bock, D. Keitel, B. Krishnan, B. Machenschalk, M. Shaltev, and X. Siemens. An Einstein@home search for continuous gravitational waves from Cassiopeia A. *ArXiv e-prints*, Aug. 2016.

[178] M. Zimmermann and E. Szedenits. Gravitational waves from rotating and precessing rigid bodies: Simple models and applications to pulsars. *Phys. Rev. D*, 20:351–355, Jul 1979.